THE EVALUATION OF TURBULENCE MODELS USING TENSOR VISUALIZATION TECHNIQUES

by

Scott A. Schorn

Thesis submitted to the Faculty of the

Virginia Polytechnic Institute and State University

in partial fulfillment of the requirements

for the degree of

MASTER OF SCIENCE

in Mechanical Engineering

APPROVED:

J. Moore, Chairman

C.L. Dancey

F.J. Pierce

June, 1995

Blacksburg, VA

c.2

THE EVALUATION OF TURBULENCE MODELS USING TENSOR VISUALIZATION TECHNIQUES

by

Scott A. Schorn

Committee Chairman: Prof. J. Moore

Mechanical Engineering Department

(ABSTRACT)

A new method of representing a second order tensor, the tensor glyph, is used to present the Reynolds stresses found in turbulent flow. Various glyph types discussed in the literature are analyzed, and a glyph suitable for the Reynolds stress tensor is developed. This glyph is constructed so that the degree of anisotropy and the orientation of the principal directions are clearly presented. Using the glyph, the effectiveness of two turbulence model formulations of the Reynolds stress tensor, the Boussinesq approximation and the Algebraic Reynolds Stress Model (ARSM), are studied. Glyphs based upon these two formulations and experimentally measured Reynolds stresses are compared in two flow geometries: fully developed pipe flow and a tip leakage turbine cascade. The glyph representations are compared with traditional presentations of the Reynolds stress tensor to ascertain the strengths and weaknesses of both.

ACKNOWLEDGMENTS

This project would not have been possible without the help and support of several people and organizations. I am greatly indebted to Dr. John and Joan Moore, whose counsel and guidance were of great value throughout the course of this work. Together, they provided a work environment which was challenging as well as enjoyable. I would also like to thank my parents, whose love and support throughout my life and in this work have been invaluable. In addition, I would like to thank Rolls Royce and the Mechanical Engineering Department of Virginia Polytechnic Institute and State University for their financial support of this project. Lastly, I would like to thank Ron Kriz, whose work with tensor visualization techniques provided the inspiration for this project.

TABLE OF CONTENTS

TABLE OF CONTENTS (continued)

TABLE OF CONTENTS (continued)

TABLE OF CONTENTS (continued)

LIST OF FIGURES

LIST OF FIGURES (continued)

LIST OF FIGURES (continued)

LIST OF FIGURES (continued)

NOMENCLATURE

a	Pipe radius
a_{ij}	Coordinate transformation matrix
c	Turbine blade axial chord
C_d	Turbulence dissipation model constant
C_s	Reynolds stress transport equation model constant
C_{z1}	Two equation turbulence model constant
C_{z2}	Two equation turbulence model constant
C_μ	Turbulence dissipation - eddy viscosity model constant
C_μ'	Kolmogorov - Prandtl eddy viscosity model constant
C_1	Reynolds stress transport equation model constant
d_i	direction unit vector components
D_{ij}	Diffusion of Reynolds stress components
D_k	Diffusion of turbulence kinetic energy
k	Turbulence kinetic energy
L	Turbulence length scale
l_m	Mixing length
n_i	normal unit vector components
P	Turbulence kinetic energy production
P	Mean Pressure

NOMENCLATURE (continued)

p	Instantaneous pressure fluctuation
$\underline{P}_i$	Principal direction vectors
P_{ij}	Reynolds stress component production
P_{MAX}, P_{MIN}	Major, minor principal stress values
r'	a - r
R	Radius
Re	Reynolds number
S	Source term
$\underline{S}_i$	Maximum shearing stress vectors
t	time
T	Integral time scale
Tu	Turbulence intensity
u_i, u,v,w	Instantaneous velocity components
U_i, U,V,W	Mean Velocity Components
U_o	Freestream/Centerline velocity
U_τ	Friction velocity
x_i, y_i, x,y,z	Cartesian coordinate components
x_i, x,r,ϕ	Cylindrical coordinate components
X_R	Eigenvalue Matrix

NOMENCLATURE (continued)

Greek Symbols

δ_{ij}	Kronecker delta
ΔF_i	Total force vector components
ΔS	Planar surface area
$\Delta y'$	y component of the turbine blade to blade width
Δz	turbine blade span
ε	Rate of turbulence dissipation
ϕ_{ij}	Turbulence pressure-strain component
μ	Laminar viscosity
μ_t	Turbulence viscosity
ν	Laminar kinematic viscosity
ν_t	Turbulence kinematic viscosity
ρ	Density
σ	Normal stress magnitude
σ_i	Stress vector components
σ_{ij}	Stress tensor components
σ_k	One equation turbulence model constant
σ_{MAJ}, σ_{MID}, σ_{MIN}	Major, middle, and minor principal stresses
σ_P	Principal stress value

NOMENCLATURE (continued)

σ_z	Two Equation turbulence model constant
θ	Coordinate system rotation angle
θ_P	Rotation angle to principal directions
overbar	Time Averaged Quantities

1.0 Introduction

Since the time Osborne Reynolds first derived the Reynolds stress tensor and, in this way, effectively formulated the influence of turbulence on the motion of a fluid, the development of an accurate model to fully predict the Reynolds stress tensor has been a primary goal of fluid dynamicists. In the past three decades, the modern computer has stimulated efforts to this cause, and the number of turbulence models has grown significantly as a result. Because of the complexity of the Reynolds stress tensor, however, its presentation throughout a considered flowfield has traditionally had no simple form. This makes comparisons between measured Reynolds stress tensors and the variety of tensors predicted by turbulence models a difficult, time-consuming, endeavor.

The increased imaging capabilities of the computer, however, can now be used to help alleviate difficulties in comparing measured and modeled Reynolds stress tensors. In recent years, it has become practical to create computer images in three spatial dimensions instead of two. With this capability, more information can be represented visually. This allows for more complex mathematical entities, such as the Reynolds stress tensor, to now have complete visual representations. These representations are called tensor glyphs.

This thesis was motivated by prior problems associated with presenting the Reynolds stress tensor. In a previous investigation by Moore, et al. [1], Reynolds stresses in a tip leakage turbine cascade were measured. These measurements were made with

respect to a set of coordinate axes whose orientation was arbitrarily defined. It was unclear for this complex flow geometry, however, which coordinate axes orientation was best suited for the presentation of the Reynolds stress tensor components. A representation of the stress tensor that was independent of any coordinate system was therefore desired. In addition, the final presentation of the Reynolds stress components, shown in Figure 1 [1], turned out to be difficult to interpret visually. The development of a tensor glyph appeared to be a possible solution to both of these problems. Inspired by the work of Kriz [2] and his presentation of a fourth order stiffness tensor, shown in Figure 2 [2], work began on applying the latest tensor visualization techniques to the problem of representing the Reynolds stress tensor. This thesis is the direct result of these efforts.

In the present investigation, developments in turbulence modeling up to second moment closure methods are discussed as a review of the various ways in which the Reynolds stress tensor can be calculated. Afterwards, the basic principles of classical stress mechanics are introduced. These principles form the basis upon which the tensor glyph is created. Various types of tensor glyphs currently used in stress mechanics are then presented, and an original glyph construction is developed. This new glyph type is designed to convey as much information about the Reynolds stress tensor as possible in a manner that is easy to understand visually. Based upon experimental measurements, these glyphs are created for the Reynolds stress tensor corresponding to: a) Reynolds stress component measurements, b) the Boussinesq approximation, and c) an Algebraic

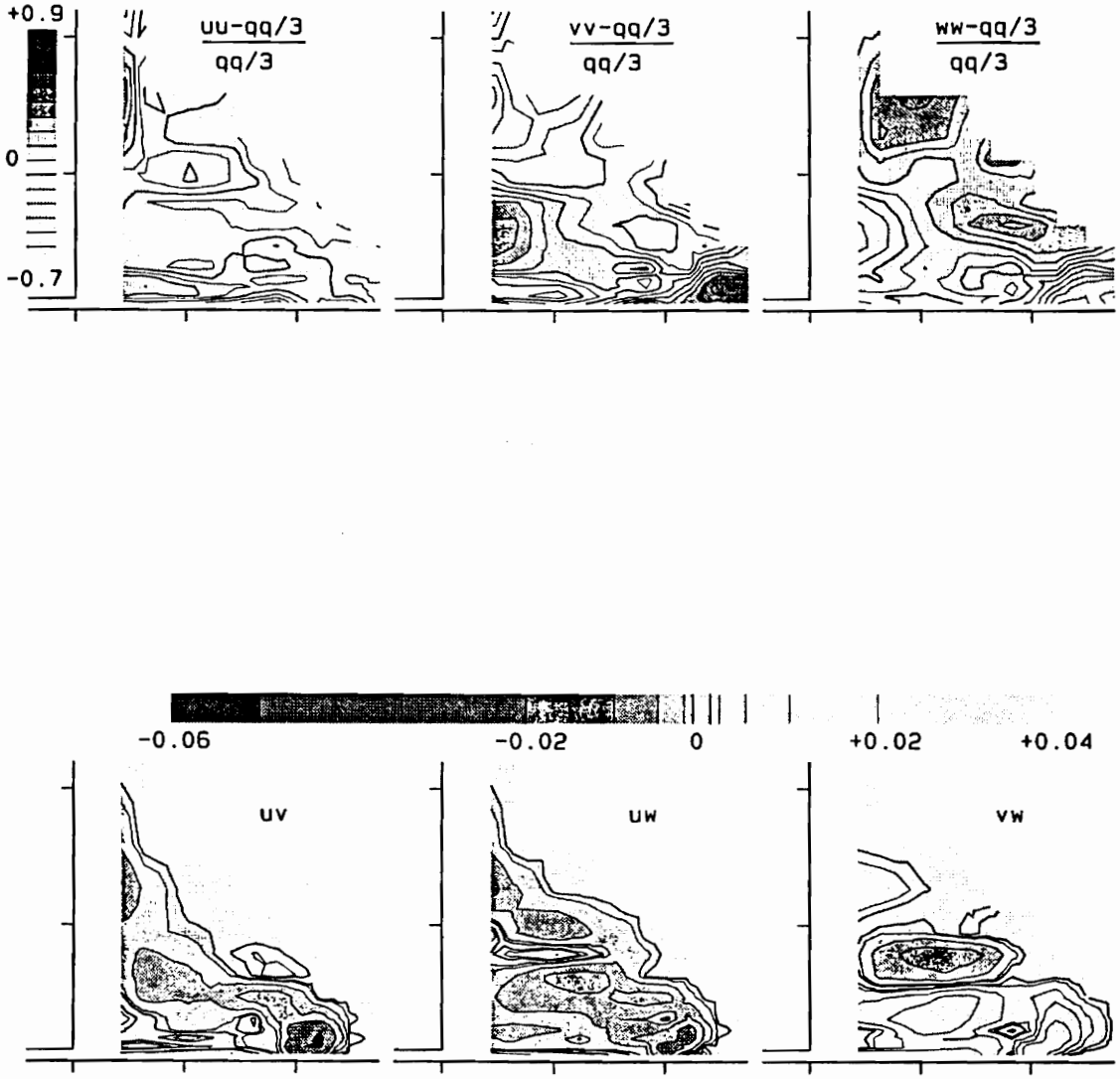

Fig. 1 Reynolds stress component plots [1]

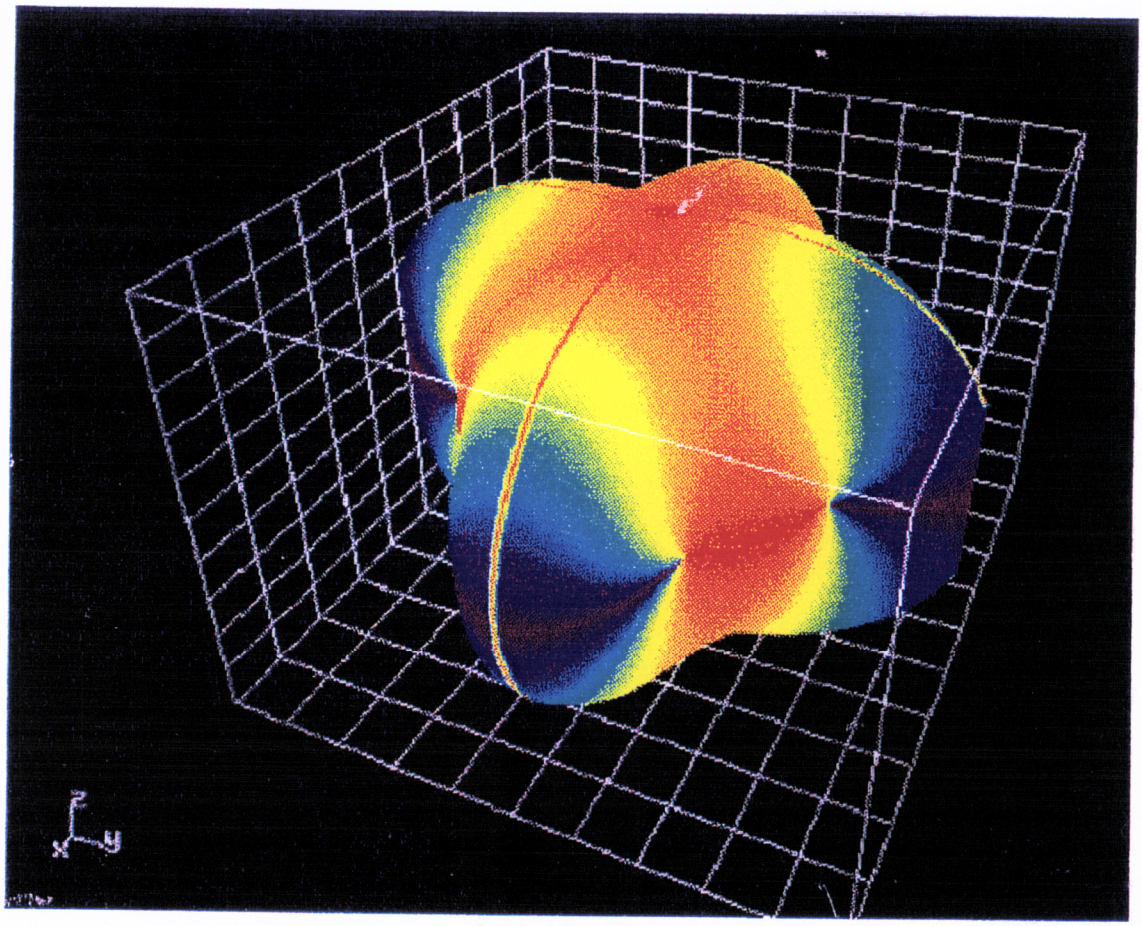

Fig. 2 A fourth order stiffness tensor [2]

Reynolds Stress Model (ARSM). By comparing the glyphs, the accuracy of the two turbulence models can be evaluated. With these three sets of glyphs, the answers to two basic questions are sought:

1) How well does the glyph represent the Reynolds stress tensor compared to the traditional method of plotting individual stress components?

2) Are there any fundamental advantages given by modeling the Reynolds stress tensor with a simple second moment closure method such as an ARSM rather than using models based upon the Boussinesq approximation?

With these two questions in mind, a simple geometry, fully developed pipe flow, and a complex geometry, the tip leakage turbine cascade, are both considered.

In summary, the present work is an attempt to apply the latest tensor visualization techniques to the study of the Reynolds stress tensor and the field of turbulence modeling. In doing this, it is hoped that a deeper understanding of the Reynolds stress tensor and the requirements of an effective turbulence model will be gained.

2.0 Literature Review

2.1 Turbulence Modeling and the Problem of Closure

The accurate prediction of turbulent fluid flow properties has been an ongoing goal of scientists and engineers for over 100 years. The exact calculations of turbulent flows in even the most simple geometries have, to this day, remained outside the capabilities of available mathematical tools. As a result, approximate models are needed to make any predictions concerning turbulent flow quantities.

Osborne Reynolds [3] first proposed the idea that turbulent flow quantities could be determined by decomposing the Navier-Stokes equations into mean and fluctuating components and averaging the resulting equations over time. Given a turbulent flow quantity, A, the time average is given by:

$$\overline{A} = \frac{1}{T}\int_0^T A(t)dt \qquad (1)$$

where the time scale, T, is much longer than the time scale of the turbulent fluctuations and much smaller than the time scale of the mean motion.

Using this time averaging technique for an incompressible, constant temperature, turbulent flow of a Newtonian fluid where body forces are negligible, the application of Reynolds' technique to the momentum equations gives:

$$\rho\left(\frac{\partial U_i}{\partial t} + U_j \frac{\partial U_i}{\partial x_j}\right) = -\frac{\partial P}{\partial x_i} + \frac{\partial}{\partial x_j}\left(\mu\left(\frac{\partial U_i}{\partial x_j} + \frac{\partial U_j}{\partial x_i}\right) - \rho\overline{u_i u_j}\right) \quad (2)$$

Here, the capital letters denote mean flow quantities and the lower case letters represent fluctuating values. It can be seen that Reynolds' time averaging has introduced a new unknown into the equation, $-\rho\overline{u_i u_j}$. This is the time averaged correlation between the velocity fluctuations of U_i and U_j. This quantity represents a stress in the flow due to the turbulent fluctuations, and has been named, after Osborne Reynolds, the Reynolds stress. The nine components comprise the Reynolds stress tensor.

The addition of new quantities in the Navier-Stokes equations makes the number of unknowns greater than the number of equations. This is known as the problem of closure for the time averaged Reynolds equations. In order to make the number of unknowns and equations equal, it is necessary to introduce new relations for the Reynolds stresses in terms of variables already existing in the other equations. These additional relations are the turbulence models.

Turbulence models of increasing sophistication have appeared since Reynolds first introduced his time averaged equations. In general, these can be classified as algebraic, one equation, two equation, and second moment closure methods. It will be seen that the algebraic, one equation, and two equation models are based upon an approximation introduced in 1877 by Boussinesq [4].

2.1.1 The Boussinesq Approximation

The Boussinesq approximation, put simply, states that Reynolds stresses can be modeled in analogy to fluid stresses due to molecular forces. For Newtonian fluids, molecular stresses were found to be proportional to the rates of strain in the fluid. The proportionality constant was the fluid viscosity, μ. Similarly, Boussinesq proposed that a turbulent or eddy viscosity, μ_t, could be introduced to model the Reynolds stresses. The Reynolds stress terms in the equation could now be replaced with the expression:

$$-\overline{u_i u_j} = \nu_t\left(\frac{\partial U_i}{\partial x_j} + \frac{\partial U_j}{\partial x_i}\right) - \frac{2}{3}k\delta_{ij} \tag{3}$$

Here, ν_t is the kinematic turbulent viscosity. This is simply the turbulent viscosity divided by the density. The k in this equation is the turbulence kinetic energy and is defined as:

$$k = \frac{1}{2}\left(\overline{u_1^2} + \overline{u_2^2} + \overline{u_3^2}\right) \tag{4}$$

The addition of the k term was not originally suggested by Boussinesq, rather, it was later found to be necessary in order for the Boussinesq approximation to be applicable to normal Reynolds stresses. Without the addition of this term, the sum of the normal stresses will always be zero for incompressible flows due to the continuity equation.

With the Boussinesq approximation, the distribution of the turbulent viscosity, μ_t, still needs to be determined. It is the purpose of the algebraic, one equation, and two equation models to provide this determination.

2.1.1.1 Algebraic Turbulence Models

The earliest and simplest proposed turbulence models were algebraic models. These models prescribe an algebraic distribution for the eddy viscosity in terms of the flow geometry.

The first such model was introduced by Prandtl [5], and is commonly known as the Prandtl mixing length hypothesis. Essentially, Prandtl derives a relationship between a turbulence length scale, called the mixing length, and the turbulent viscosity. He then introduces algebraic relations for the length scale determination. In analogy to kinetic gas theory, Prandtl assumed, by dimensional arguments, that the eddy viscosity was proportional to a characteristic velocity and a characteristic length scale. He then reasoned that the characteristic velocity was equal to the characteristic length scale multiplied by the mean flow velocity gradient. As a result, Prandtl's mixing length model is

$$\nu_t = l_m^2 \left| \frac{\partial U}{\partial y} \right|, \tag{5}$$

where the length scale, l_m, is called the mixing length. This relation applies only to two dimensional shear layer flows where the normal direction is y. Rodi [6] gives a mixing length model that applies to more general flows. It takes the form:

$$\nu_t = l_m^2 \left[\left(\frac{\partial U_i}{\partial x_j} + \frac{\partial U_j}{\partial x_i} \right) \frac{\partial U_i}{\partial x_j} \right]^{1/2} \tag{6}$$

To close the problem set, the distribution of the length scale needs to be determined. This distribution takes the form of algebraic relations based upon flow geometry. While these relations are fairly simple for shear layer flows, the mixing length prescription becomes much more difficult for more general flows.

The defining feature for all algebraic turbulence models is the determination of the magnitude of turbulence through local flow properties. The magnitude of the eddy viscosity or the mixing length at a given point is determined solely from the position in the flow. This type of formulation ignores any transport effects of turbulence quantities. As a result of this shortcoming, more sophisticated transport equation models were introduced.

2.1.1.2 One Equation Models

In order to produce turbulence models applicable to more general flow situations, researchers needed to include a transport equation for a turbulence quantity. The commonly accepted quantity to consider for this additional transport equation is the turbulence kinetic energy. By including a transport equation for turbulence kinetic energy,

convective and diffusive effects could now be considered. For high Reynolds number flows the transport equation for turbulence kinetic energy can be written as:

$$\frac{\partial k}{\partial t} + U_i \frac{\partial k}{\partial x_i} = -\frac{\partial}{\partial x_i}\left[\overline{u_i\left(\frac{u_j u_j}{2} + \frac{p}{\rho}\right)}\right] - \overline{u_i u_j}\frac{\partial U_i}{\partial x_j} - \nu\overline{\frac{\partial u_i}{\partial x_j}\frac{\partial u_i}{\partial x_j}} \qquad (7)$$

The terms in this equation can be thought of as convective transport, diffusion, production, and viscous dissipation of the turbulence kinetic energy. Note that the production of turbulence kinetic energy is commonly expressed as

$$P = -\overline{u_i u_j}\frac{\partial U_i}{\partial x_j}. \qquad (7.a)$$

As with the mean momentum equation, terms involving fluctuation correlations need to be modeled in terms of variables already existing in the equation set. With the addition of these models, the distribution of the turbulence kinetic energy can be calculated. The modeled form of the k equation usually takes the form of:

$$\frac{\partial k}{\partial t} + U_i \frac{\partial k}{\partial x_i} = -\frac{\partial}{\partial x_i}\left(\left[\nu + \frac{\nu_t}{\sigma_k}\right]\frac{\partial k}{\partial x_i}\right) + \nu_t\left(\frac{\partial U_i}{\partial x_j} + \frac{\partial U_j}{\partial x_i}\right)\frac{\partial U_i}{\partial x_j} - C_d\frac{k^{3/2}}{L} \qquad (8)$$

This equation is based upon heuristic arguments and extrapolations of the knowledge of simplified turbulence situations. The terms σ_k and C_d are empirical constants that are determined from experimental measurements.

Since k is a direct measure of the intensity of the turbulent velocity fluctuations, it followed that $\sqrt{k}$ could be used as a velocity scale in determining the eddy viscosity. As described by Rodi [6], two researchers, Prandtl and Kolmogorov, both independently proposed this procedure. As a result, the new expression for the eddy viscosity,

$$\nu_t = C_\mu' \sqrt{k} L, \tag{9}$$

is known as the Kolmogorov-Prandtl eddy viscosity formulation. From this and the Boussinesq approximation, the Reynolds stresses can be determined.

In the Kolmogorov-Prandtl expression, the length scale L, needs to be prescribed for the problem to be closed. The determination of L is, in general, accomplished in exactly the same manner as l_m is in the algebraic turbulence models. As a result, the limitations for determining l_m also apply to the determination of L. To overcome these limitations, researchers proposed introducing another transport equation; an equation for the length scale.

2.1.1.3 Two Equation Models

The problems associated with developing a general algebraic formula for the length scale, L, stimulated the proposal for introducing another differential transport equation for this quantity. It was not necessary, however, to derive an equation for a length scale specifically. Instead, since a transport equation for k existed, any quantity that was a combination of k and L in the form $k^m L^n$ could be used as a second independent variable in the two equation set. Perhaps the most popular choice for this combination is the turbulence dissipation rate, ε, which is proportional to $k^{3/2}/L$. A list of more commonly known variations of $k^m L^n$ is listed in Rodi [6]. Just as with the turbulence kinetic energy equation, the second transport equation can be derived from the Navier-Stokes equations or it may be developed heuristically. In either case, modeling assumptions are required to close the equation set. With the models, the second transport equation takes the form:

$$\frac{\partial Z}{\partial t} + U_i \frac{\partial Z}{\partial x_i} = \frac{\partial}{\partial x_i}\left(\frac{C_\mu' \sqrt{k} L}{\sigma_Z} \frac{\partial Z}{\partial x_i}\right) + C_{Z1} \frac{Z}{k} P - C_{Z2} Z \frac{\sqrt{k}}{L} + S \qquad (10)$$

where Z is the form of the length scale, S is a source term, and σ_z, C_{z1}, and C_{z2} are empirical constants that are again obtained from experimental data.

It should be noted that the two equation models, as with the one equation and algebraic models, still employ the Boussinesq approximation. As a result, the relative

magnitudes of the Reynolds stress components at a given point are related to the mean flow through the strain rate tensor. For complex flows, this relation for the Reynolds stress components may be too simplified to match the actual flow. The transport of the individual turbulent stresses may need to be modeled. For this reason, differential transport equations have been derived and applied, with modeling approximations, to close the turbulence equation set.

2.1.2 Second Moment Closure Methods

The concept of deriving equations for the Reynolds stresses directly, instead of relating them to the mean flow, and using these additional equations to close the turbulence equation set, comprise the second moment closure methods. These additional equations will, unfortunately, contain fluctuation correlations of still higher levels so that there will always be more unknowns than equations. Modeling approximations will still need to be introduced.

2.1.2.1 Full Reynolds Stress Models

The Reynolds stress transport equations can be derived by manipulating the Navier-Stokes equations. This was first demonstrated by Chou and is described by Launder, et al., [7]. These equations are given as:

$$\frac{D\overline{u_i u_j}}{Dt} = -\left[\overline{u_j u_k}\frac{\partial U_i}{\partial x_k} + \overline{u_i u_k}\frac{\partial U_j}{\partial x_k}\right] - 2\nu\overline{\frac{\partial u_i}{\partial x_k}\frac{\partial u_j}{\partial x_k}} + \overline{\frac{p}{\rho}\left(\frac{\partial u_i}{\partial x_j} + \frac{\partial u_j}{\partial x_i}\right)}$$

Convection | P_{ij}=Production | Dissipation | Pressure Strain

$$-\frac{\partial}{\partial x_k}\left[\overline{u_i u_j u_k} - \nu\frac{\partial \overline{u_i u_j}}{\partial x_k} + \overline{\frac{p}{\rho}\left(\delta_{jk}u_i + \delta_{ik}u_j\right)}\right] \qquad (11)$$

Diffusion

All the terms in this equation except for the convective transport and the stress production terms involve unknown correlation quantities, and will therefore have to be modeled. The work of Hanjalic and Launder[8] is a widely regarded early stress transport modeling effort. They obtained:

$$\frac{D\overline{u_i u_j}}{Dt} = -\left[\overline{u_j u_k}\frac{\partial U_i}{\partial x_k} + \overline{u_i u_k}\frac{\partial U_j}{\partial x_k}\right] - \frac{2}{3}\delta_{ij}\varepsilon + \left(\phi_{ij} + \phi_{ji}\right)_1 + \left(\phi_{ij} + \phi_{ji}\right)_2$$

$$+C_s\frac{\partial}{\partial x_k}\frac{k}{\varepsilon}\left[\overline{u_i u_l}\frac{\partial \overline{u_j u_k}}{\partial x_l} + \overline{u_j u_l}\frac{\partial \overline{u_k u_i}}{\partial x_l} + \overline{u_k u_l}\frac{\partial \overline{u_i u_j}}{\partial x_l}\right] \qquad (12)$$

where

$$\left(\phi_{ij} + \phi_{ji}\right)_1 = -C_1\frac{\varepsilon}{k}\left(\overline{u_i u_j} - \delta_{ij}\frac{2k}{3}\right) \qquad (12.a)$$

$$\left(\phi_{ij} + \phi_{ji}\right)_2 = \frac{\partial U_l}{\partial x_m}a_{lj}^{mi} + \frac{\partial U_l}{\partial x_m}a_{li}^{mj} \qquad (12.b)$$

Together, Equations (12.a) and (12.b) form the model for the pressure strain term found in Equation (11). The fourth order tensor, a, found in Equation (12.b) is modeled as a complex linear combination of Reynolds stresses. For more details see Hanjalic and Launder [8]. Launder et al. [7] greatly simplify the model of $\left(\phi_{ij} + \phi_{ji}\right)_2$. They proposed:

$$\left(\phi_{ij} + \phi_{ji}\right)_2 = -\gamma\left(P_{ij} - \frac{2}{3}P\delta_{ij}\right). \qquad (12.c)$$

It should be noted that in addition to Reynolds stresses, mean flow values and their respective gradients, both k and ε also appear in the modeled Reynolds stress transport equations. It is therefore necessary to include the transport equations for these quantities as well, in order for the problem to be closed.

2.1.2.2 Algebraic Reynolds Stress Models

The effort to simultaneously solve differential equations for the six Reynolds stress components, as well as continuity, momentum, the turbulence velocity scale, and the length scale is a formidable task, even at today's computational speeds. To help alleviate this computational burden, simplifications were sought to reduce the differential Reynolds stress equations to algebraic ones. This was first accomplished by Rodi [9] and is detailed in Appendix A. Rodi's algebraic expression for the Reynolds stresses is:

$$\overline{u_i u_j} = k\left[\frac{2}{3}\delta_{ij} + \frac{(1-\gamma)\left(P_{ij} - \frac{2}{3}P\delta_{ij}\right)}{(C_1 - 1)\varepsilon + P}\right] \tag{13}$$

Here, C_1 and γ are empirical constants. This is an example of an Algebraic Reynolds Stress Model (ARSM) and is one of the simplest formulations for the direct prescription of the individual Reynolds stresses. This ARSM formulation will be analyzed throughout this work.

2.2 Stress Mechanics Review

In assessing a particular turbulence model's effectiveness in predicting the Reynolds stress tensor by using visualization techniques, it is necessary to use many of the principles of classical stress mechanics. For this reason, a brief review of the basic tenets of stress mechanics is given here. This review is based upon analyses and development given by Frederick and Chang [10] and Beer [11].

2.2.1 The Stress Tensor

The idea of a stress vector acting upon a given medium can be simply understood by considering a planar surface area, ΔS, oriented by the unit normal vector n_i, with a

total force, ΔF_i, acting across the surface. This is shown in Figure 3 [10]. The stress vector σ_i, can then be defined in the limit as:

$$\sigma_i = \lim_{\Delta S \to 0} \frac{\Delta F_i}{\Delta S} = \frac{dF_i}{dS}. \tag{14}$$

Note that the orientation of the unit normal, n_i, influences the magnitude and direction of the total force upon the surface and therefore influences the stress vector.

The stress vector can be broken down into two components, one in the direction of the unit normal, the normal stress, and one in the plane of the surface, the shearing stress. If an orthogonal coordinate system is defined so that n_i is in the positive y_1 direction, the shearing stress can be further broken down into two components in the y_2 and y_3 directions. The components of stress on a surface oriented normal to n_i are denoted σ_{i1}, σ_{i2}, and σ_{i3}; the first index indicating the surface normal direction and the second index indicating the direction of the stress. This can be seen in Figure 4 [10]. This procedure can also be applied to surfaces oriented normal to the positive y_2 and y_3 axes. The components of stress in the three orthogonal planes completely represent the state of stress at a point. Taken together, they are called the stress tensor and are denoted as σ_{ij}.

The stress tensor can be visually represented by considering a cubic element of infinitesimal proportions as shown in Figure 5. The three faces of the cubic element oriented normal to the negative y_1, y_2, and y_3 directions have stress vectors that are

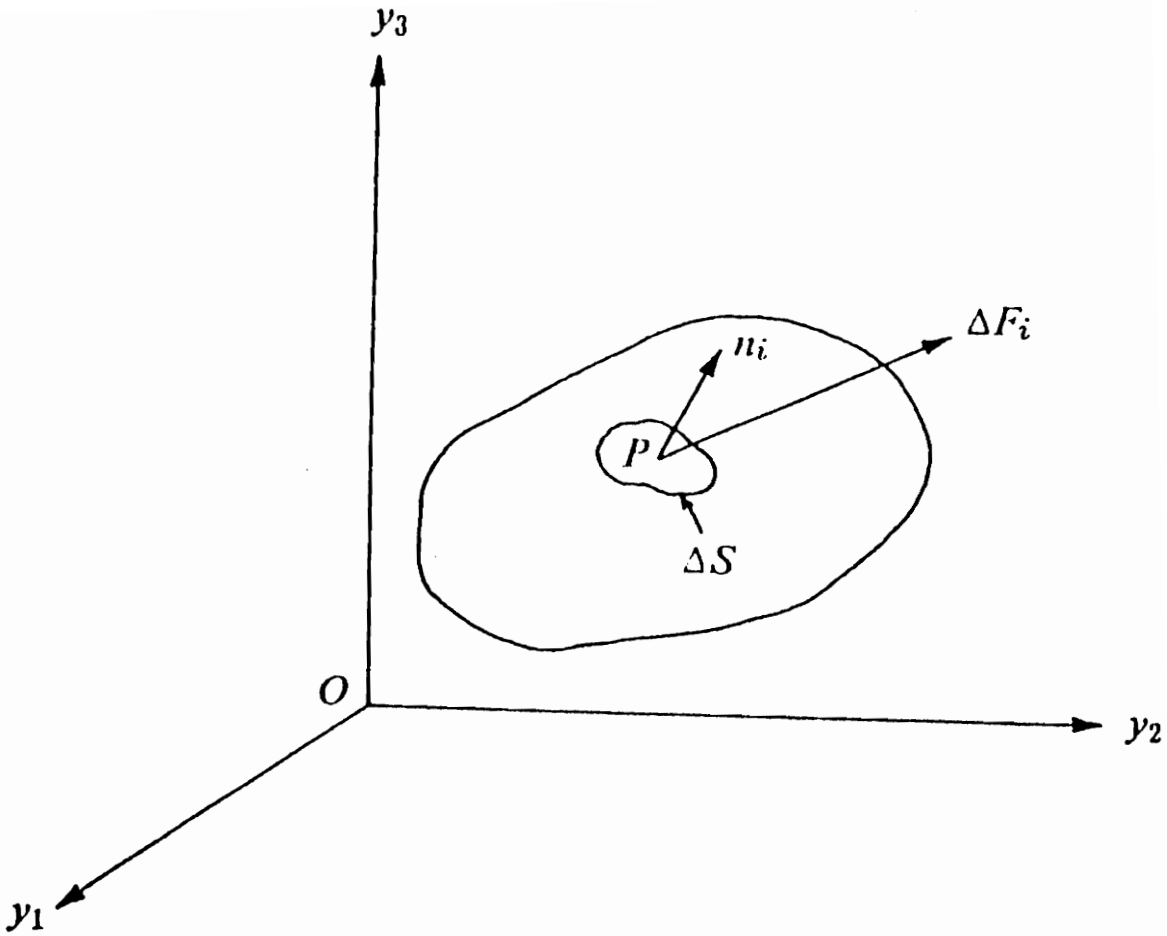

Fig. 3 Generalized State of Stress [10]

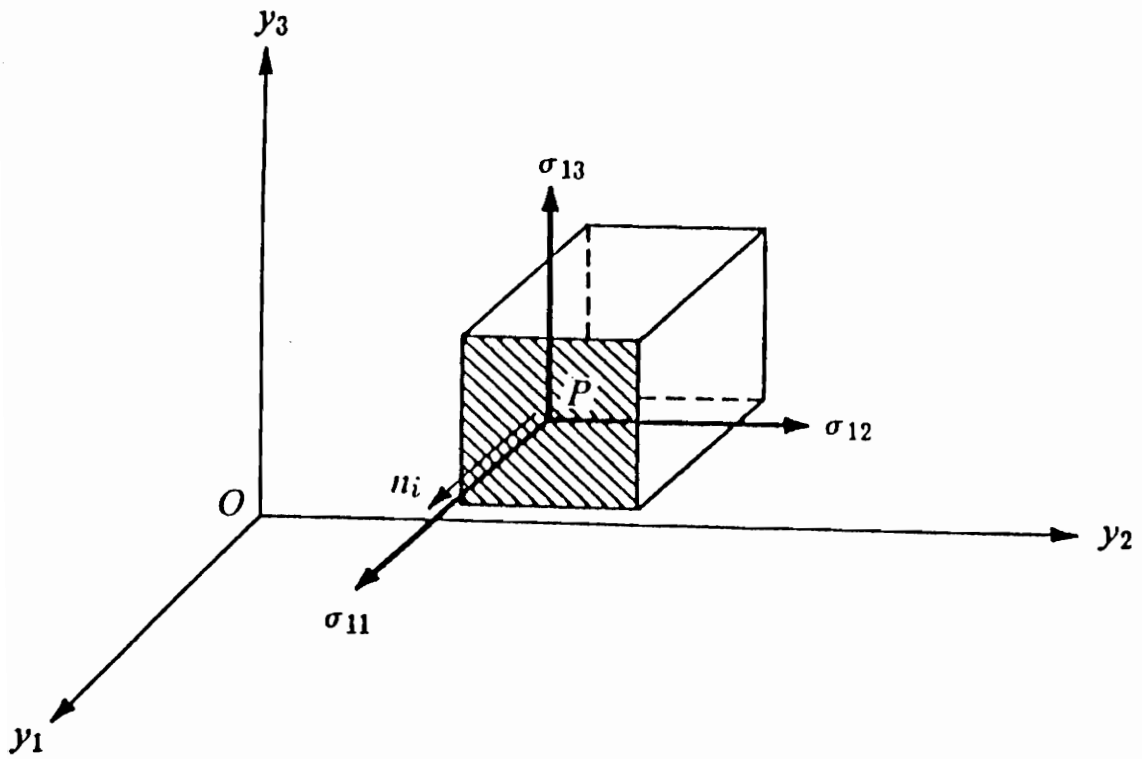

Fig. 4 A Control Surface for a Stress Vector [10]

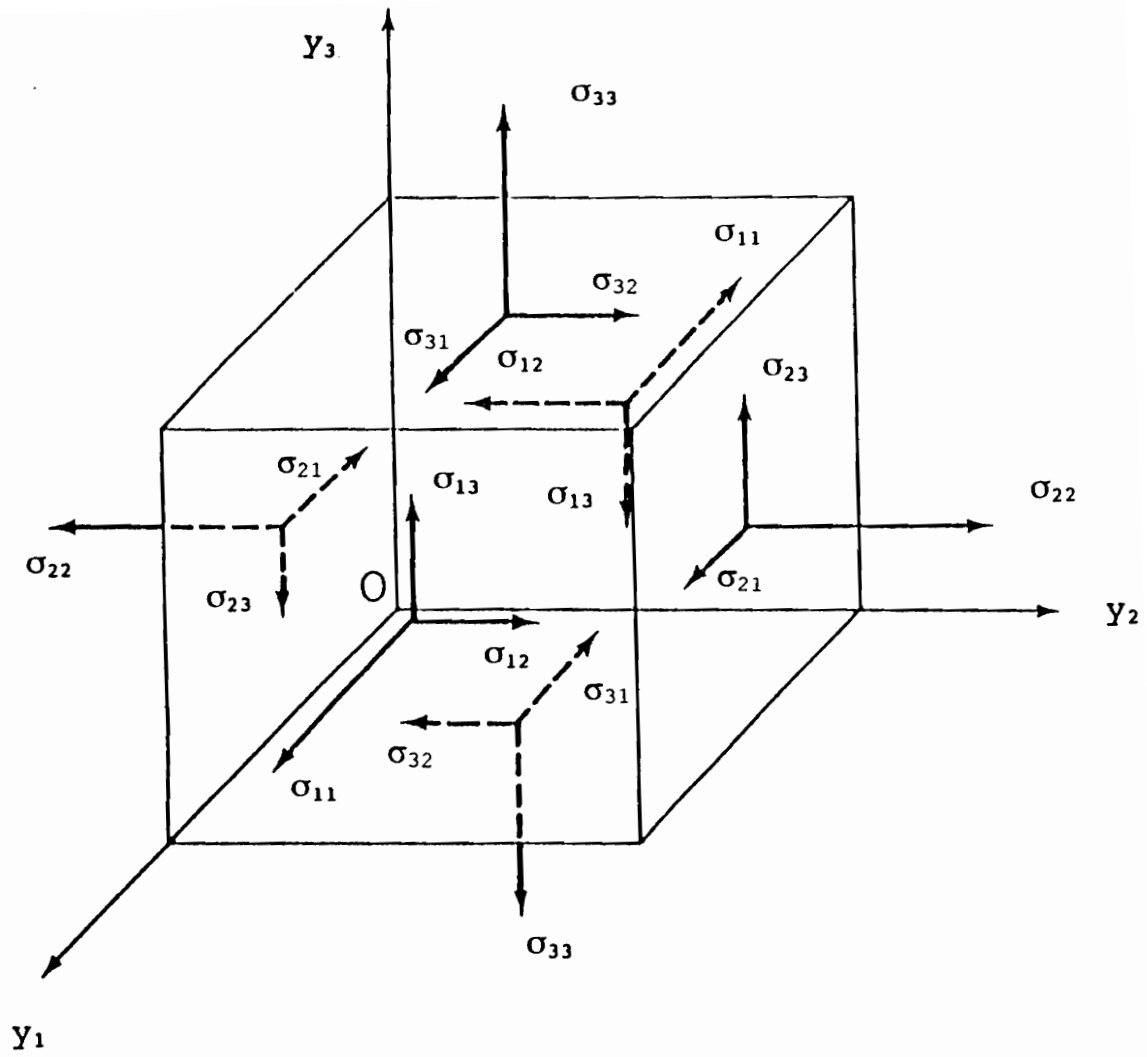

Fig. 5 A Cubic Element for a State of Stress

reactions to the stress vectors on their respective positive face counterparts. The stress components on these faces, therefore, are equal in magnitude and opposite in sign to the stress components on the opposite faces.

The stress vector σ_i can be simply related to the stress components σ_{ij} by considering a tetrahedron oriented with the coordinate axes and having an arbitrary sloping face defined by the unit normal n_i. This is shown in Figure 6 [11]. Assume the tetrahedron is under a state of stress by surface forces and allow for body forces. If simple force equilibrium equations are applied, and the limit is taken as the tetrahedron dimensions go to zero, there results:

$$\sigma_i = \sigma_{ji} n_j . \tag{15}$$

Additionally, with the use of moment and force equilibrium equations on an arbitrary region in which no body moments are present, it can be shown that:

$$\sigma_{ij} = \sigma_{ji} \tag{16}$$

In other words, the stress tensor is symmetric. It has been shown that the Reynolds stress tensor [12] and the strain rate tensor [13] considered in this thesis are both symmetric tensors. As a consequence, there are only six independent component values of these tensors.

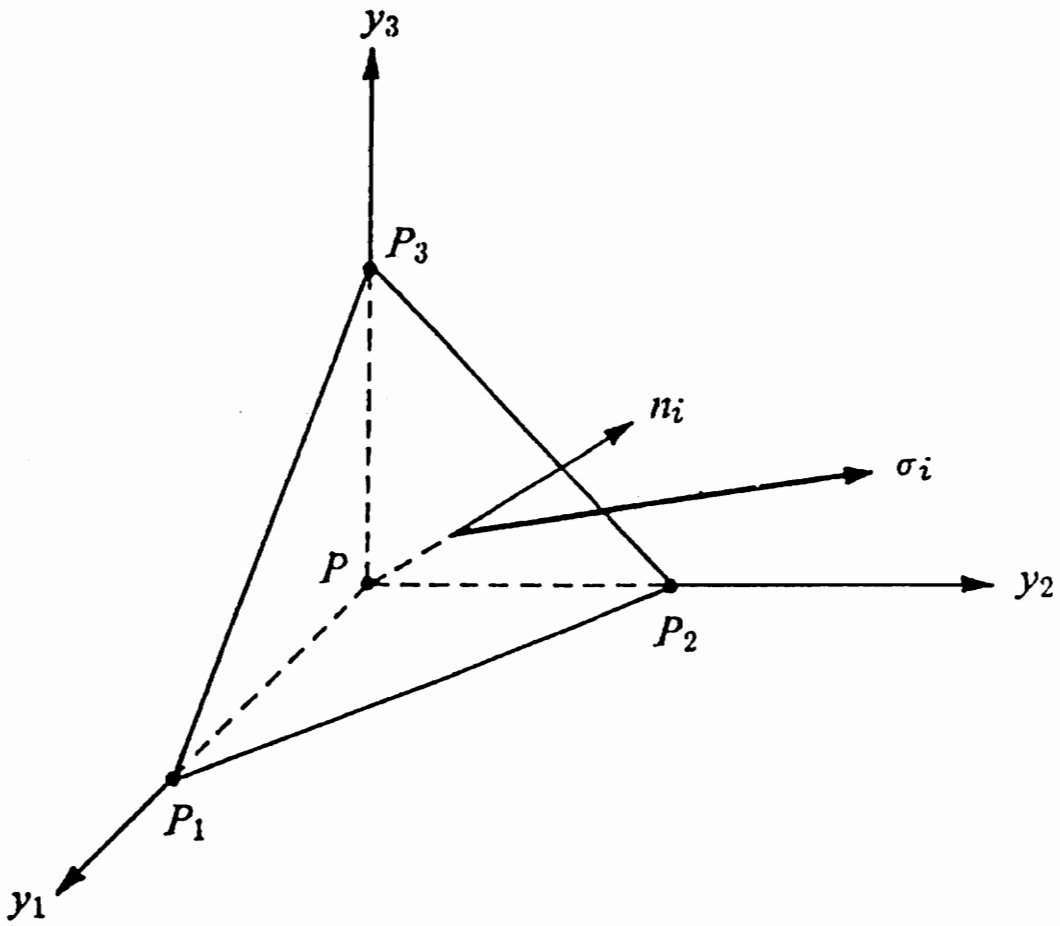

Fig. 6 A Stress Tetrahedron[11]

2.2.2 Transformation of the Stress Tensor

The transformation of the stress tensor to different coordinate systems can be derived by considering two sets of orthogonal coordinate systems; y_1, y_2, y_3 and y_1', y_2', y_3', as shown in Figure 7 [11]. A stress element can be described in each coordinate system with a unit normal vector, a stress vector, and a stress tensor. The goal here is to relate the stress tensors of the primed and unprimed systems.

First, the relations between the two vector quantities, the normal and stress vectors, in each system need to be established. In Cartesian coordinate systems, vectors follow the transformation laws of a Cartesian tensor quantity of order 1. Therefore:

$$n'_i = a_{ij} n_j \tag{17a}$$

$$n_j = a_{ij} n'_i \tag{17b}$$

$$\sigma'_i = a_{ij} \sigma_j \tag{17c}$$

$$\sigma_j = a_{ij} \sigma'_i, \tag{17d}$$

where a_{ij} is the transformation matrix between the primed and unprimed coordinate systems. The relations between stress vectors in the two coordinate systems given in Equations (17c) and (17d) can be manipulated first by substituting in the relations between the stress tensor and stress vector given in Equation (15), and then by substituting in the relations between the normal vectors in both coordinate systems given in Equations (17a) and (17b). After a little tensor algebra the relation of the form

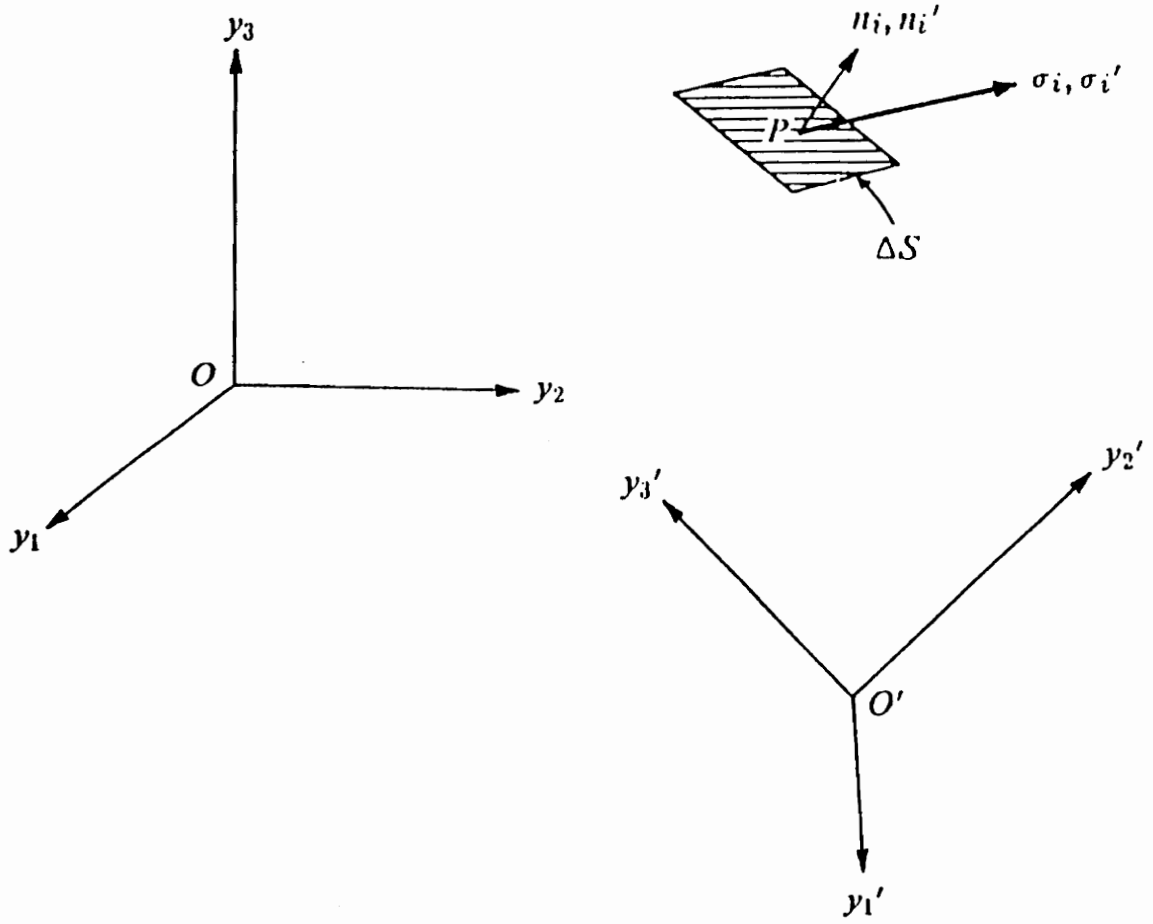

Fig. 7 Rotated Coordinate Systems [11]

$$\sigma'_{ij} = a_{ir}a_{js}\sigma_{rs} \tag{18}$$

can be derived . This is the general form of the transformation law of a Cartesian tensor of order 2. Because the stress components transform in such a way, it is justified to call the state of stress at a point a stress tensor. This transformation equation can be re-expressed in more convenient notation for a normal stress component in an arbitrary direction as:

$$\sigma = d_1^2\sigma_{11} + d_2^2\sigma_{22} + d_3^2\sigma_{33} + 2\left(d_2d_3\sigma_{23} + d_3d_1\sigma_{31} + d_1d_2\sigma_{12}\right), \tag{19}$$

where d_1, d_2, and d_3 are the components of the unit direction vector of the normal stress σ [14]. This form will be used later in constructing tensor glyphs.

2.2.3 Principal Values and Principal Directions

It is convenient to express the elements of the stress tensor in a coordinate system in which the stress vectors acting upon the coordinate planes are exactly aligned with the plane's unit normal. The magnitude of the stresses satisfying this condition are called the principal stresses and their orientations are the principal directions. This can be formulated as:

$$\sigma_i = \sigma_p n_i \tag{20}$$

where σ_p is a principal stress value and n_i is a principal stress direction. Since the unit normal and the stress vector are aligned in the same direction, the shearing stress on this plane is zero.

The magnitudes of the principal stresses and the orientations of the principal directions depend on the stress tensor. They can be determined through a standard eigenvalue/eigenvector formulation of the stress quantities. Equating previous relations:

$$\sigma_i = \sigma_{ji} n_j = \sigma_p n_i = \sigma_p \delta_{ij} n_j, \tag{21}$$

the standard eigenvalue problem can be derived as

$$\left(\sigma_{ij} - \sigma_p \delta_{ij}\right) n_j = 0. \tag{22}$$

Trivial solutions for this equation exist as $n_j = 0$. For non-trivial solutions, the coefficient of the unit vector n_j must equal zero. Since the coefficient of n_j is a 3 x 3 matrix, this solution can be determined by equating its determinant with zero. This will result in three values for the principal stresses. The principal directions can then be determined by using the values for the principal stresses to solve for n_j.

It can be shown that for a tensor with only real components, its principal values will also always be real. This condition is satisfied for all stress tensors. Additionally, if

each of the principal stresses is distinct, then the principal stress directions will form an orthogonal coordinate system.

Although the method described above is the standard way of determining principal values and directions, for the sake of simplicity, an algorithm given in Numerical Recipes in FORTRAN [15]was used to determine these quantities. A brief description of the method is given in Appendix B.

2.2.4 Mohr's Circles

A simple geometrical tool called the Mohr's circle can be used to determine transformation relations in the case of plane stress. Conditions for plane stress are met if two faces on a cubic element are free of any stress. However, the Mohr's circle is also a useful tool in understanding transformations for a more general state of stress in planes rotating about principal stress axes.

Consider a cubic element in a state of planar stress so that the only non-zero stress components are σ_{11}, σ_{22}, and σ_{12}. This is shown in Figure 8 [11]. If this element is rotated about the y_3 axis by an angle θ, so that the element is now in the y_1', y_2', y_3 coordinate system, as seen in Figure 9 [11], the new normal and shear stresses can be given in terms of the old stresses with the use of Equation (18). In algebraic notation, these relations can be put into the convenient form of:

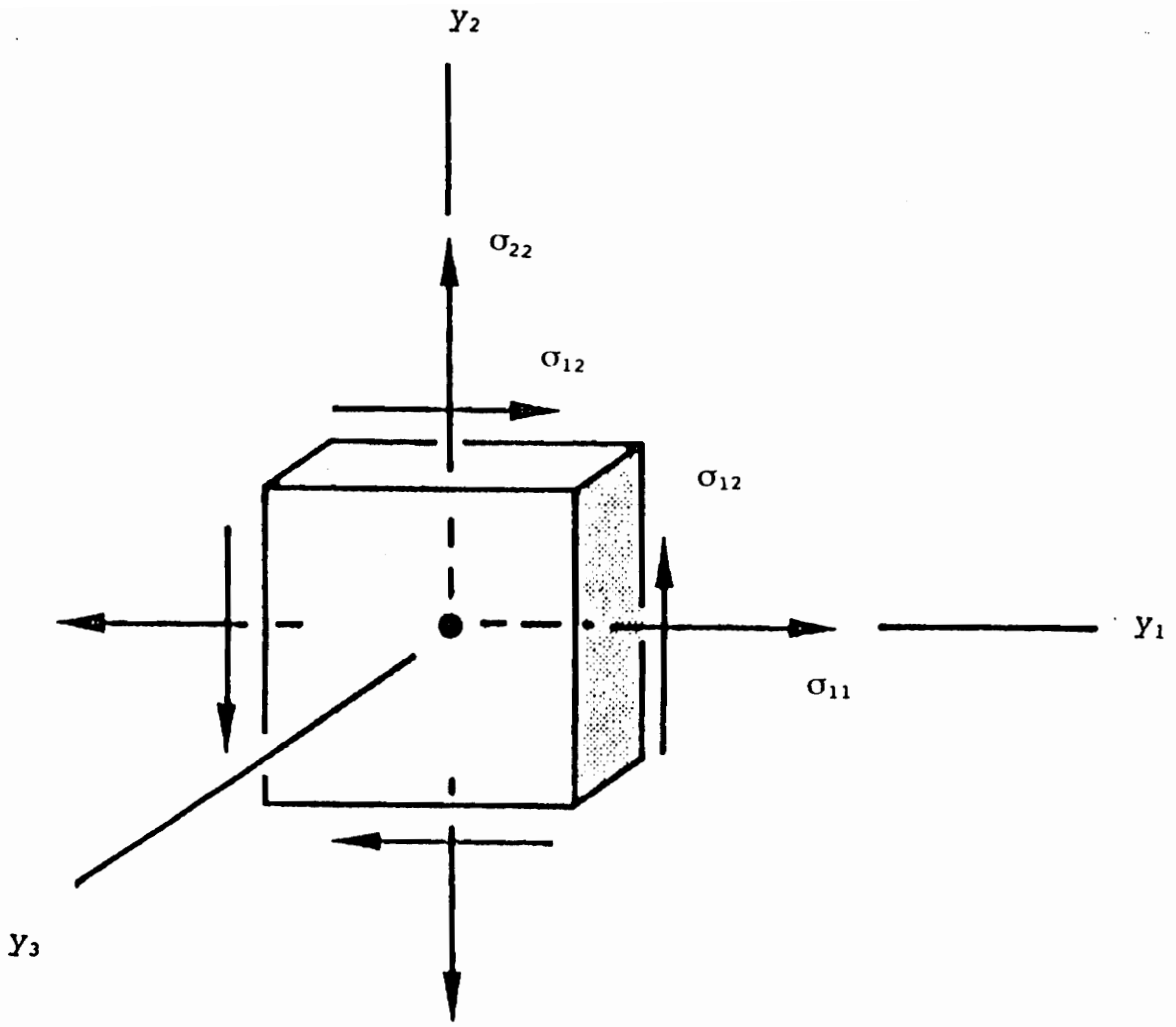

Fig. 8 A Cubic Element Under a State of Planar Stress [11]

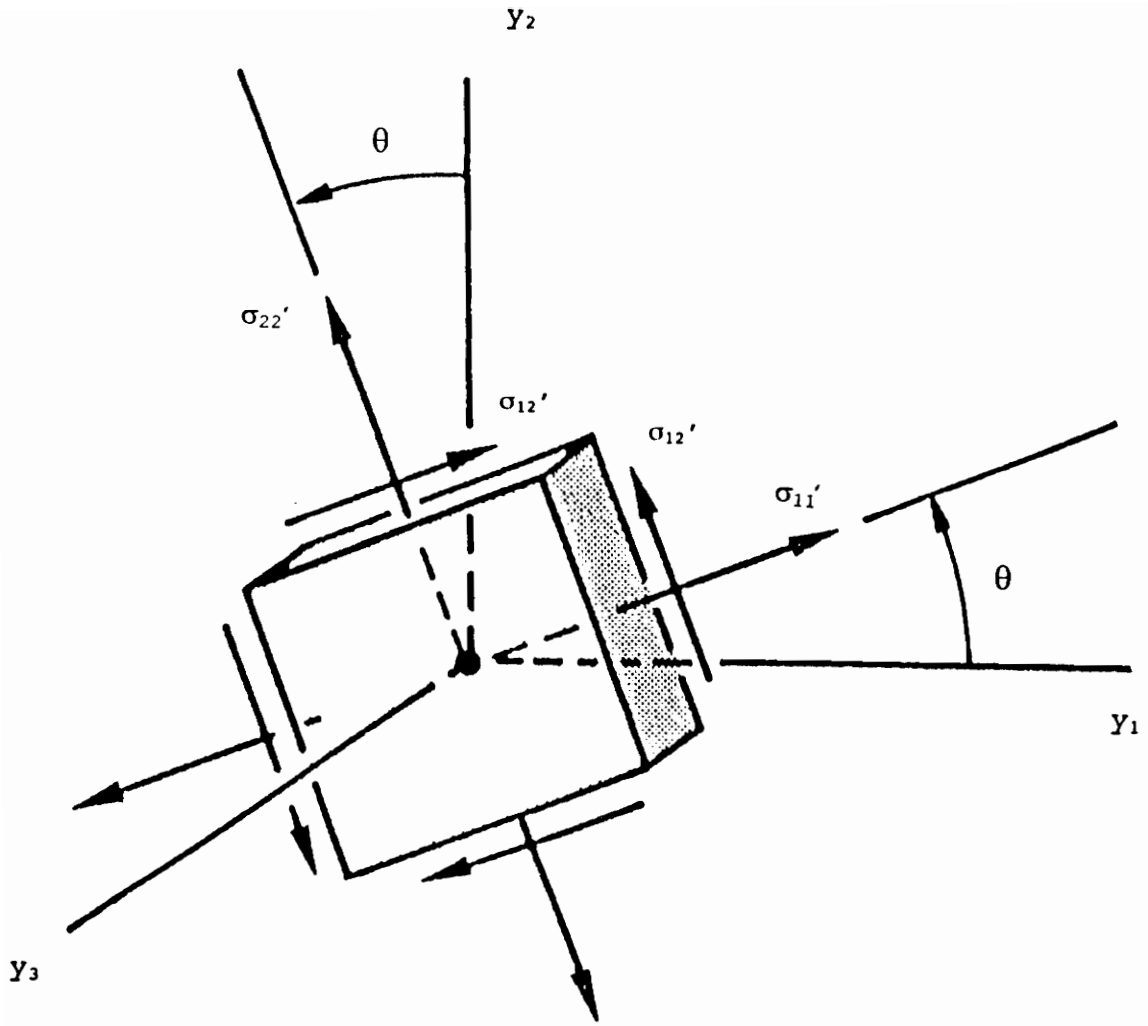

Fig. 9 A Rotated Cubic Element Under a State of Planar Stress [11]

$$\sigma_{11}' = \frac{\sigma_{11} + \sigma_{22}}{2} + \frac{\sigma_{11} - \sigma_{22}}{2}\cos 2\theta + \sigma_{12}\sin 2\theta \tag{23}$$

$$\sigma_{22}' = \frac{\sigma_{11} + \sigma_{22}}{2} - \frac{\sigma_{11} - \sigma_{22}}{2}\cos 2\theta - \sigma_{12}\sin 2\theta \tag{24}$$

$$\sigma_{12}' = -\frac{\sigma_{11} - \sigma_{22}}{2}\sin 2\theta + \sigma_{12}\cos 2\theta\,. \tag{25}$$

Eliminating θ from Equations (23) and (25) yields:

$$\left(\sigma_{11}' - \frac{\sigma_{11} + \sigma_{22}}{2}\right)^2 + \sigma_{12}'^2 = \left(\frac{\sigma_{11} + \sigma_{22}}{2}\right)^2 + \sigma_{12}^2 \tag{26}$$

This form is easily seen in a plane whose axes are defined as a shearing stress and a normal stress as the equation of a circle that is centered upon the point $\left(\frac{\sigma_{11} + \sigma_{22}}{2}, 0\right)$ and has a radius R given by:

$$R = \sqrt{\left(\frac{\sigma_{11} + \sigma_{22}}{2}\right)^2 + \sigma_{12}^2} \tag{27}$$

In this way Equation (26) defines the Mohr's circle. A typical Mohr's circle is shown in Figure 10 [11]. Here, it can be seen that the circle is plotted in the normal and shearing stress coordinate system. The points X and Y on the circle correspond to the states of

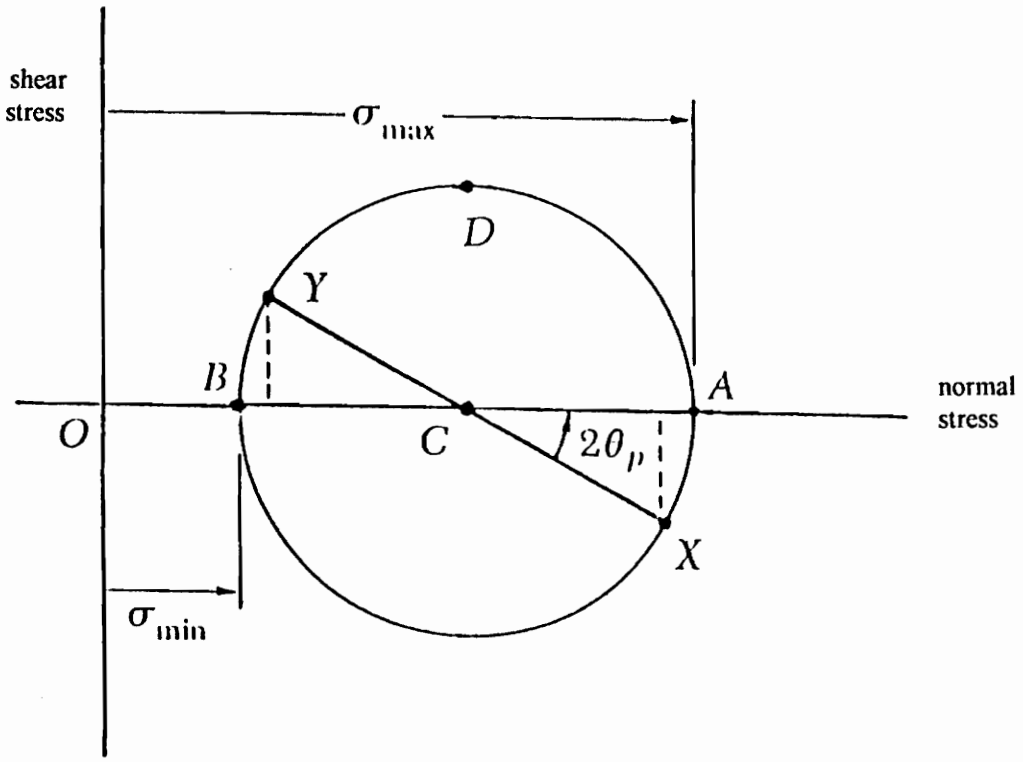

Fig. 10 A Mohr's Circle [11]

stress of the two perpendicular surface planes shown in Figure 8. The coordinate values of points X and Y correspond to the magnitudes of the normal and shearing stresses on these two planes. The effect of the rotation of the cubic element on the stress component values is shown on the Mohr's circle as the rotation of points X and Y about the circle perimeter.

To locate a specific state of stress on the Mohr's circle, it is helpful to remember a few simple rules in determining whether a shear stress should go above or below the normal stress axis. If the shear stress is oriented on an element face so as to rotate the element in a clockwise direction, the shear stress should be located above the normal stress axis. If the shear stress on the face tends to rotate the cubic element in a counterclockwise direction, the shear stress should be located below the normal stress axis. These rules are consistent with the transformation laws.

Recalling the fact that in the principal directions the shear stresses are zero, it is clear that the principal directions correspond to the intersection of the circle with the normal stress axis on the Mohr's circle. This is seen on Figure 10 at the points A and B. By using the shear stress transformation relation given in Equation (25) and setting the transformed shear stress to zero, the rotation angle to principal directions, θ_p, can be given as:

$$\tan 2\theta_p = \frac{2\sigma_{12}}{\sigma_{11} - \sigma_{22}} \tag{28}$$

This equation defines two values of θ_p that are 90° apart, as would be expected. On the Mohr's circle, however, the angle difference between the principal values is seen as 180°. This indicates that the rotation angle θ_p for the stress element is represented as $2\theta_p$ on the Mohr's circle.

Using the Mohr's circle in Figure 10 as a visual aid, some basic characteristics about the nature of stress transformations under plane rotation can be seen. First, it is clear that the maximum and minimum normal stresses occur at points A and B on the Mohr's circle. Since it was noted above that points A and B correspond to principal directions, it is clear that the principal stress values are maximum and minimum values. Also, the maximum shearing stress occurs at point D on the circle. This corresponds to a plane whose normal is oriented 45° between the principal directions. The magnitude of the maximum shearing stress is one half the difference between the largest and smallest principal stress. When the element is oriented in the direction of maximum shear stress, the normal stresses on each of the two faces are equal, and also have a magnitude equal to one half the sum of the largest and smallest principal stress.

Although the Mohr's circle was derived assuming plane stress, it may also be applied to a more general state of stress oriented in the principal directions. This is true because in the principal directions no shear stresses are present. If the element is rotated about a principal axis, then the axis about which it is rotated remains the same and does not affect the transformations of the other stresses. In this way, the restrictions for plane stress transformations are satisfied.

A Mohr's circle can be created for rotations about each of the principal axes. The three circles can be plotted together on the same diagram as shown on Figure 11 [11]. In a general state of stress we have a major, a minor, and a middle principal stress. The major and minor principal stresses are the maximum and minimum possible normal stresses. The middle principal stress is the normal stress corresponding to the remaining principal direction. These are seen as the three points where the three circles cross the normal stress axis. The full range of possible normal stress magnitudes falls within the diameter of the circle created by rotating about the middle principal stress direction.

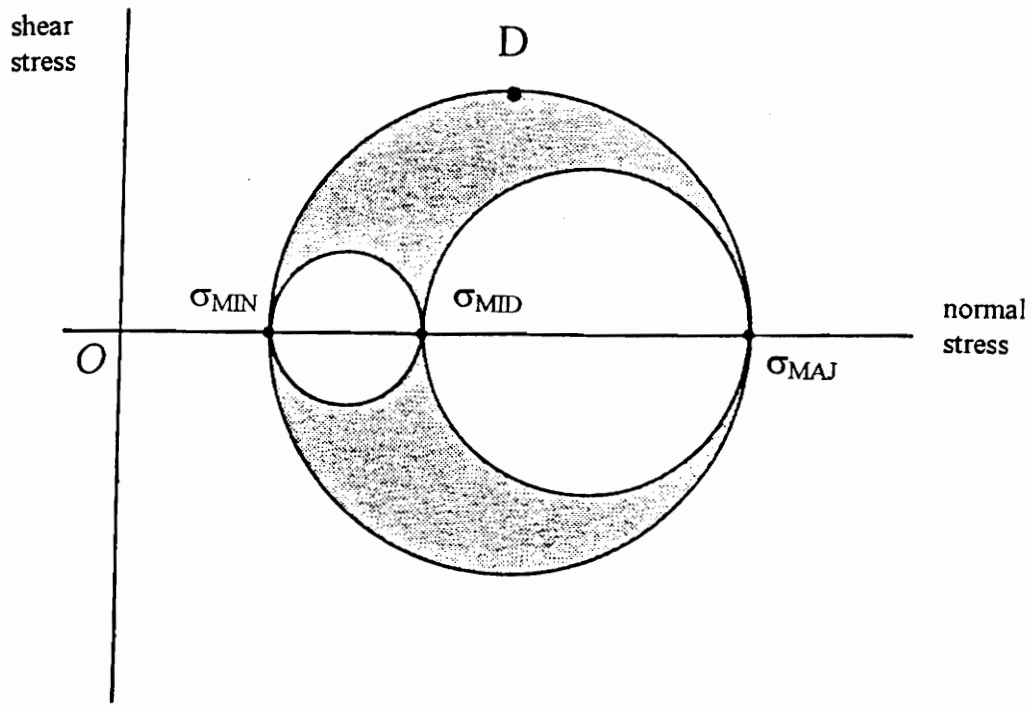

Fig. 11 A Mohr's Circle Under a Generalized State of Stress [11]

2.2.5 Anisotropy of the Stress Tensor

A defining characteristic of any stress tensor is its degree of anisotropy. A stress tensor is considered isotropic if its shearing components are equal to zero in all coordinate system orientations. Additionally, the magnitudes of the normal stress components are equal to one another and do not change with the rotation of the coordinate system. The degree of anisotropy of a stress tensor, put simply, is the level at which it deviates from the isotropic condition. This can be quantified by considering the difference between the maximum and minimum normal stresses. As was noted in Section 2.2.4, these stresses occur when the tensor is oriented in principal directions.

2.3 Tensor Visualization Techniques

As a supplement to the analysis of the effectiveness of various turbulence models in a complex flow geometry, a compact visual representation of the Reynolds stress tensor, a tensor glyph, was developed. Haber [16] defines a glyph as "a geometric icon that represents multi-variate or higher dimensional information at a given position." Just as a vector, a tensor of order 1, is visually represented by an arrow of a particular length oriented in a particular direction, a more elaborate icon was developed to represent the information contained within the second order Reynolds stress tensor.

When dealing with a large set of data, scientists and engineers find it useful to represent the numerical data visually in some form. In this way, patterns in the data become more apparent. Large sets of scalar values can be represented on a contour plot

over the data domain. Vector quantities can be represented as arrows; the lengths and directions of the arrows corresponding, respectively, to the magnitudes and directions of the vectors. The information contained within second or higher order tensors, however, has no simple representation. As a result, it has been common practice to contract the information into more manageable scalar or vector quantities and then plot these values. In the process, information about the tensor is lost. With the increase in computation capacity, it is now possible to create more elaborate visual representations for larger amounts of data. These representations can also take a form in three spatial dimensions instead of two. This increased capability makes it possible for a more complete representation of the information contained within higher order tensors.

2.3.1 The Quadric Surface

One method for describing second order tensors has existed for some time. It is the quadric surface as presented by Frederick and Chang [10]. Here, the properties of a symmetric second order tensor are manipulated to derive an equation for a surface in three dimensional space. This surface, therefore, can be used to yield visual information about the tensor.

Consider a tensor σ_{ij} defined in a local Cartesian coordinate system y_1,y_2,y_3 at a point P in space. Then, the equation

$$\sigma_{ij}y_iy_j = k^2, \tag{29}$$

defines a surface in three dimensional space. This is the quadric surface. Here, k is an arbitrary constant. Expanding the tensor notation gives:

$$\sigma_{11}y_1^2 + \sigma_{22}y_2^2 + \sigma_{33}y_3^2 + 2\sigma_{12}y_1y_2 + 2\sigma_{13}y_1y_3 + 2\sigma_{23}y_2y_3 = k^2. \quad (30)$$

Clearly, this is an equation of a surface in three dimensional space: the quadric surface.

Using Equation (29) two properties of the quadric surface can be shown [10]:

(I) If Q is a point on the quadric surface, and the line PQ is of length r, then the magnitude of the normal stress acting across a plane normal to PQ is inversely proportional to r^2.

(II) A stress vector, σ_i, acting across the plane normal to PQ is parallel to a vector, $\underline{N}$, normal to the quadric surface at Q.

These properties are illustrated in Figure 12 [10].

Additionally, principal values and directions can be inferred from the quadric surface. The major and minor principal values will correspond to those points on the surface that have the shortest and longest distances to the glyph center, respectively. These points will be oriented in principal directions. The middle principal direction will

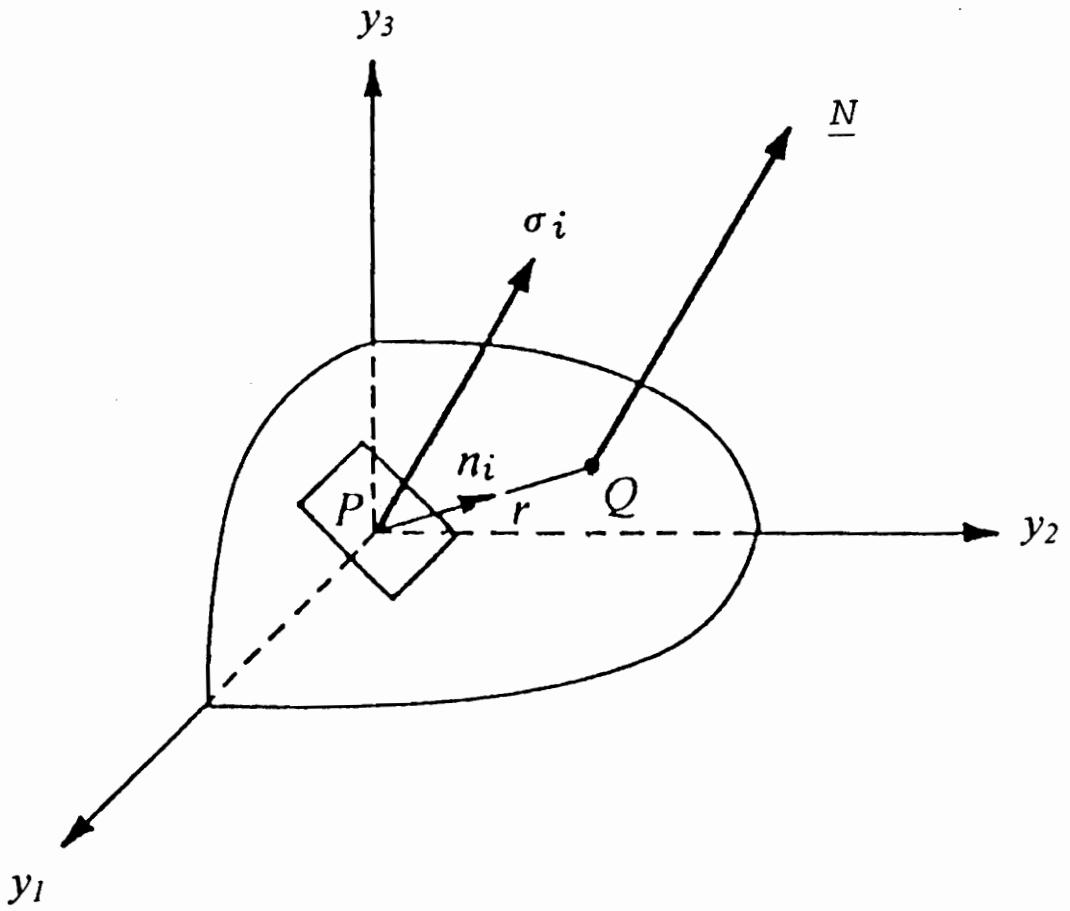

Fig. 12 A Quadric Surface [10]

be orthogonal to the other two principal directions; the point on the quadric surface in this direction will be the middle principal value.

The quadric surface can therefore give information about the magnitudes of the normal stresses in all coordinate directions, the orientations of the total stresses in all coordinate directions, and the magnitudes and directions of the principal stresses in a compact visual representation.

2.3.2 Haber's Cylinders

A more simplified visual representation was presented by Haber [16]. Essentially, Haber's glyphs are cylindrical shafts surrounded at the mid-length by an elliptical disk. This is shown in Figure 13 [16]. The length and orientation of the shaft indicates the magnitude and orientation of the major principal stress, while the magnitudes of the elliptical disk's major and minor axes represent the magnitudes of the middle and minor principal stresses. The relative sizes of the shaft length and disk axes can be scaled for a clearer visual representation when the major principal stress dominates the others. Additionally, the shaft and disk can be color coded to indicate compression or tension in the principal directions.

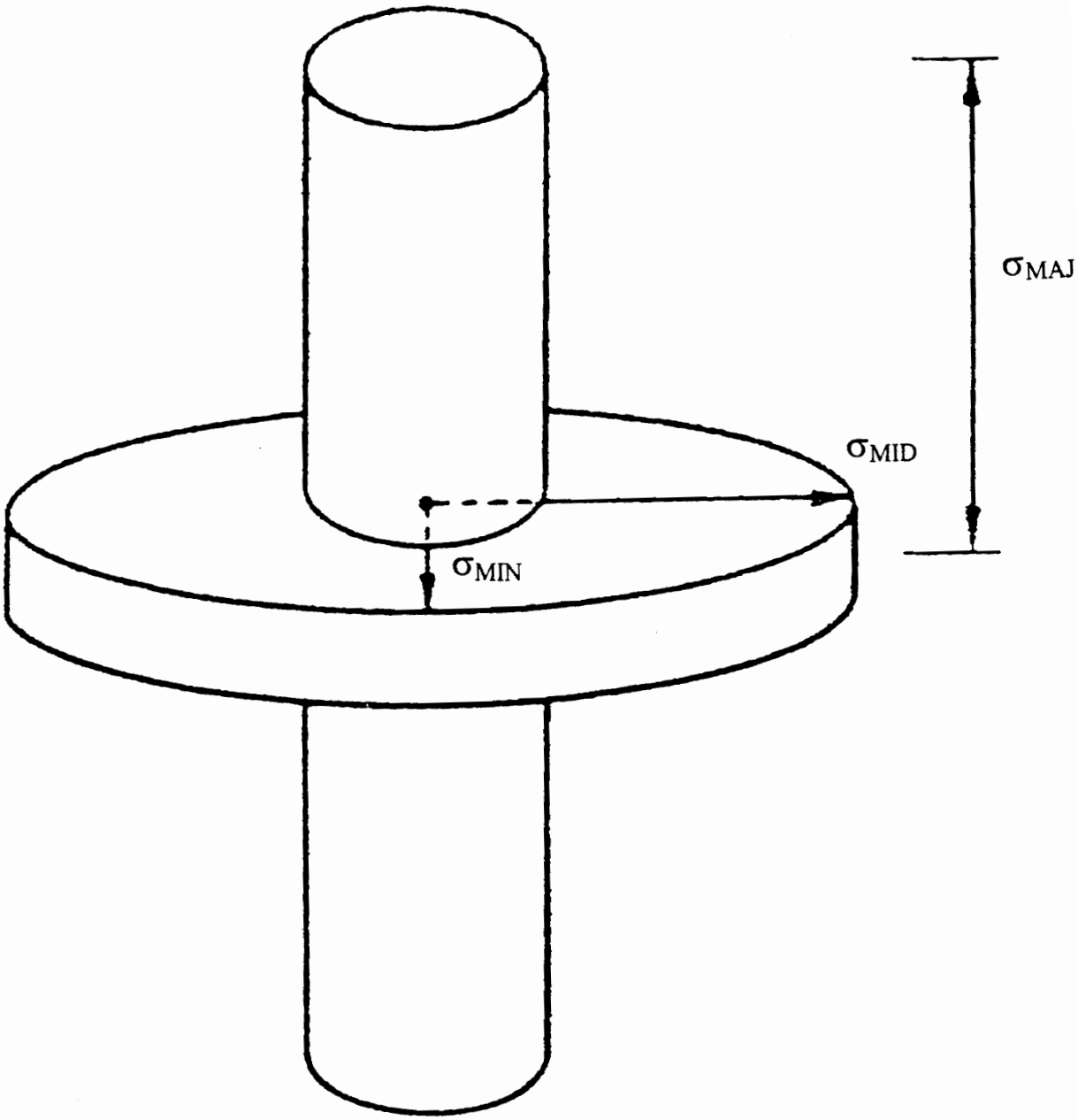

Fig. 13 A Haber Cylinder [16]

3.0 Plan of Investigation

The primary objective of this research is to develop a suitable tensor glyph for the purpose of representing the Reynolds stress tensor and evaluating the performance of turbulence models. With regard to this effort, two flow geometries are considered: fully developed pipe flow and flow in a tip leakage turbine cascade. For both of these, experimental data for the Reynolds stress components and the mean velocity gradients are available. These are used to make three sets of glyphs for each flow. First, the Reynolds stress data is utilized to make glyphs representing the measured Reynolds stress tensor. Also, glyphs are created that correspond to the Boussinesq approximation and the ARSM formulations of the Reynolds stress tensor. To make these glyphs, measurements for the mean velocity gradients, turbulence kinetic energy, and rate of turbulence production are used to determine all the variables in the model expressions. In doing this, the resulting Reynolds stress predictions from these two models are made as accurate as their formulations will allow. These three sets of glyphs are then compared to determine whether the ARSM offers an improvement over the Boussinesq approximation.

Plots of the individual Reynolds stress components are also created. These are used along with the tensor glyphs in the analysis of the Reynolds stress data. With this, the strengths and weaknesses of both representations can be determined, and an effective way of using the tensor glyph can be developed.

Additionally, two methods for calculating the rate of turbulence dissipation, one connected to the Boussinesq approximation and the other connected to the ARSM, are

derived. These are used to make calculations in both flows. For the pipe flow, these calculations are compared with experimental dissipation estimates to evaluate the constants used in both models.

Finally, the assumptions used to derive the ARSM from the Full Reynolds stress Model are examined in more detail for both flow geometries. This was done to examine the applicability of the ARSM in these two flows.

With the analyses planned here, it is hoped that an improved way of representing the Reynolds stress tensor will be developed, and a more complete understanding of the Boussinesq approximation and the ARSM will be gained.

4.0 Visualization of the Reynolds Stress Tensor

4.1 Analysis of a Data Point In the Tip Leakage Turbine Cascade Flow

For the purpose of constructing glyphs, a data point measured in the tip leakage turbine cascade will be examined. A more complete description of this flow geometry will appear in Chapter 7. At a point in this flow, a Reynolds stress tensor was measured to be:

$$\frac{1000}{U_o^2}\overline{u_i u_j} = \begin{bmatrix} 89.2 & -48.5 & -34.4 \\ -48.5 & 125.1 & 35.1 \\ -34.4 & 35.1 & 78.2 \end{bmatrix} \tag{31}$$

where U_o = 20 m/s. The principal directions and principal values of this stress tensor can be found with the methods described in Section 2.2.3. The components of the three principal direction unit vectors given in flow coordinates are:

$$\begin{aligned} \underline{P}_1 &= (-0.540, 0.727, 0.426) \\ \underline{P}_2 &= (0.744, 0.175, 0.645) \\ \underline{P}_3 &= (0.394, 0.655, -0.635). \end{aligned} \tag{32}$$

The Reynolds stress tensor in the coordinate system defined in these principal directions then becomes:

$$\frac{1000}{U_o^2}\overline{u_{pn}u_{pm}} = \begin{bmatrix} 181.7 & 0 & 0 \\ 0 & 48.0 & 0 \\ 0 & 0 & 62.8 \end{bmatrix}. \tag{33}$$

Here it can be seen that the major principal stress corresponds to $\underline{P}_1$, the minor principal stress to $\underline{P}_2$, and the middle principal stress to $\underline{P}_3$. Also, note that the sum of the diagonal elements in both stress tensors equals 292.5. This value is directly proportional to the turbulence kinetic energy, which is constant in all coordinate system orientations.

4.2 Existing Glyph Types

The stress tensor given in Section 4.1 can be represented visually with a quadric surface and a Haber cylinder. By creating these two glyphs, the strengths and weaknesses of both can be determined, and ideas for an improved visual representation can be developed.

A quadric surface for the stress tensor given above is shown in Figure 14. Here, the flow coordinates are indicated, with the x-coordinate axis pointing out of the page. The principal directions are also shown in this figure; the major principal direction is the blue axis, the minor principal direction is the red axis, and the middle principal direction is the black axis.

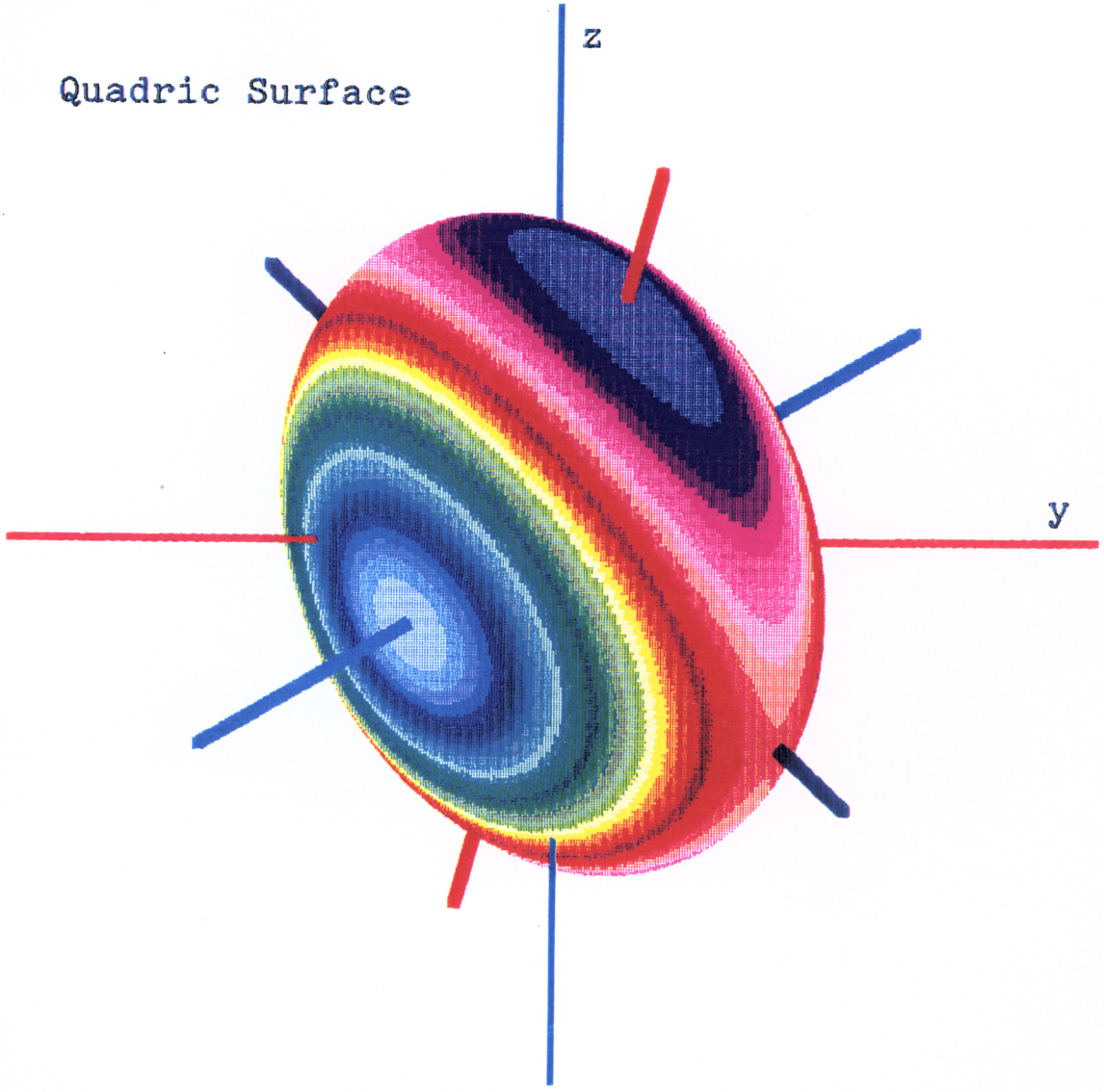

Fig 14 A Quadric Surface for a Reynolds Stress Tensor Measured in a Tip Leakage Turbine Cascade

As discussed in Section 2.3.1, the quadric surface contains information concerning the magnitudes of the normal stresses and the directions of the stress vectors acting on planes oriented in all directions. Looking to Figure 14, however, it can be seen that this information is presented obscurely. First, to unlock the information about the normal stress magnitudes, the length to the quadric surface must be squared and inverted. Obviously, this is a complicated visual process. Also, the information concerning the stress vector orientations requires picturing vectors normal to the quadric surface. Since this cannot be done with any precision, the utility of this information is diminished.

Clearly, the quadric surface conveys a wealth of information, but these problems in interpretation make this glyph a difficult tool. As a result, the quadric surface was not chosen to be used in this work.

In Figure 15, a Haber cylinder for the same data point is shown. This is presented in the same orientation as the quadric surface. This glyph presents the major principal stress and direction with the length and orientation of the cylindrical shaft. The minor and middle principal stresses and directions are indicated by the major and minor axes of the elliptical disk.

While the Haber cylinder has the advantage of being much easier to interpret than the quadric surface, it still has two major problems. First, the amount of information given by the Haber cylinder is significantly reduced. Any information about stresses in coordinate directions other than the principal directions is simply not given. Also, the information about the minor and middle principal directions is not very clear. For stress

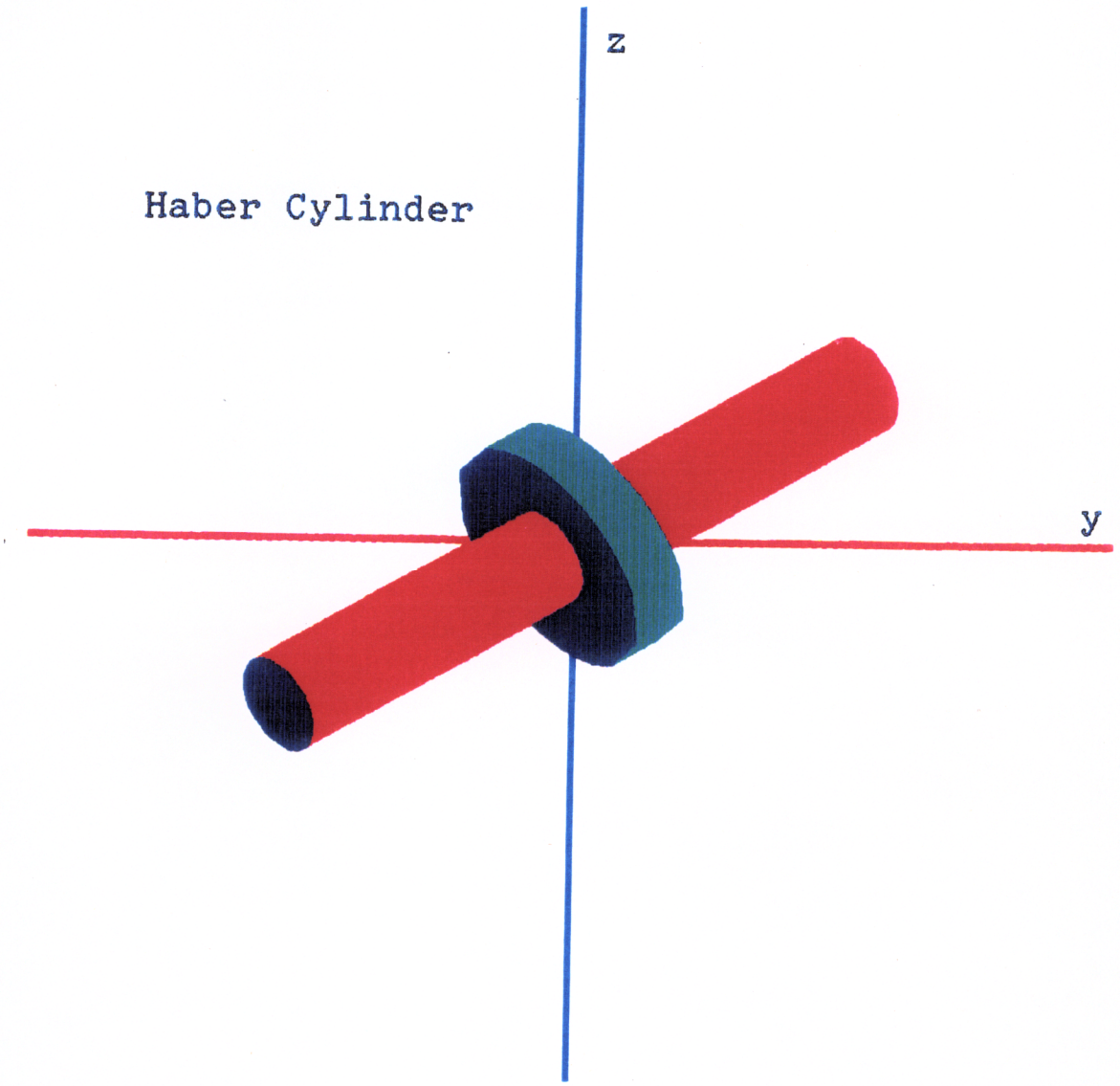

Fig 15 A Haber Cylinder for a Reynolds Stress Tensor Measured in a Tip Leakage Turbine Cascade

tensors with minor and middle principal stresses that have relatively close values, the elliptical disk that represents them becomes circular. In this case, the determination of the ellipse axes is difficult. Because of these two factors, the Haber cylinder was also not considered the ideal glyph form.

4.3 A New Glyph Construction

With the advantages and disadvantages of both the quadric surface and the Haber cylinder in mind, a new glyph type was developed. In creating this glyph, a middle ground in previous developments was sought, combining the clarity of the Haber cylinder with the information content of the quadric surface.

4.3.1 Description

The new glyph was made for the stress tensor given in Section 4.1 and is shown in Figure 16. This glyph indicates the magnitudes of the normal stresses in all coordinate directions and emphasizes the orientation of the principal directions. Each glyph is constructed so that the distance from the glyph center to its surface is directly proportional to the normal stress acting on a plane normal to the line joining the two points. The variations in the magnitudes of the normal stresses with direction are reinforced by a color coding. Ranges of normal stress magnitudes were created according to 1/40th of the difference between the major and minor principal stress values. Each range was then assigned a color, so that normal stresses falling within the same range of

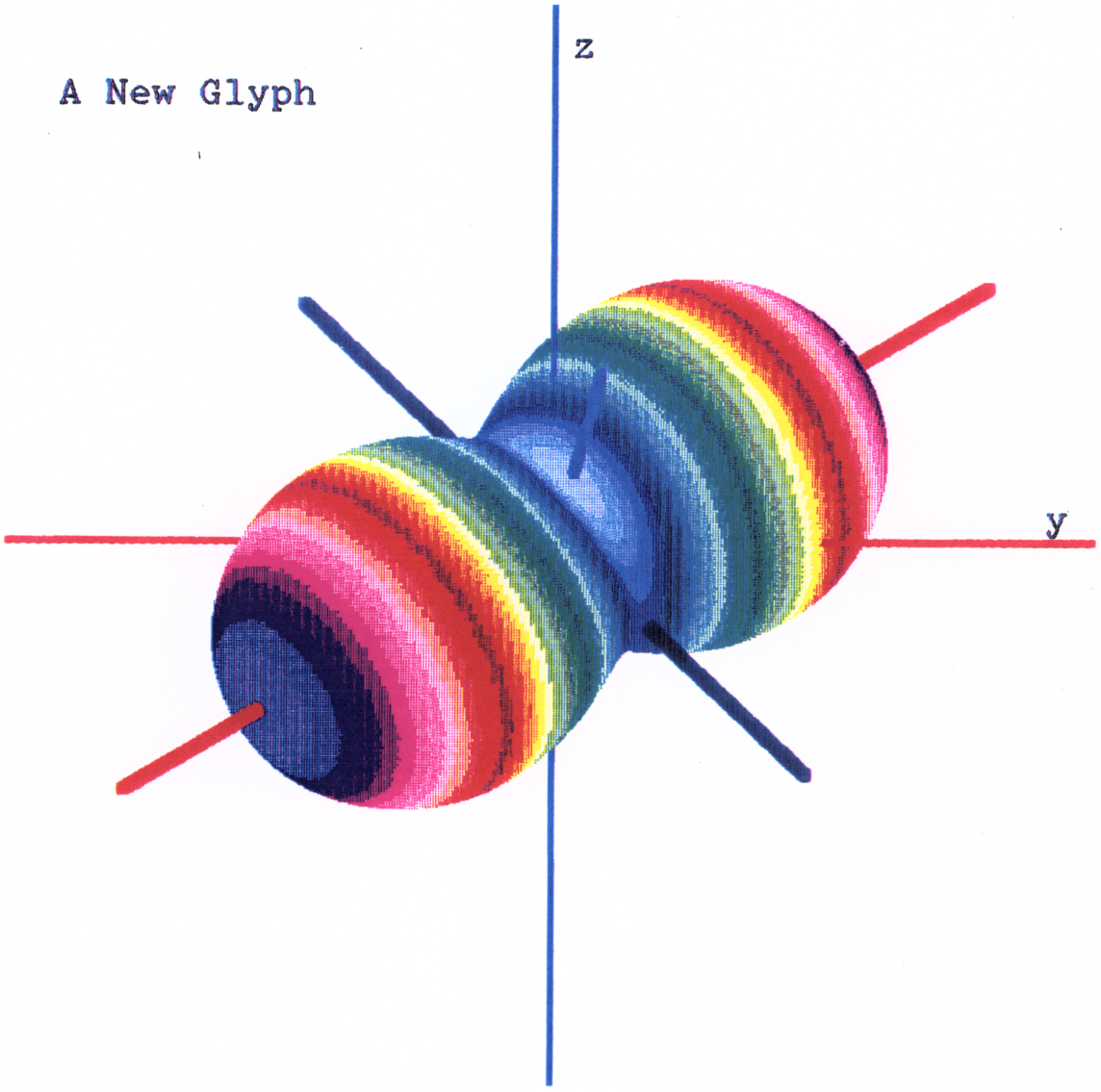

Fig 16 A New Glyph Construction for a Reynolds Stress Tensor Measured in a Tip Leakage Turbine Cascade

values share a common color. The principal directions are indicated by axes protruding from the glyph. These axes are also color coded: red indicates the major principal direction, blue indicates the minor principal direction, and black is the middle principal direction. A detailed description of the glyph construction is given in Appendix C.

4.3.2 Representation of Limiting Physical Cases

In order to effectively interpret the physics behind glyph appearances, it is helpful to first note the glyph shapes with regard to certain limiting physical cases. The limiting cases to be considered involve relative differences in the magnitudes of the principal stresses.

Consider first, however, the case in which no principal stresses exist. This occurs when the normal stresses are of equal magnitude in all coordinate directions. This is the case of isotropic stress. Clearly, this will translate into a spherical shaped glyph as shown in Figure 17.a.

Next, consider the case when two principal stresses are of equal magnitude and the third principal stress is of lesser magnitude. This will result in a donut-like shape and is shown in Figure 17.b. The orientation of the "donut-hole" in this representation is the direction of the smallest possible normal stress. The severity of the hole indentation is an indication of the relative difference between the two principal stress values.

Now suppose two principal stresses are of equal magnitude and the third has a larger value. For relatively small differences between the two values, this will appear as

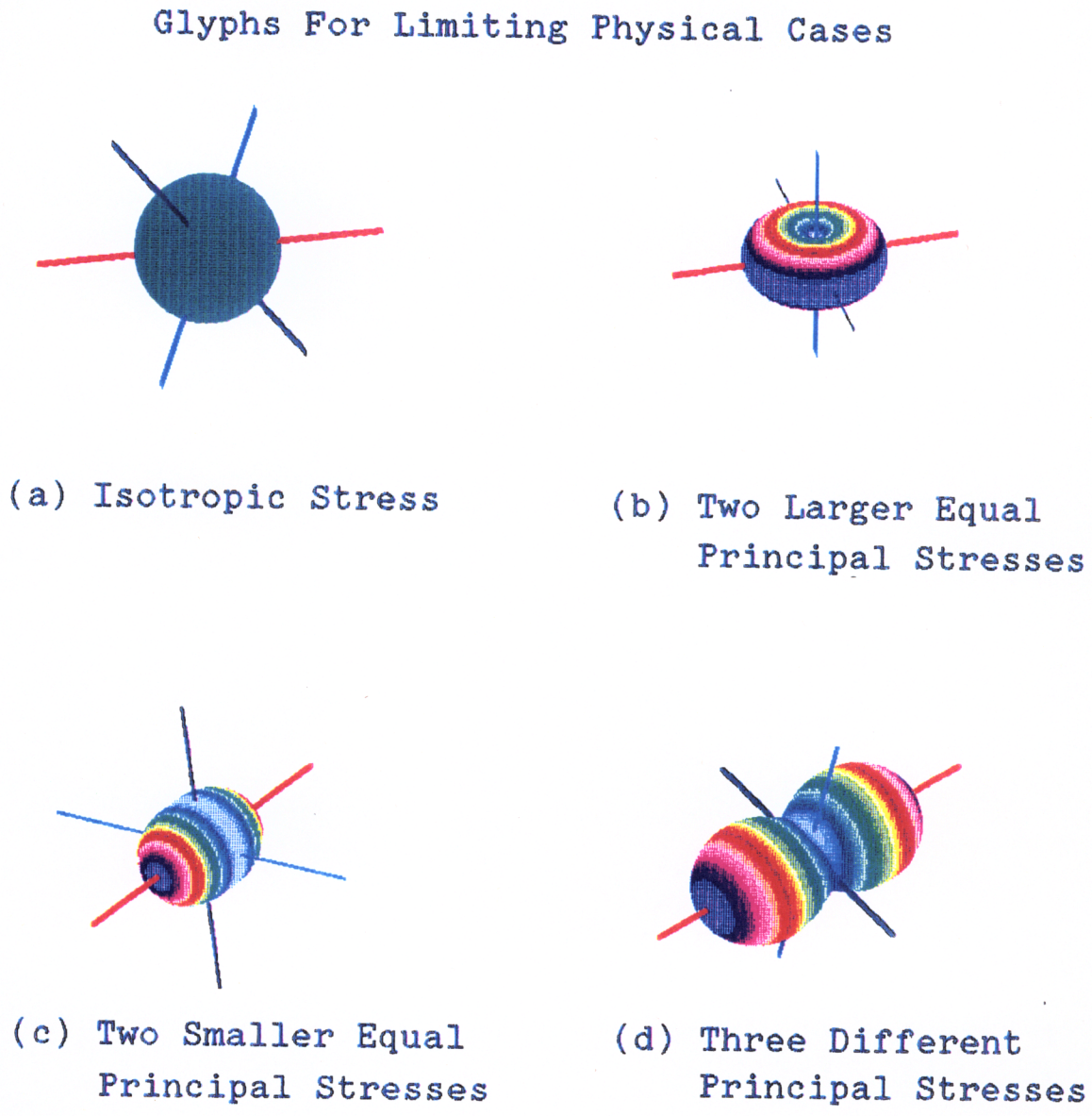

Fig 17 Glyph Appearances for Limiting Physical Cases

an egg-shaped glyph, as shown in Figure 17.c. The longer region in the egg corresponds to the larger principal stress value. The more oblong the glyph appears, the greater the difference between the two stress values. As the difference increases, the glyph will appear more peanut shaped, as shown in Figure 17.d. Here, the middle and minor stresses are not exactly the same, but are relatively close in value compared to the major principal stress. This glyph is typical of the stress states found in this thesis.

By understanding these appearances, it becomes easier to interpret the glyphs corresponding to the intermediate cases (e.g. a glyph that appears something like a cross between a donut and an indented peanut has two principal stress values that are close to one another and much larger than the third stress value).

4.3.3 Advantages

This new glyph was designed so that the magnitudes of the normal stresses, the orientation of principal directions, and the degree of anisotropy could be easily interpreted. The normal stress magnitudes and the principal direction orientations are directly shown by the glyph size and protruding axes orientation. In addition, the degree of anisotropy is also indicated by the shape of the glyph, the more sphere-like the glyph is shaped, the more isotropic the state of stress. With the simple representation of this information, this new glyph construction is easier to interpret than the quadric surface. At the same time, it conveys more information than the Haber cylinder. For these reasons,

this glyph was chosen for representing the Reynolds stress tensors considered in this work.

4.4 Shearing Stresses In Principal Planes

A Mohr's circle can easily be used in conjunction with this tensor glyph to depict the transformation of the Reynolds stress tensor with the rotation of the coordinate system about one of the principal directions. In this way, shear stresses in the planes formed by two principal direction vectors can be shown. A Mohr's circle corresponding to the stress tensor given in Section 4.1 is shown in Figure 18. The three principal stress values are indicated along the normal stress axis. As stated in Section 2.2.4, all possible states of stress are contained within the circle formed by the rotation about the middle principal direction. On Figure 18, this is the largest circle. The maximum possible shearing stress, therefore, is point A on the circle. The coordinate system corresponding to this point is defined by the vectors $\underline{S}_1$, $\underline{S}_2$, $\underline{S}_3$. For the data considered, these are aligned so:

$$\underline{S}_1 = \frac{\underline{P}_1 + \underline{P}_2}{\sqrt{2}} = (0.144, 0.637, 0.757)$$

$$\underline{S}_2 = \frac{\underline{P}_1 - \underline{P}_2}{\sqrt{2}} = (0.908, -0.390, 0.155) \qquad (33)$$

$$\underline{S}_3 = \underline{P}_3 = (0.394, 0.665, -0.635).$$

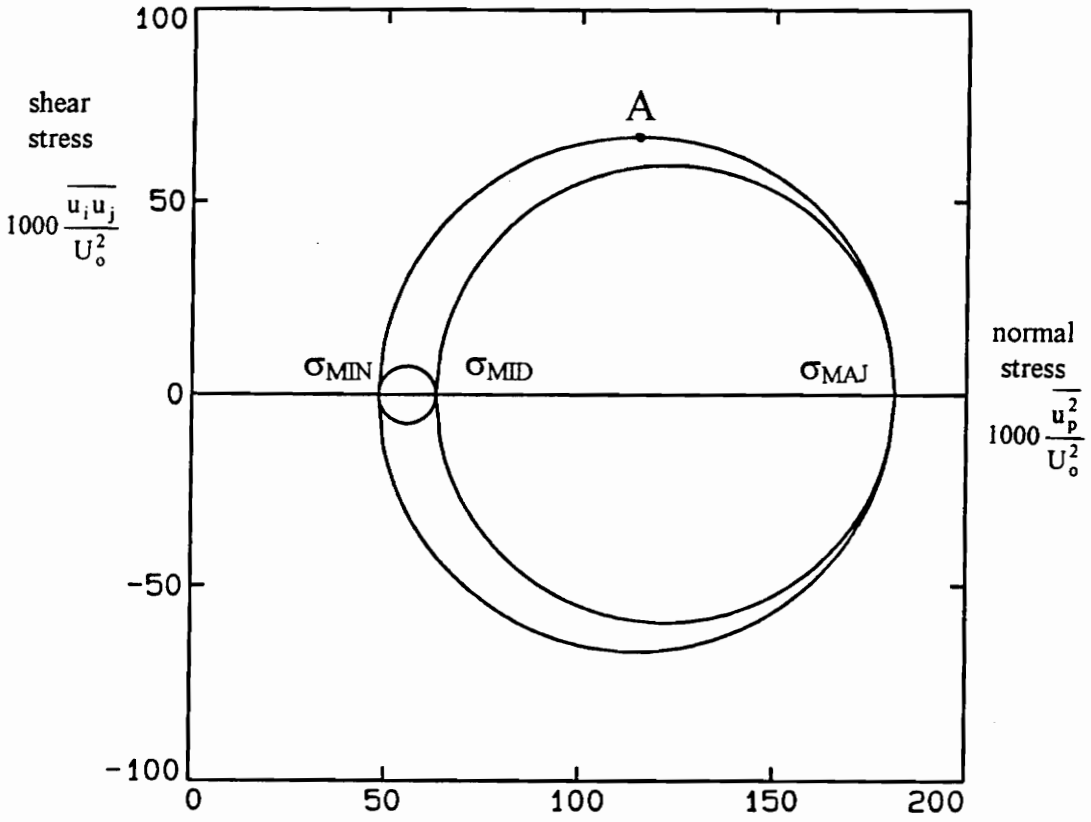

Fig. 18 A Mohr's Circle for a Measured Point in a Tip Leakage Turbine Cascade

The resulting stress tensor is

$$\frac{1000}{U_o^2}\overline{u_{si}u_{sj}} = \begin{bmatrix} 114.8 & -66.9 & 0 \\ -66.9 & 114.8 & 0 \\ 0 & 0 & 62.8 \end{bmatrix}. \qquad (34)$$

Note that two of the normal stresses equal one another as indicated by the Mohr's circle.

5.0 Methods of Analyzing the Boussinesq Approximation and the ARSM

To calculate Reynolds stress components as predicted by the Boussinesq approximation and the ARSM, other flow quantities must first be determined. Recall from Section 2.1.1 that the Boussinesq approximation is:

$$-\overline{u_i u_j} = \nu_t \left[\frac{\partial U_i}{\partial x_j} + \frac{\partial U_j}{\partial x_i} \right] - \frac{2}{3} k \delta_{ij} . \tag{36}$$

Here, it can be seen that values for the mean velocity gradients, $\partial U_i / \partial x_j$, the turbulence kinetic energy, k, and the turbulent viscosity, ν_t, must be supplied in order to evaluate the Reynolds stress components.

Likewise, recall that the ARSM is:

$$\overline{u_i u_j} = k \left[\frac{2}{3} \delta_{ij} + \frac{(1-\gamma)\left(P_{ij} - \frac{2}{3} P \delta_{ij} \right)}{(C_1 - 1)\varepsilon + P} \right] , \tag{37}$$

where P_{ij} and P represent the rate of Reynolds stress component production and the rate of turbulence kinetic energy production, respectively. The turbulence kinetic energy and

mean velocity gradients must again be determined, along with the rate of turbulence dissipation, ε, before Reynolds stresses can be calculated from the ARSM.

Normally in CFD codes, the Reynolds stresses are solved as part of a coupled set of flow variable equations. The other flow variables appearing in the Boussinesq approximation and the ARSM are found simultaneously with the Reynolds stresses. It is the intent of this work, however, to focus exclusively on how well the Reynolds stress tensor is represented within the flow solvers. For this reason, experimental data was used to determine all other quantities appearing in the Reynolds stress expressions. In doing this, errors in the predictions of the other flow variables are eliminated and the accuracy of the Reynolds stress models can be evaluated to within the accuracy of experimental measurements.

The determination of the velocity gradients and the turbulence kinetic energy is straightforward. The flows considered in this work have detailed measurements of Reynolds stresses and mean velocity components. The turbulence kinetic energy, therefore, is simply calculated from measured normal Reynolds stress components. Likewise, the mean velocity gradients are approximated using the mean velocities, measured throughout the flowfield.

The turbulent viscosity and rate of dissipation were determined by deriving modeled expressions for the rate of turbulence production, and setting these expressions equal to the production calculated from the experimental measurements. From the Boussinesq approximation, the rate of turbulence production is:

$$P = -\overline{u_i u_j}\frac{\partial U_i}{\partial x_j} = \nu_t\left[\frac{\partial U_i}{\partial x_j} + \frac{\partial U_j}{\partial x_i}\right]\frac{\partial U_i}{\partial x_j} - \frac{2}{3}k\delta_{ij}\frac{\partial U_i}{\partial x_j}, \tag{38}$$

which, for incompressible flow reduces to:

$$P = -\overline{u_i u_j}\frac{\partial U_i}{\partial x_j} = \nu_t\left[\frac{\partial U_i}{\partial x_j} + \frac{\partial U_j}{\partial x_i}\right]\frac{\partial U_i}{\partial x_j}. \tag{39}$$

This can be rearranged to give

$$\nu_t = \frac{P}{\left[\frac{\partial U_i}{\partial x_j} + \frac{\partial U_j}{\partial x_i}\right]\frac{\partial U_i}{\partial x_j}}, \tag{40}$$

providing an equation for the evaluation of ν_t. Now, ν_t can be calculated using the measured mean velocity gradients and the measured rate of turbulence production.

An expression for the rate of turbulence dissipation was derived from the ARSM in a similar fashion. For incompressible flows, the ARSM gives production as:

$$P = -\overline{u_i u_j}\frac{\partial U_i}{\partial x_j} = -\frac{k(1-\gamma)P_{ij}\dfrac{\partial U_i}{\partial x_j}}{\varepsilon(C_1 - 1) + P} \tag{41}$$

This can be rearranged to provide an expression for the rate of turbulence dissipation:

$$\varepsilon = \frac{-k(1-\gamma)P_{ij}\dfrac{\partial U_i}{\partial x_j}}{P(C_1 - 1)} - \frac{P}{C_1 - 1}, \tag{42}$$

where, in expanded form:

$$P_{ij}\frac{\partial U_i}{\partial x_j} = P_{11}\frac{\partial U_1}{\partial x_1} + P_{22}\frac{\partial U_2}{\partial x_2} + P_{33}\frac{\partial U_3}{\partial x_3} + P_{12}\left(\frac{\partial U_1}{\partial x_2} + \frac{\partial U_2}{\partial x_1}\right) + P_{13}\left(\frac{\partial U_1}{\partial x_3} + \frac{\partial U_3}{\partial x_1}\right)$$

$$+P_{23}\left(\frac{\partial U_2}{\partial x_3} + \frac{\partial U_3}{\partial x_2}\right) \tag{43}$$

Equation (42) is coupled to the set of six ARSM Reynolds stress equations given in Equation (37) through the term $P_{ij}\,\partial U_i/\partial x_j$. This coupling occurs because the Reynolds stresses appearing in P_{ij} (see Equation (11)) are ARSM values. Equations (37) and (42) must therefore be solved simultaneously.

The simultaneous solution of Equations (37) and (42) was done using an iteration procedure. First, initial estimations were made for the Reynolds stress components to

calculate a value for ε. For simplicity, the actual measurements of the Reynolds stress components were used as initial estimates. The initial value for ε can then be written as;

$$\varepsilon^{(1)} = \frac{-k(1-\gamma)\left(P_{ij}\dfrac{\partial U_i}{\partial x_j}\right)^{(1)}}{P(C_1-1)} - \frac{P}{C_1-1} \tag{44}$$

Here, ε and $P_{ij}\,\partial U_i/\partial x_j$ have superscripts because these values change with successive iterations. This value for the dissipation, along with the estimations for the six Reynolds stresses was then used to calculate new $\overline{u_i u_j}$ values according to equation (37). That is:

$$\left(\overline{u_i u_j}\right)^{(2)} = k\left[\frac{2}{3}\delta_{ij} + \frac{(1-\gamma)\left(P_{ij}^{(1)} - \dfrac{2}{3}P\delta_{ij}\right)}{(C_1-1)\varepsilon^{(1)} + P}\right]. \tag{45}$$

These new $\overline{u_i u_j}$ values are then used to re-calculate P_{ij} and a value for ε, and the process is continued until the successive values of ε and $\overline{u_i u_j}$ all converge to within ± 0.0001.

After the values for the dissipation and the Reynolds stresses were calculated, two interesting features of this ARSM solution method became apparent.

First, the values for the constants C_1 and γ did not effect the solutions for $\overline{u_i u_j}$, but they did influence the final solution for ε. The reason for this can be seen clearly if Equation (42) is re-written as:

$$-\frac{P}{P_{ij}\frac{\partial U_i}{\partial x_j}} = \frac{k(1-\gamma)}{\varepsilon(C_1 - 1) + P}. \tag{46}$$

The expression on the right hand side of Equation (46) appears in each of the Reynolds stress expressions shown in Equation (37). Equation (37) can therefore be rewritten as:

$$\overline{u_i u_j} = \frac{2}{3}k\delta_{ij} - \frac{P}{P_{km}\frac{\partial U_k}{\partial x_m}}\left(P_{ij} - \frac{2}{3}P\delta_{ij}\right) \tag{47}$$

With this formulation, it can be seen that the Reynolds stresses are actually uncoupled from the dissipation. The value for the dissipation, however, can easily be calculated from Equation (42). Clearly, the solution for ε depends on the values of C_1 and γ. For these constants, the values of C_1=1.5 and γ=0.6, as suggested by Launder, et al. [7], were initially used. For the fully developed pipe flow, more suitable constants were found. This will be discussed in Section 6.4.4.

Another feature of the ARSM solution method appeared when predictions for the tip leakage turbine cascade flow were being calculated. For a few points in this flow, the solutions for $\overline{u_i u_j}$ did not converge to a single value. These points were examined further to determine how the ARSM Reynolds stress solutions combined with the measured velocity gradients to calculate turbulence production. In this ARSM solution method, it was assumed that the rate of turbulence production equaled the production calculated from experimental measurements. It was thought, therefore, that at the points that did not converge to a solution, the production calculated by the ARSM could not give a value equal to the measurements. This theory was checked by solving the ARSM, as given in Equation (37), using the measured values of the turbulence kinetic energy and production, and arbitrarily varying the rate of turbulence dissipation from zero to a large number. The resulting ARSM Reynolds stress components were then used, along with mean velocity gradients, to calculate a rate of turbulence production, P_{ARSM}. The P_{ARSM} values were then plotted against the values for turbulence dissipation and compared to the production calculated from the experimental measurements, P_{DATA}. Such plots are shown in Figure 19. On this figure, a point with a converged ARSM solution and a point in which the ARSM did not converge are both shown. As expected, for the point that did not converge to a solution, there was no value for ε for which $P_{ARSM} = P_{DATA}$.

At the points that did not have a proper solution, the value for P_{DATA} was lowered to a value that could be calculated by the ARSM. To keep the adjustment as small as possible, P_{DATA} was set to the peak value of P_{ARSM}, as seen on Figure 19. The largest

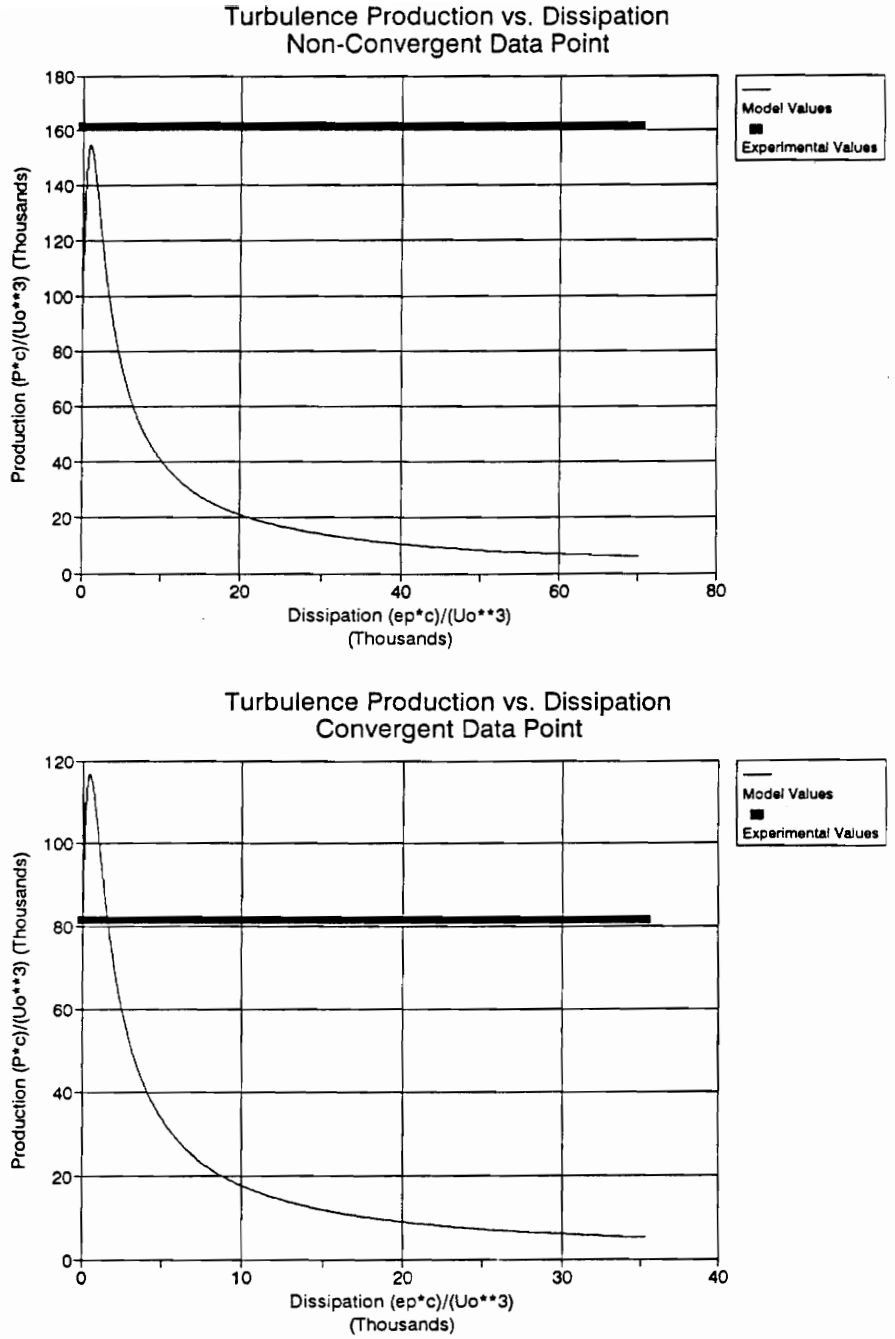

Fig. 19 ARSM Production vs. Dissipation for a Convergent and a Non-Convergent Data Point

required adjustment was a 50% reduction in value. The need for such adjustments could be attributed to the combined uncertainty in the measured values used to calculate P_{DATA}, or it could indicate that Rodi's ARSM is inappropriate for these points.

6.0 Fully Developed Turbulent Pipe Flow

Before attempting to analyze a complex flow geometry such as the turbine cascade, it seemed prudent to start with a better understood flow geometry. To this end, an analysis of fully developed turbulent pipe flow was performed. Because the structure of turbulence in such a flow has been studied carefully in the past [17], the results from a new analytical method such as the tensor glyph can be compared with previous experimental studies. This provides a check on the new method. Additionally, the assumptions of fully developed pipe flow allow considerable simplifications in the analysis. For these reasons, the development of the new model evaluation techniques associated with the use of the tensor glyph can be performed with greater ease and confidence. Afterwards, these techniques can be extended to the analysis of the more complicated turbine tip leakage vortex data.

6.1 Turbulent Pipe Flow - The Equations of Motion

Following Laufer [17], the Reynolds time-averaged momentum equations can be used to show simplifications of the Reynolds stress tensor under the conditions of fully developed pipe flow for an incompressible fluid.

A cylindrical coordinate system will be used with x, r, and ϕ corresponding to the axial, radial, and circumferential flow coordinate directions. Corresponding average flow velocities are denoted by U, V, and W. Fluctuating flow velocities are denoted by u, v,

and w. Time averaged quantities are indicated by an overbar. In cylindrical coordinates, the full time-averaged Reynolds equations are:

$$U\frac{\partial U}{\partial x}+V\frac{\partial U}{\partial r}+\frac{W}{r}\frac{\partial U}{\partial \phi}=-\frac{1}{\rho}\frac{\partial P}{\partial x}-\left(\frac{\partial}{\partial x}\overline{u^2}+\frac{1}{r}\frac{\partial}{\partial r}\overline{ruv}+\frac{1}{r}\frac{\partial}{\partial \phi}\overline{uw}\right)+\nu\nabla^2 U \qquad (48)$$

$$U\frac{\partial V}{\partial x}+V\frac{\partial V}{\partial r}+\frac{W}{r}\frac{\partial V}{\partial \phi}-\frac{W^2}{r}=-\frac{1}{\rho}\frac{\partial P}{\partial r}-\left(\frac{\partial}{\partial x}\overline{uv}+\frac{1}{r}\frac{\partial}{\partial r}\overline{rv^2}+\frac{1}{r}\frac{\partial}{\partial \phi}\overline{vw}-\frac{\overline{w^2}}{r}\right)$$

$$+\nu\left(\nabla^2 V-\frac{V}{r^2}-\frac{2}{r^2}\frac{\partial W}{\partial \phi}\right) \qquad (49)$$

$$U\frac{\partial W}{\partial x}+V\frac{\partial W}{\partial r}+\frac{W}{r}\frac{\partial W}{\partial \phi}+\frac{VW}{r}=-\frac{1}{\rho r}\frac{\partial P}{\partial \phi}-\left(\frac{\partial}{\partial x}\overline{uw}+\frac{\partial}{\partial r}\overline{vw}+\frac{1}{r}\frac{\partial}{\partial \phi}\overline{w^2}-2\frac{\overline{vw}}{r}\right)$$

$$+\nu\left(\nabla^2 W+\frac{2}{r^2}\frac{\partial W}{\partial \phi}-\frac{W}{r^2}\right) \qquad (50)$$

where,

$$\nabla^2=\frac{\partial^2}{\partial x^2}+\frac{\partial^2}{\partial r^2}+\frac{1}{r}\frac{\partial}{\partial r}+\frac{1}{r^2}\frac{\partial^2}{\partial \phi^2}.$$

The conditions for fully developed pipe flow allow for considerable simplification of the Reynolds averaged equations. The fully developed pipe flow conditions are:

(1) $V = 0$ and $W = 0$,

(2) $\frac{\partial}{\partial \phi} = 0$,

(3) the velocity field is independent of x.

The Reynolds averaged momentum equations therefore become:

$$\frac{1}{\rho}\frac{\partial P}{\partial x} = -\frac{1}{r}\frac{d}{dr}\overline{ruv} + \nu\left(\frac{d^2U}{dr^2} + \frac{1}{r}\frac{dU}{dr}\right) \tag{51}$$

$$\frac{1}{\rho}\frac{\partial P}{\partial r} = -\frac{1}{r}\frac{d}{dr}\overline{rv^2} + \frac{\overline{w^2}}{r} \tag{52}$$

$$0 = \frac{d}{dr}\overline{vw} - 2\frac{\overline{vw}}{r}. \tag{53}$$

This last equation is the circumferential momentum equation, and can be integrated over the radius of the pipe. Noting that $\overline{vw}$ is exactly zero at the pipe wall and the pipe centerline, it follows that $\overline{vw}$ must equal zero throughout the flow. If $\overline{vw} = 0$ everywhere, the circumferential momentum equation reduces to $0 = 0$. This means that no net momentum transfer occurs in the circumferential direction. This makes sense for a non-swirling pipe flow. Since the $\overline{uw}$ correlation is another quantity that results from circumferential momentum transfer, it follows that $\overline{uw} = 0$ throughout the flowfield.

6.2 Experimental Measurements

All subsequent turbulence modeling analysis with respect to fully developed pipe flow in this thesis is based upon the experimental work of Laufer [17]. Laufer made measurements of the radial distributions of mean and fluctuating flow velocity components at Reynolds numbers of 50,000 and 500,000. From these velocity measurements, Laufer calculated the four Reynolds stresses. The mean velocity profiles found by Laufer are shown in Figure 20. Here the mean velocity is non-dimensionalized by the centerline velocity U_o. The distributions of the $\overline{uu}$, $\overline{vv}$, $\overline{ww}$, and $\overline{uv}$ Reynolds stresses are shown in Figure 21. All Reynolds stress values are non-dimensionalized with the friction velocity, U_τ^2. The radial position in the plots is non-dimensionalized with the pipe radius, a, and is represented by r', which is equal to r-a. Therefore, a value of r'/a = 1 indicates the pipe centerline and r'/a = 0 is the pipe wall. This convention will be used throughout the rest of this chapter.

Laufer also estimated radial distributions of the rate of turbulence dissipation by measuring five of the nine fluctuating velocity gradient terms. He estimated the remaining four by using the assumption of local isotropy of turbulence at the microscales at which turbulence dissipation occurs. Laufer's results for the Reynolds number of 50,000 is shown later. These results are discussed in more detail in Section 6.4.4.

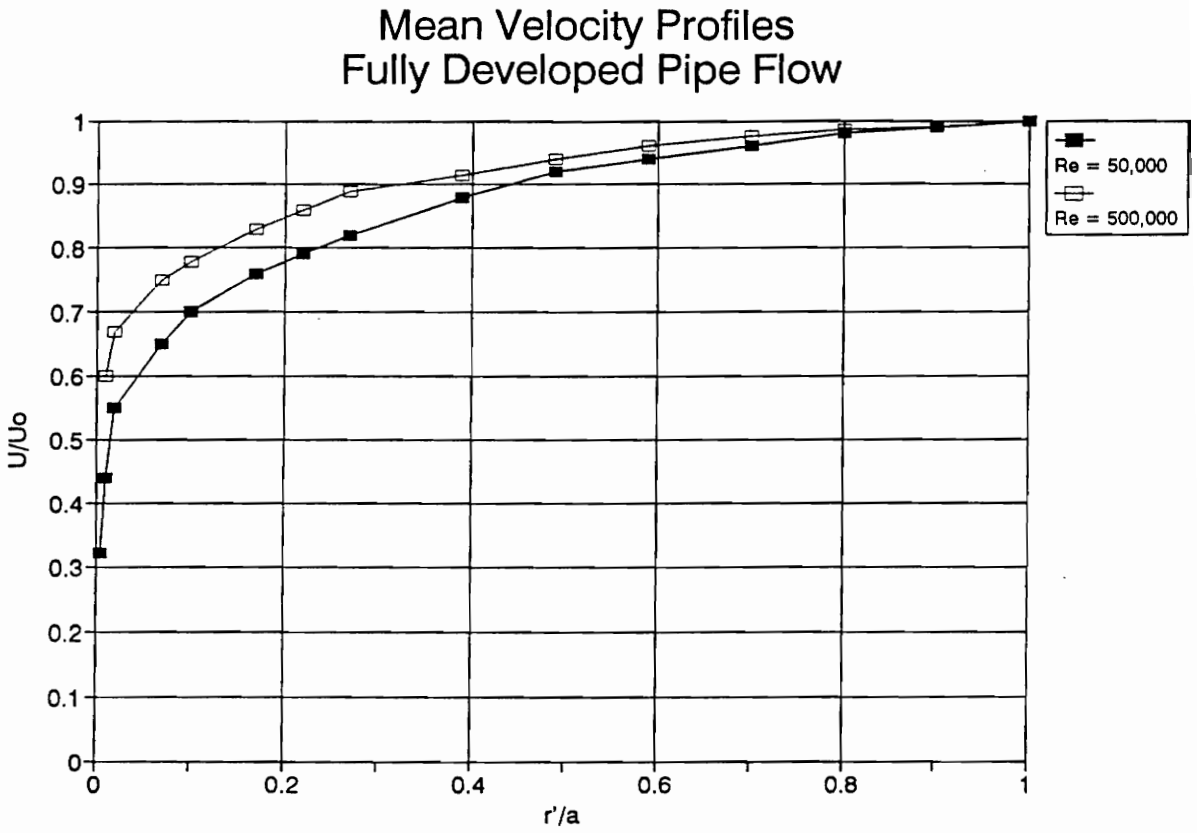

Fig. 20 Mean Velocity Profiles in Fully Developed Pipe Flow [17]

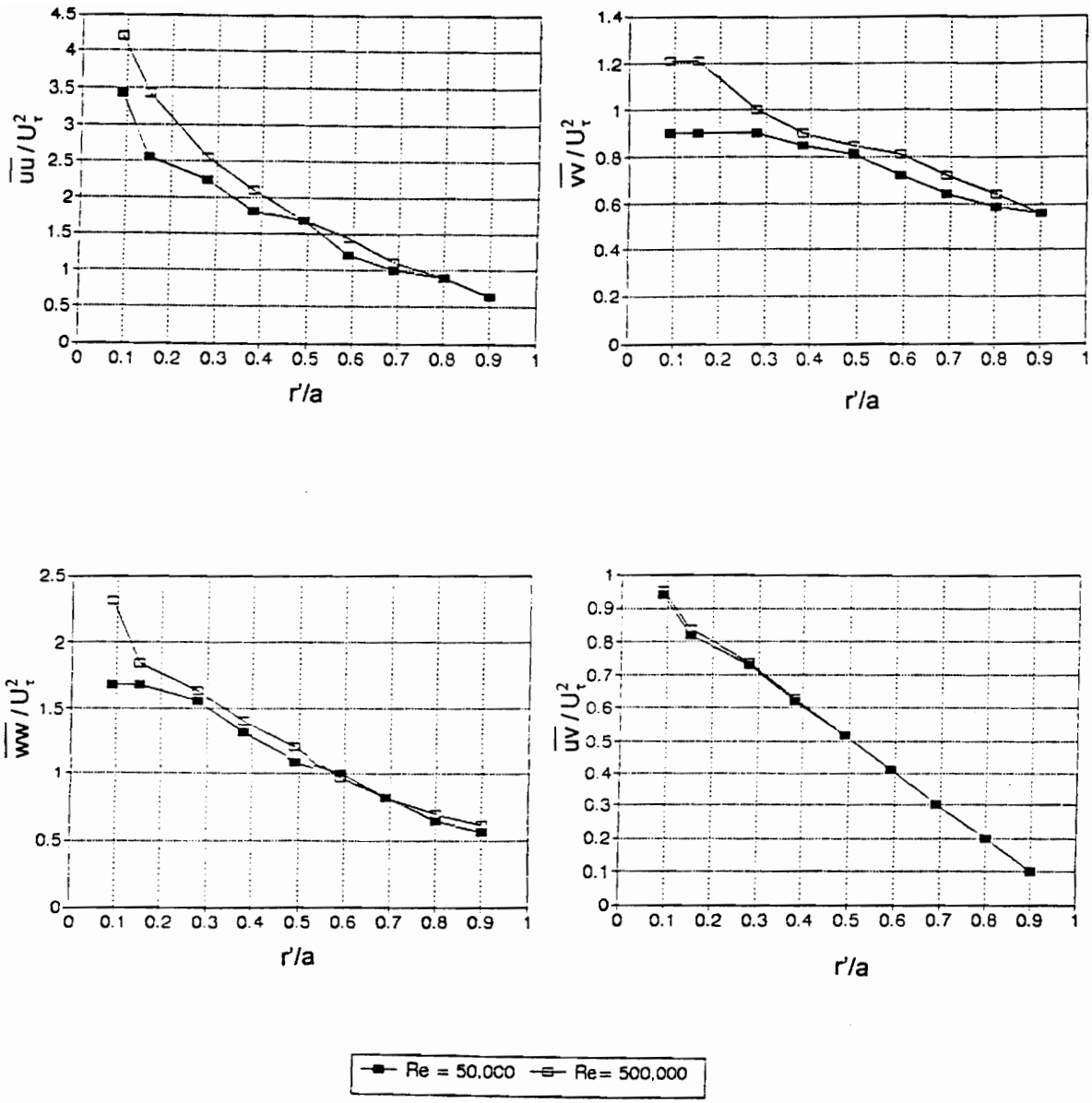

Fig. 21 Reynolds Stress Components in Fully Developed Flow [17]

6.3 Reynolds Stress Predictions for Pipe Flow

The simplifying assumptions of fully developed pipe flow greatly reduce the complexity of the Boussinesq approximation and the ARSM. The pipe flow geometry affects the models primarily through the fact that the only non-zero velocity gradient is dU/dr. This reduces the complicated tensor expansions occurring in the models to simpler algebraic expressions.

Appendix D details the derivation of the Boussinesq approximation and ARSM expressions for the Reynolds stress components. These derivations show that both models predict $\overline{uw} = \overline{vw} = 0$, just as the physics of fully developed pipe flow requires. These shear stress components, therefore, need not be considered. Also note that, for pipe flow, the turbulence production is given as:

$$P = \overline{u_i u_j} \frac{\partial U_i}{\partial x_j} = \overline{uv} \frac{\partial U}{\partial r}. \tag{54}$$

Since we determine the velocity gradients and the turbulence production from the experimental data, it follows that the $\overline{uv}$ stress is also set to the data values. For this reason, the modeled result for this shear stress is also not considered here.

For fully developed pipe flow, the Boussinesq approximation predicts that all normal Reynolds stress components are equal. Normal stresses are equated as:

$$\overline{uu} = \overline{vv} = \overline{ww} = \frac{2}{3}k. \tag{55}$$

The ARSM, on the other hand, predicts:

$$\overline{uu} = \frac{2}{3}k + \frac{4}{3}\frac{\left(\overline{uv}\right)^2}{\overline{vv}} \tag{56.a}$$

$$\overline{vv} = \frac{2}{3}k - \frac{2}{3}\frac{\left(\overline{uv}\right)^2}{\overline{vv}} \tag{56.b}$$

$$\overline{ww} = \frac{2}{3}k - \frac{2}{3}\frac{\left(\overline{uv}\right)^2}{\overline{vv}}. \tag{56.c}$$

Note that the ARSM Reynolds stress expressions form a set of three coupled equations through the appearance of the $\overline{vv}$ stress component in each.

Comparison of the normal stress expressions of the Boussinesq approximation and the ARSM indicates that, for pipes, the two models are related. The predictions of the ARSM can be regarded as the Boussinesq approximation predictions plus some correction factor. While the Boussinesq approximation predicts equal values for all the normal stress components, the correction factors allow the ARSM to predict a distinct value for the axial normal stress. However, the ARSM still gives equal values for the radial and circumferential normal stresses. For comparison, the experimental

measurements given in Figure 21 show distinct values for all three normal stress components.

6.4 Results and Discussion

6.4.1 Reynolds Stress Plots

Figure 22 shows radial distributions of the three normal Reynolds stress components in fully developed pipe flow at a Reynolds number of 50,000. Both the experimental data and the two model predictions are shown. The ARSM shows a clear improvement over the Boussinesq approximation in predicting the $\overline{uu}$ and $\overline{vv}$ stress component. However, the Boussinesq approximation matches the measured $\overline{ww}$ stress component more closely. Compared to the data, the models tend to predict lower $\overline{uu}$ stresses and higher $\overline{vv}$ stresses. Also, the Boussinesq approximation shows slightly higher values for the $\overline{ww}$ stress while the ARSM shows slightly lower $\overline{ww}$ stress values. Both models generally predict the $\overline{uu}$ and $\overline{vv}$ stress values better near the pipe centerline.

Figure 23 shows the three normal Reynolds stress components for pipe flow at a Reynolds number of 500,000. As would be expected, both the measured and modeled stress values are higher than the stresses at Re = 50,000. Besides this, the modeled stresses compare with the data in much the same way for both Reynolds numbers.

These results indicate that the ARSM offers improvements over the Boussinesq approximation in modeling the $\overline{uu}$ and $\overline{vv}$ stresses while providing no significant

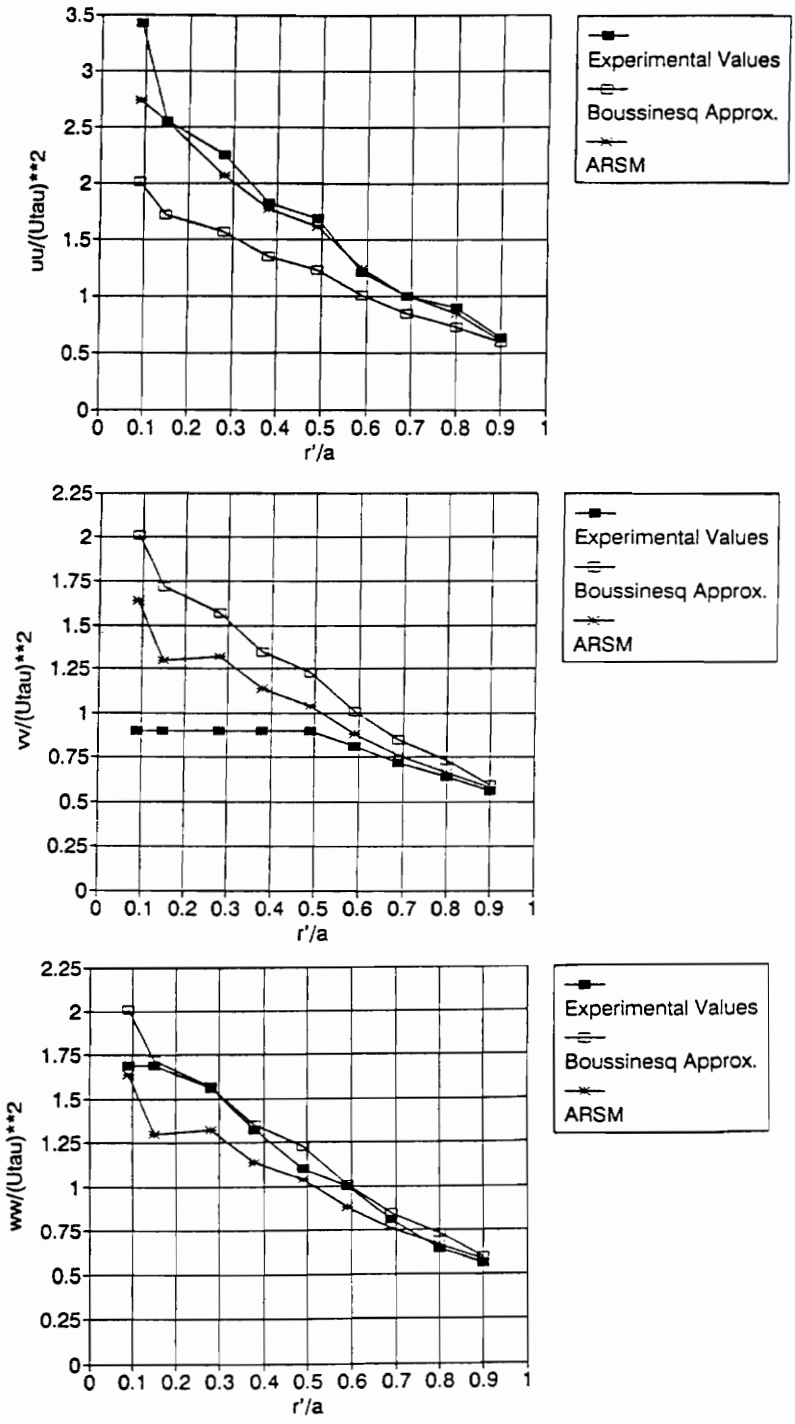

Fig. 22 Measured and Modeled Reynolds Stress Components in Fully Developed Pipe Flow, Re = 50,000

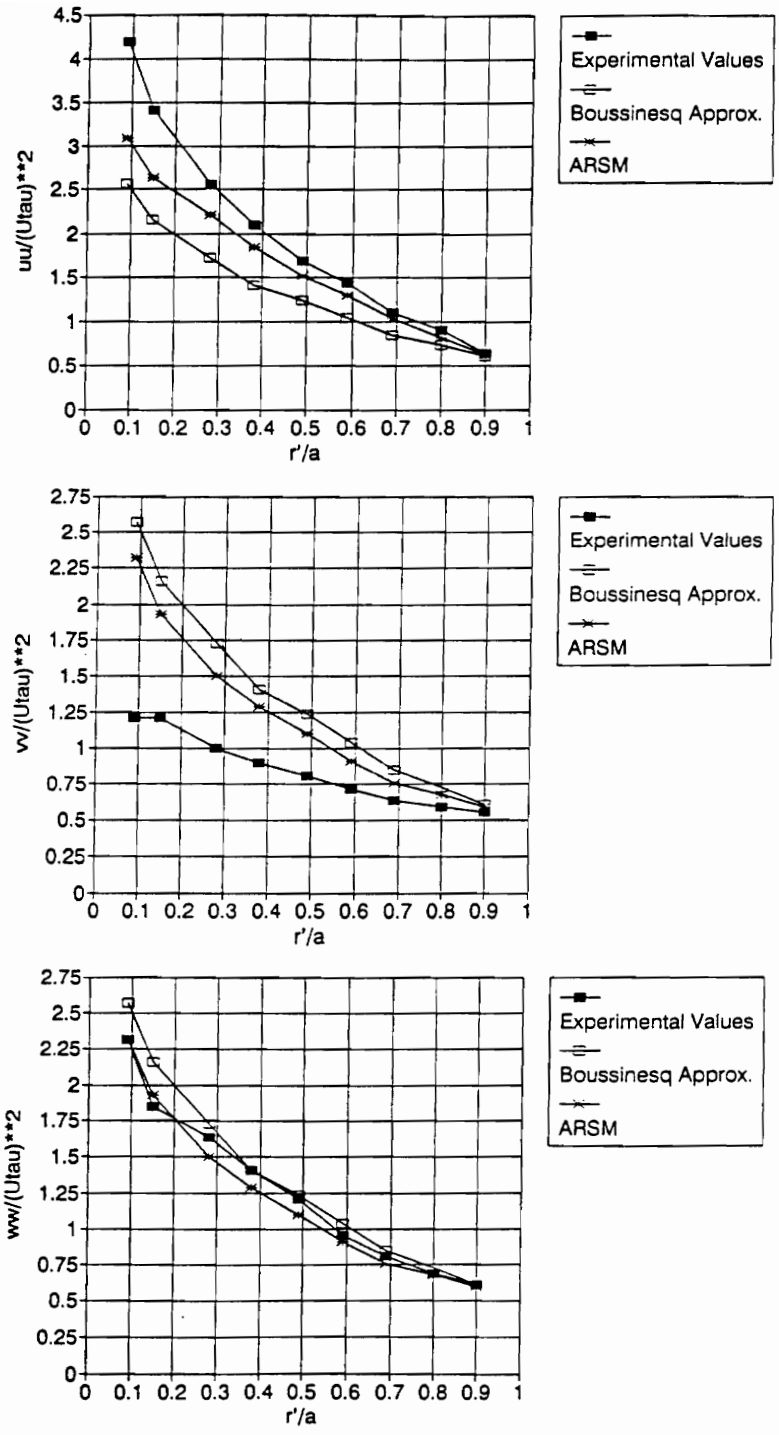

Fig. 23 Measured and Modeled Reynolds Stress Components in Fully Developed Pipe Flow, Re = 500,000

improvement in predicting the $\overline{ww}$ stress. Recalling that the Boussinesq approximation predicts normal stress components of 2k/3, and the ARSM predicts normal stress components of 2k/3 plus some correction factor, these stress plots would suggest that the ARSM correction factor for the $\overline{ww}$ stress is inaccurate in this flow geometry.

6.4.2 Tensor Glyph Pictures

While Figures 22 and 23 give a clear comparison of the individual Reynolds stress components, a view of how these components combine to form the entire tensor is not shown. Characteristics such as the tensor's degree of anisotropy and orientation of principal directions are simply not given with plots of the tensor components. Therefore, if these plots are the sole source of information used in evaluating the tensor, such evaluations are based upon incomplete information. To alleviate this problem, the tensor glyph was created.

Tensor glyph pictures based upon the experimental data and the two model predictions were made for both Reynolds numbers. The radial distributions of glyphs for Re = 50,000 are shown in Figures 24-26. Analogous pictures for Re = 500,000 are shown in Figures 27-29. Note that the glyphs for the lower Reynolds number were scaled in size by a factor of 1.5. This was done for clearer presentation. In these figures, the axial direction is shown horizontally, the radial direction is shown vertically, and the circumferential direction is coming out of the page. Glyphs of the near-wall point for Re = 50,000 were enlarged and are shown in Figures 30 and 31.

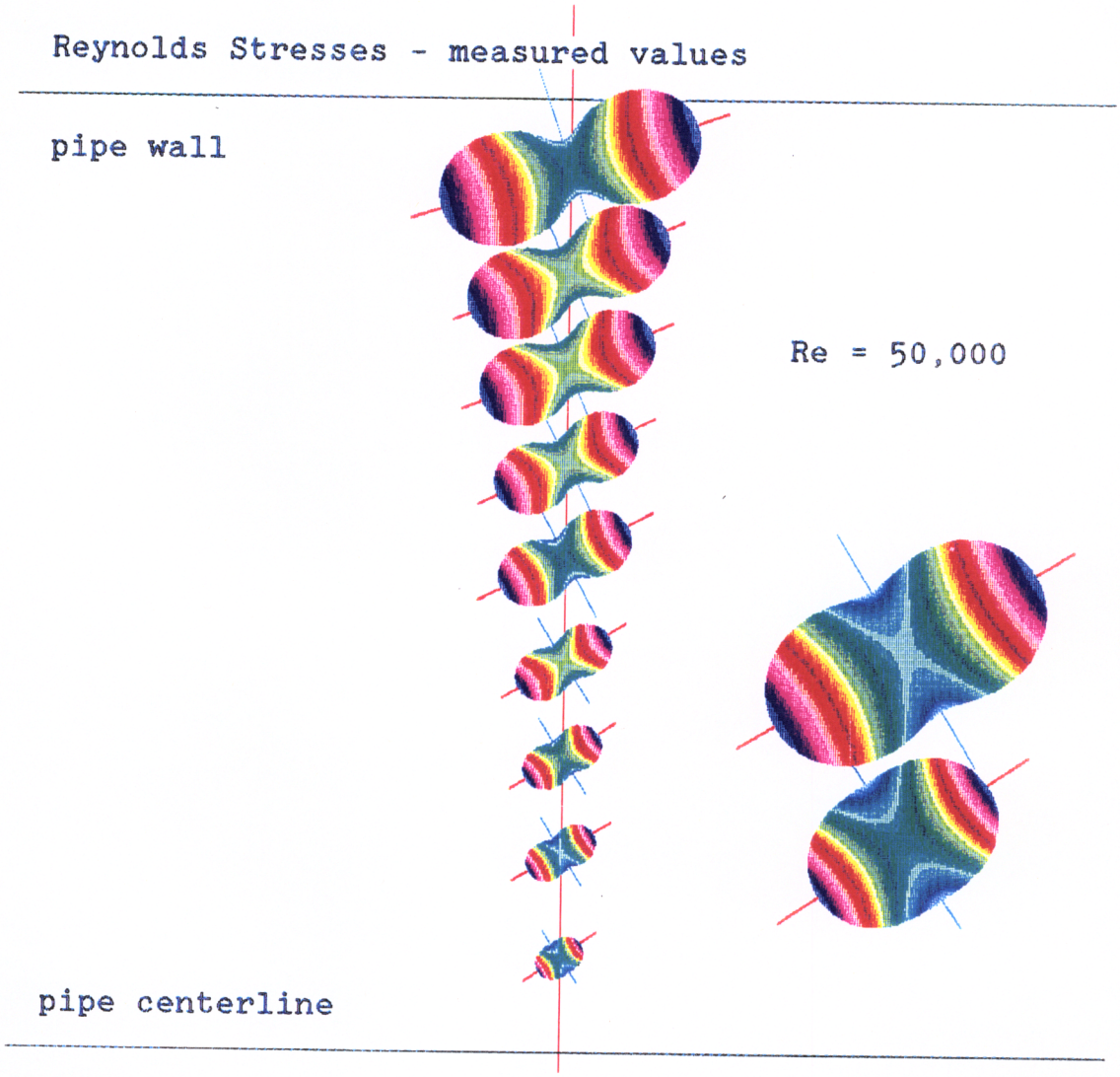

Fig 24 Glyphs for Measured Reynolds Stress Tensors in Fully Developed Pipe Flow; Re = 50,000

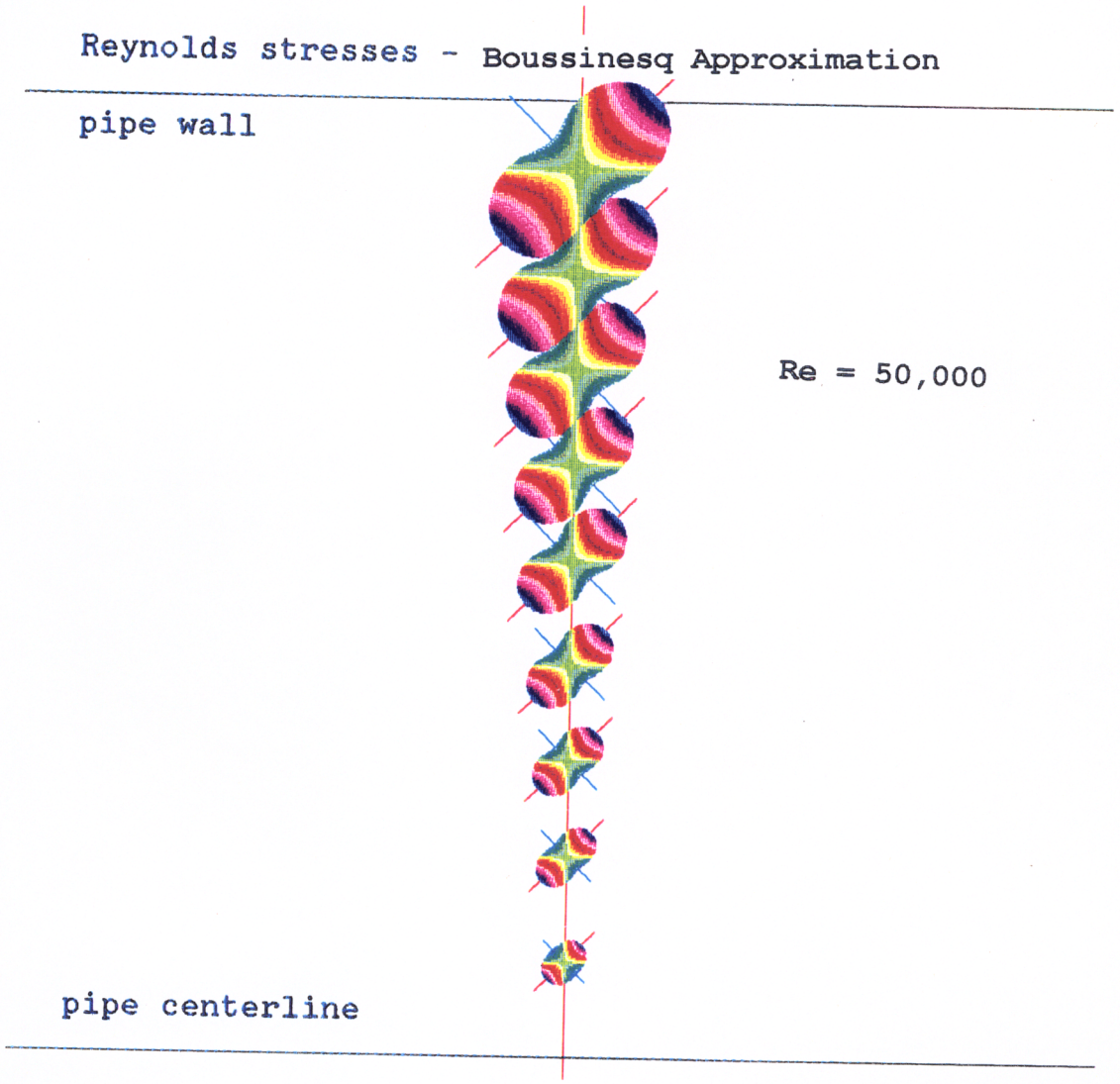

Fig 25 Glyphs for the Boussinesq Approximation Predictions in Fully Developed Pipe Flow; Re = 50,000

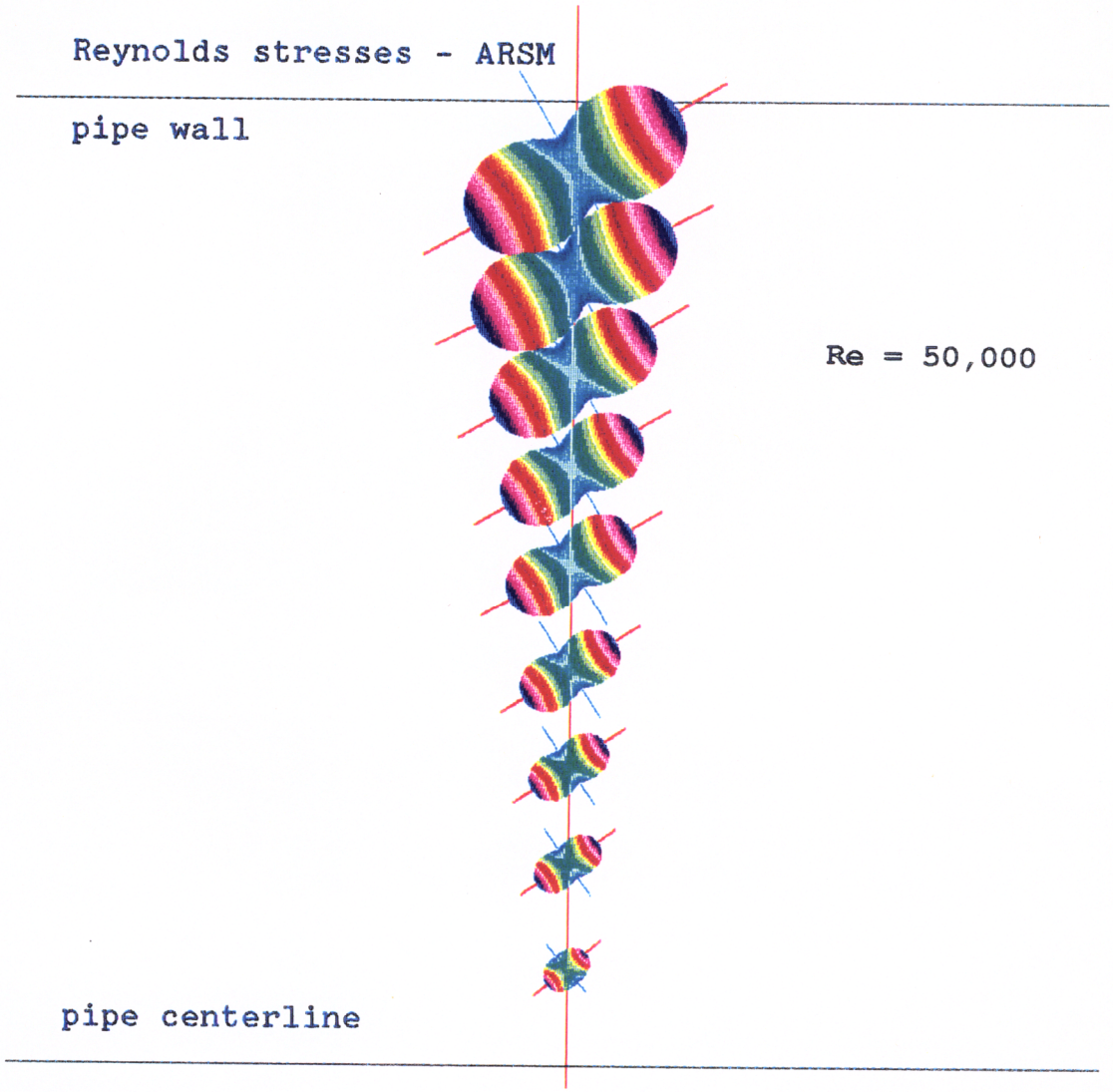

Fig 26 Glyphs for ARSM Predictions in Fully Developed Pipe Flow; Re = 50,000

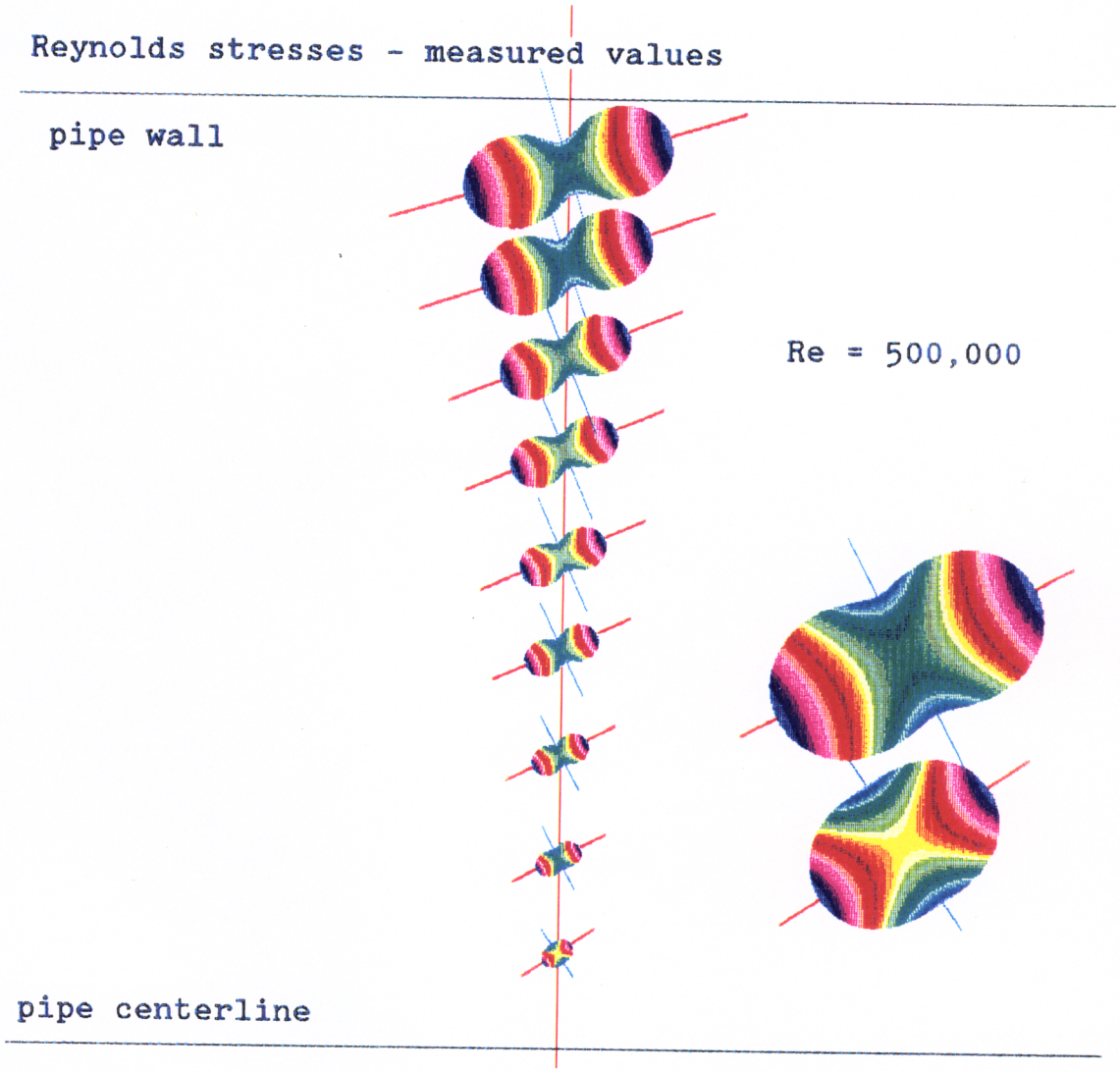

Fig 27 Glyphs for Measured Reynolds Stress Tensors in Fully Developed Pipe Flow; Re = 500,000

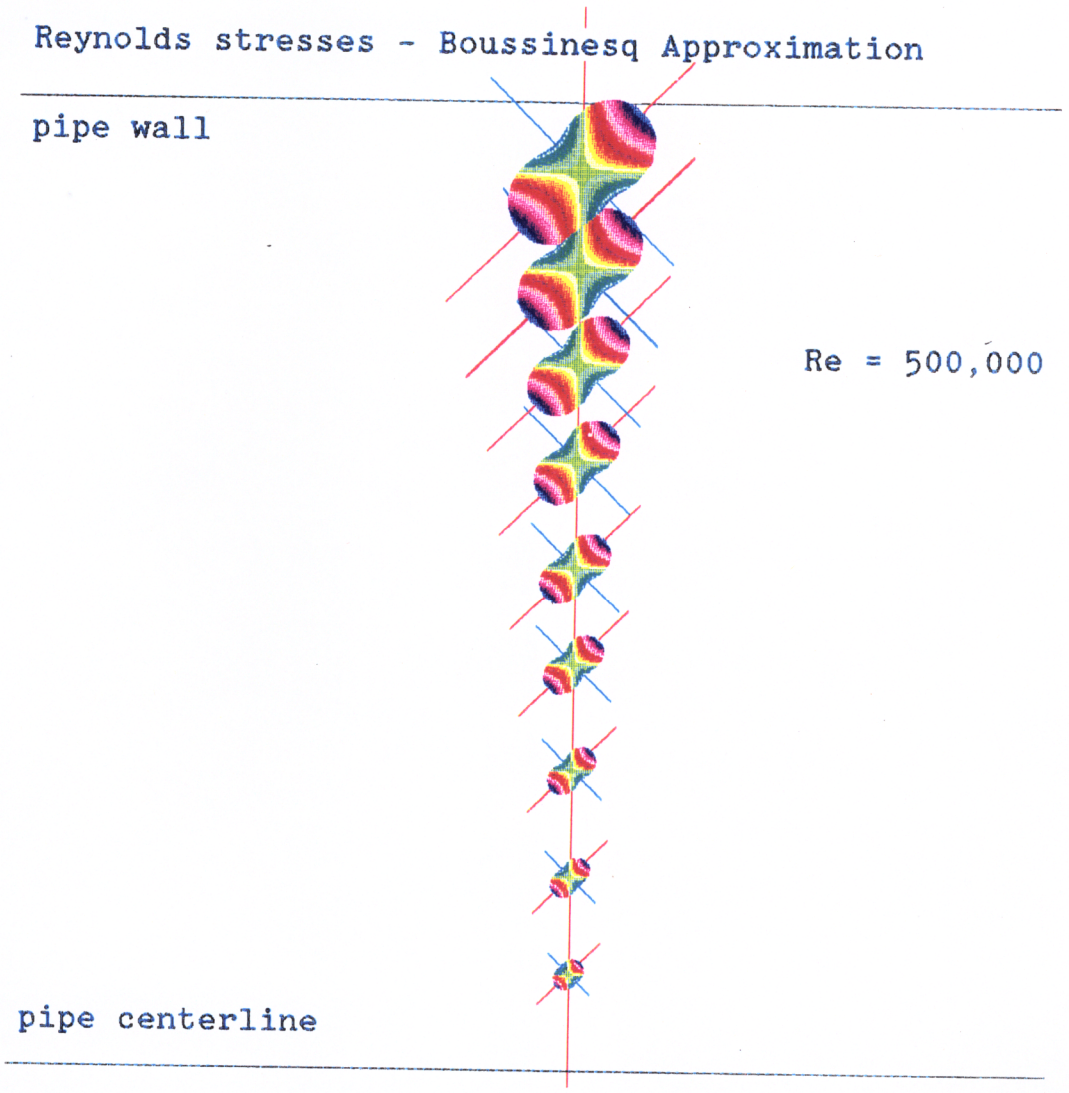

Fig 28 Glyphs for the Boussinesq Approximation Predictions in Fully Developed Pipe Flow; Re = 500,000

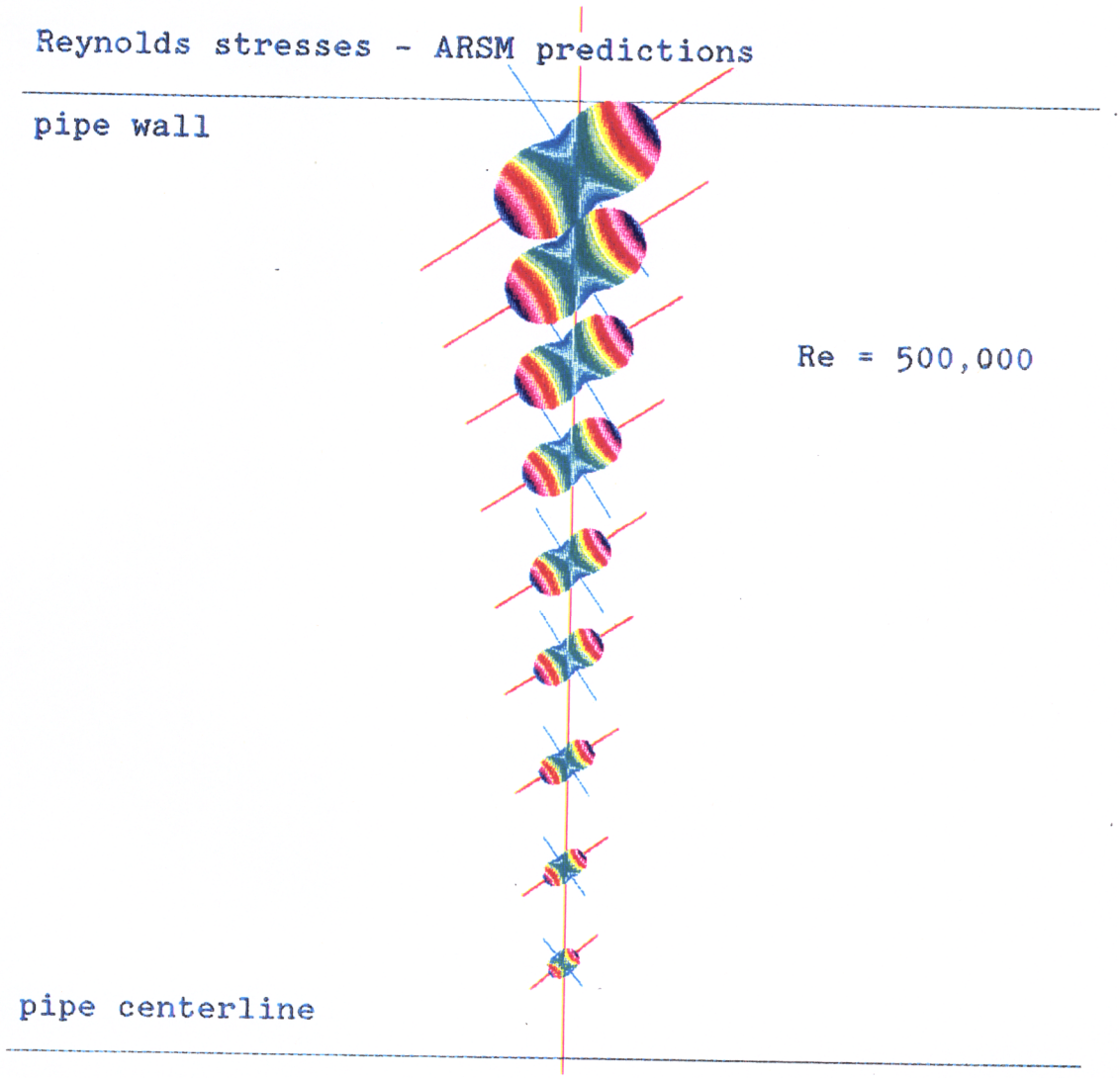

Fig 29 Glyphs for ARSM Predictions in Fully Developed Pipe Flow; Re = 500,000

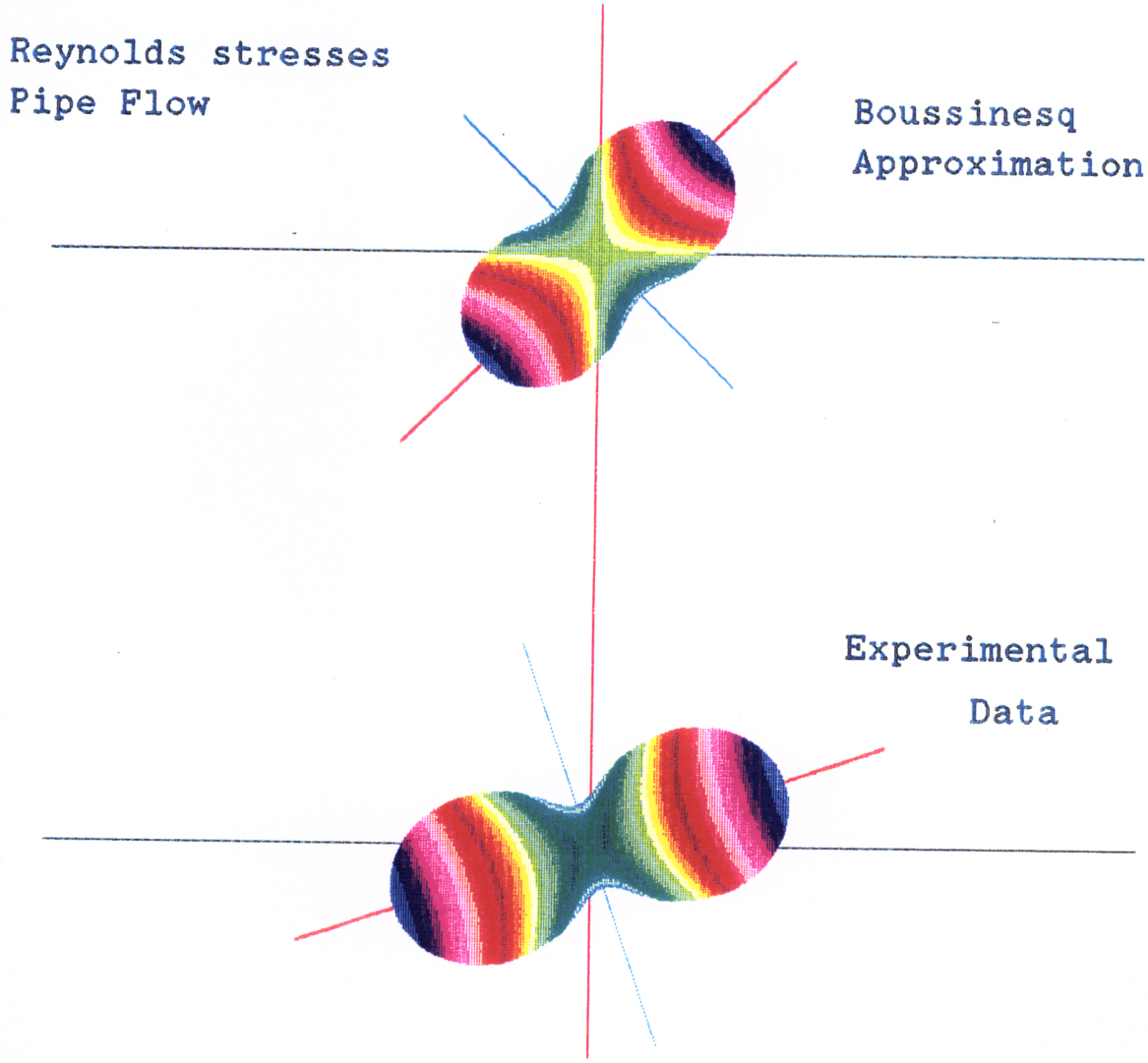

Fig 30 Boussinesq Approximation and Experimental Data Glyph Comparisons for the Near Wall Point in Fully Developed Pipe Flow; Re = 50,000

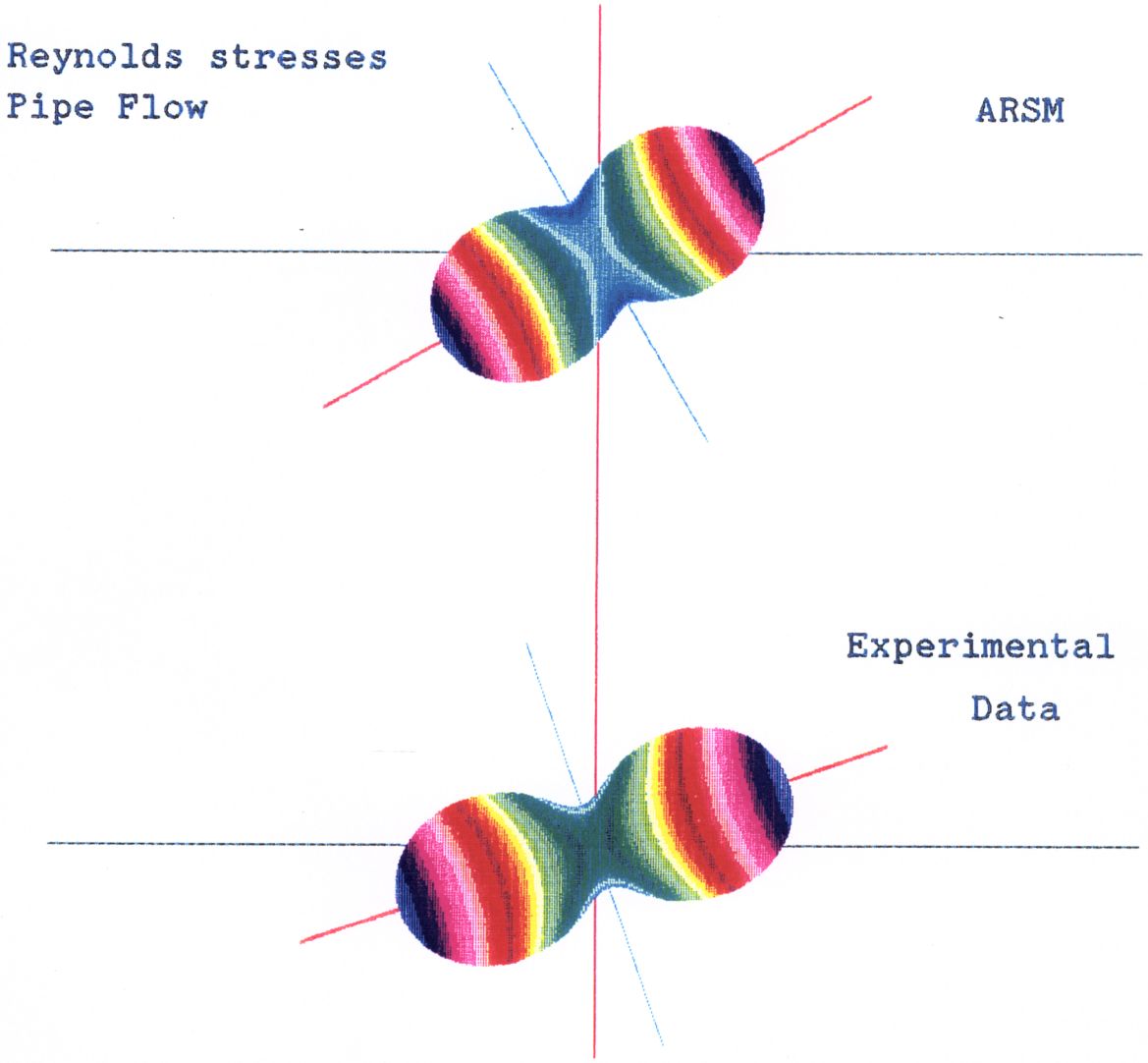

Fig 31 ARSM and Experimental Data Glyph Comparisons for the Near Wall Point in Fully Developed Pipe Flow; Re = 50,000

6.4.2.1 General Observations

An examinination of the distributions of glyphs in Figures 24-29 reveals that three features of the measured Reynolds stress glyphs are reproduced in both models. These features are manifestations of common factors found in both the measured and modeled Reynolds stress tensors used to create the glyphs.

First, the glyphs for the data and the two models at corresponding points in the flow are of the same size. This is an effect of using the turbulence kinetic energy calculated from the measured data in the two models. Since the turbulence kinetic energy is proportional to the sum of three normal Reynolds stresses, and the length of the glyph in a given direction is also proportional to a normal Reynolds stress, it follows that glyphs with equal turbulence kinetic energies will have the same general size. An accurate distribution of the turbulence kinetic energy is therefore shown in both models.

Second, it can be seen that all the glyphs are oriented so that the middle principal direction is in the circumferential direction, pointing out of the page. This is a result of both the measured and modeled Reynolds stress tensors having zero components for $\overline{uw}$ and $\overline{vw}$. With only one non-zero shearing component, a rotation about only one axis is required to orient the coordinate system in principal directions. The axis of rotation is the middle principal direction which remains aligned with the original circumferential coordinate axis. This is an example of planar stress discussed in Section 2.2.4.

Third, the shapes of the glyphs for both the measured data and the two models become more spherical as the pipe centerline is approached. This means that, for each

case, the Reynolds stress tensor is becoming more isotropic near the pipe centerline, and the two models are predicting this phenomenon accurately. The state of isotropic stress occurs when all the shear stresses equal zero and all the normal stresses equal one another. As indicated by the experimental measurements shown in Figure 21, these conditions are approached near the pipe centerline. The two models accurately predict this because the turbulence production, and therefore the $\overline{uv}$ shear stress, from the measured data is used in both models. When $\overline{uv} = 0$, Equations (55) and (56) show that the Boussinesq approximation and the ARSM both predict normal stresses equal to one another. A state of isotropic stress therefore results.

6.4.2.2 Glyph Representations of Individual Stress Components

A careful inspection of the glyphs shown in Figures 24-29 reveals how the normal stress components in x,r,ϕ coordinates vary relative to one another with the change in radial position. These relations are given as the shape and coloring of the glyphs. With these considerations, important differences between the radial distributions of measured turbulent stresses and the predictions of the Boussinesq approximation and the ARSM can be discerned.

In Figure 24, glyphs for Laufer's Reynolds stress measurements at Re = 50,000 are shown. The glyphs for the two points closest to the pipe centerline were enlarged for clearer presentation. To ascertain how the magnitudes of the $\overline{uu}$, $\overline{vv}$, and $\overline{ww}$ stresses

relate to one another, the glyphs color and length in the directions of the pipe based coordinate system will be studied.

Consider first, the glyph closest to the pipe centerline. At the center of the glyph, surrounding the point where the circumferential axis would protrude, is an area of constant green color. The green extends vertically in the radial direction and nearly horizontally along the x-axis forming an X-shape. This X-shape on the glyph surface indicates directions in which the normal stresses have near equal magnitudes. Since this green X surrounds the radial and the circumferential axes, the glyph reveals that the $\overline{vv}$ and $\overline{ww}$ stresses have magnitudes that are nearly equal. Because the green X is not aligned in the axial direction as well, the value of the $\overline{uu}$ stress must be different. Using the color coding as a reference, it is clear that the glyph is longer in the axial direction, so that $\overline{uu}$ must be larger than $\overline{vv}$ and $\overline{ww}$.

The glyph directly above the first also has a constant color X-shape centered about the circumferential axis. The X-shaped color is still oriented vertically, but extends less horizontally than on the previous glyph. This color again provides a reference of near equal stress magnitudes that can be used to conclude that the $\overline{vv}$ and $\overline{ww}$ are equal. Because the colored X-shape is oriented at a larger angle to the axial direction, the value of the $\overline{uu}$ stress must be getting larger compared to the $\overline{vv}$ and $\overline{ww}$ stresses.

These constant colored X-shapes can be seen on all the glyphs shown in Figure 24. Using these colored X-shapes as a reference of directions in which the normal stresses

have equal magnitudes, the relative magnitudes of the $\overline{uu}$, $\overline{vv}$, and $\overline{ww}$ stress components throughout the pipe radius can be determined. This process reveals that near the pipe centerline all the normal stress components are nearly equal, with the $\overline{uu}$ stress having a slightly higher value. Moving away from the centerline, first the $\overline{uu}$ stress begins to grow larger compared to the $\overline{vv}$ and $\overline{ww}$ stresses, and then the $\overline{ww}$ stress becomes larger than the $\overline{vv}$ stress. As the pipe wall is approached the $\overline{uu}$ stress is largest stress, and the $\overline{ww}$ stress is larger than the $\overline{vv}$ stress.

The same type of analysis can be performed on the glyphs shown in Figure 27, for the flow at Re = 500,000. This reveals the same general trend in the relations between the normal stress components.

The glyphs corresponding to the Boussinesq approximation shown in Figures 25 and 28 can also be analyzed to determine how the normal stresses vary relative to one another throughout the pipe. These two figures show that all the glyphs corresponding to the Boussinesq approximation have light green colored X-shapes oriented perfectly in the axial and radial directions. This means that the glyph is of the same length in the axial, radial, and circumferential directions, and, therefore, $\overline{uu} = \overline{vv} = \overline{ww}$. This is the result indicated by Equation (55).

Likewise, the glyphs corresponding to the ARSM, shown in Figures 26 and 29, also have a common color X-shape for every point. In these figures, the colored X is oriented vertically, but not horizontally. All the glyphs can be seen to be longer in the

horizontal direction. This shows that the ARSM predicts equal the $\overline{vv}$ and $\overline{ww}$ stresses, and a higher $\overline{uu}$ stress, at every point in the pipe flow. This is consistent with Equation (56).

This type of analysis is a demonstration of how information regarding Reynolds stresses in specific directions can be seen within the glyph construction. In this way, the glyphs can reproduce information shown in the individual Reynolds stress component plots.

6.4.2.2 Orientation of Principal Directions

Since the transformation of the coordinate system from flow coordinates to principal directions requires a rotation about only one axis, it can be defined with one angle. Here, the angle between the axial flow direction and the major principal direction will be used. This angle will be referred to as the transformation angle.

From the glyph pictures, it can be seen that the Boussinesq approximation always predicts the same transformation angle, for every point, regardless of Reynolds number. By comparison, the ARSM and the measured data have smaller transformation angles than the Boussinesq approximation, with the angles for the measured data generally being lower than the ARSM angles.

The differences between the data, ARSM, and Boussinesq approximation transformation angles at a point in the pipe flow can also be analyzed with the use of Mohr's circles. Figure 32 shows Mohr's circles, for the near wall point at Re = 50,000,

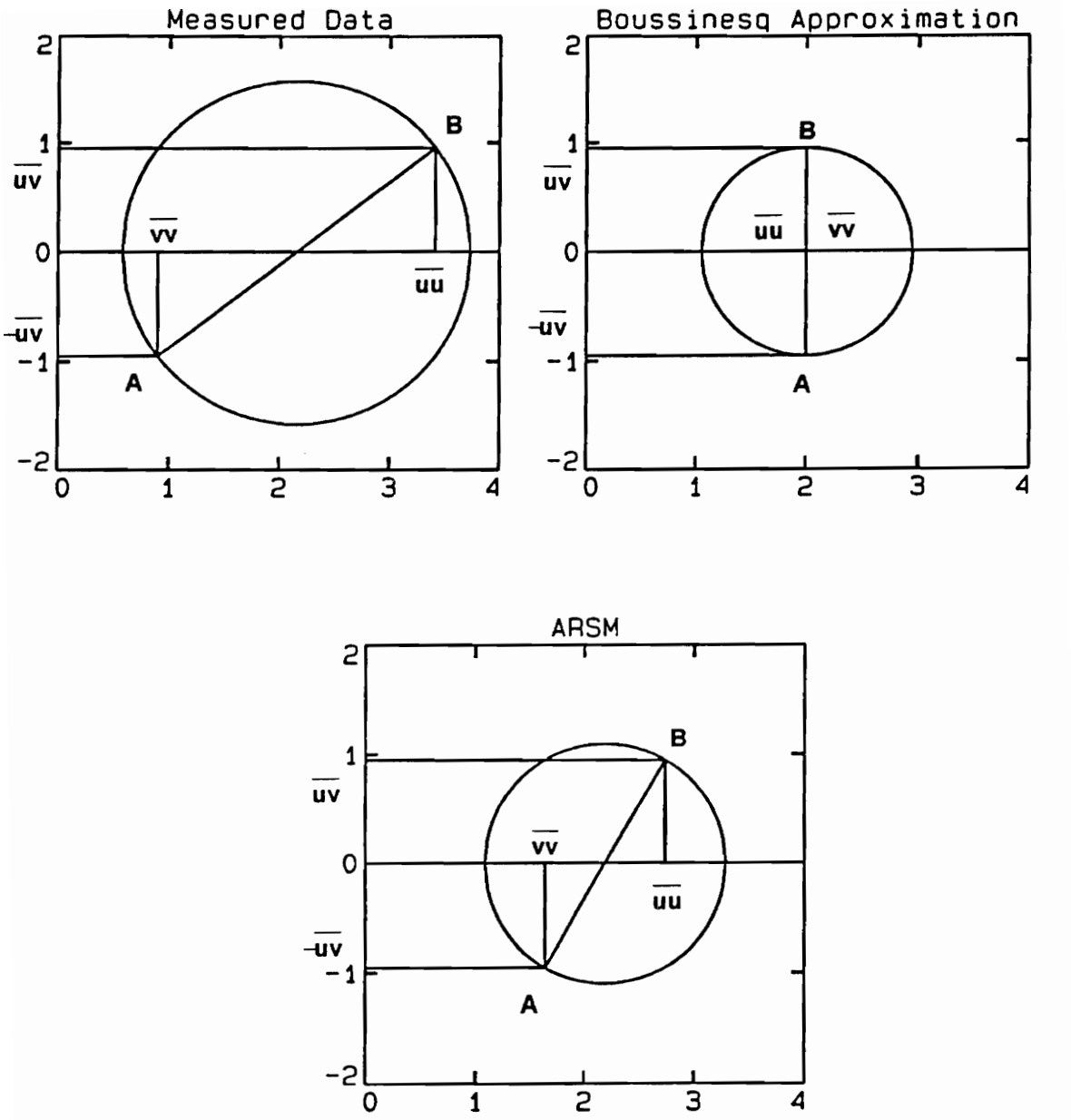

Fig. 32 Mohr's Circles for a Near Wall Point in Fully Developed Pipe Flow, Re = 50,000

corresponding to the measured data and the Bossinesq approximation and ARSM predictions. These circles show the variation of the normal and shear stresses as the coordinate system is rotated about the circumferential axis. Indicated on each of the Mohr's circles are the $\overline{uu}$, $\overline{vv}$, and $\overline{uv}$ stress components, as well as the major and minor principal values. Note that on each circle, the $\overline{uv}$ stress is the same. Also, as discussed before, the angle between the line joining the $\overline{uu}$ and $\overline{vv}$ stresses, line AB on the three circles, and the x axis is equal to twice the angle between the major principal direction and the x flow coordinate axis. Since the Boussinesq approximation always predicts the same magnitudes of these normal stress components, the Mohr's circle shows that the transformation angle will always equal 1/2 of 90°, or 45°. The measured value for the $\overline{uu}$ stress is higher than the ARSM $\overline{uu}$ stress prediction, and the measured value for the $\overline{vv}$ stress is lower than the ARSM $\overline{vv}$ stress prediction. The Mohr's circle indicates that under these conditions the transformation angle to principal directions will always be lower for the data than it is for the ARSM.

6.4.2.3 Degree of Anisotropy

The tensor glyphs also indicate the degree of anisotropy of the stress tensors by their shape. A more anisotropic stress tensor has a larger difference between the magnitudes of the major and minor principal stresses. Differences in the degrees of anisotropy are therefore shown as differences in the lengths of the glyphs in the principal

directions. The more elongated the glyph is in the major principal direction and the shorter the glyph is in the minor principal direction, the higher the degree of anisotropy.

The glyph pictures in Figures 24-29 clearly show that the degree of anisotropy of the data and the two models increases as the wall is approached. This is seen for both Reynolds numbers. The glyphs for the measured data have a higher degree of anisotropy than the two models. Differences between the shapes of the two modeled stress glyphs, however, are harder to distinguish. The enlarged glyph pictures in Figures 30 and 31, however, show the Boussinesq glyph to be slightly shorter than the ARSM glyph in the major principal direction. This suggests that the ARSM predicts a slightly more anisotropic tensor.

At the higher Reynolds number, the glyphs tend to be thicker in the direction of the minor principal axis when compared to their lower Reynolds number counterparts. This indicates a higher relative minor principal stress and means that the measurements and the models both show a higher degree of isotropy at the higher Reynolds number.

6.4.3 Quantitative Tensor Glyph Information

Since the tensor glyphs are only pictorial representations of the Reynolds stress tensors, no quantitative information about the orientation of principal directions or the degree of anisotropy is given. Because of this, plots were made to quantify this information.

The transformation angles for the data and models at both Reynolds numbers are shown in Figure 33. This plot shows the Boussinesq approximation predicting angles of 45° for all points at both Reynolds numbers. This is consistent with the analysis of the transformation angles using the Mohr's circle in the previous section. Since the experimental data results in calculated transformation angles that vary, and never have a value of 45 degrees, this indicates a substantial failure of the Boussinesq approximation. Figure 33 also shows that the ARSM predicts transformation angles that are up to 12 degrees higher than experimental measurement at Re = 50,000. At Re = 500,000, the ARSM transformation angles are 5 to 20 degrees higher than the data.

The degree of anisotropy of the tensors is roughly measured by the value, $(P_{MAX} - P_{MIN})/k$. Here, P_{MAX} and P_{MIN} correspond to the major and minor principal stress values, respectively. Again, k is the turbulent kinetic energy. From now on, this relation will be referred to as the anisotropy value.

The anisotropy values are shown in Figure 34 for both Reynolds numbers. Both plots show that the anisotropy value of the measured data rises as the wall is approached. The two models, however, predict that the anisotropy value should level off somewhat. Each model predicts lower anisotropy values than the data, with the Boussinesq approximation faring worse than the ARSM. At Re = 50,000, the ARSM is off by as much as 0.30, and the Boussinesq approximation shows errors as high as 0.40. For the flow at Re = 500,000, the ARSM is off by as much as 0.40, and the Boussinesq approximation underpredicts by as much as 0.45. These results are consistent with the

tensor glyph pictures, in which the data appeared more anisotropic than either model predicted.

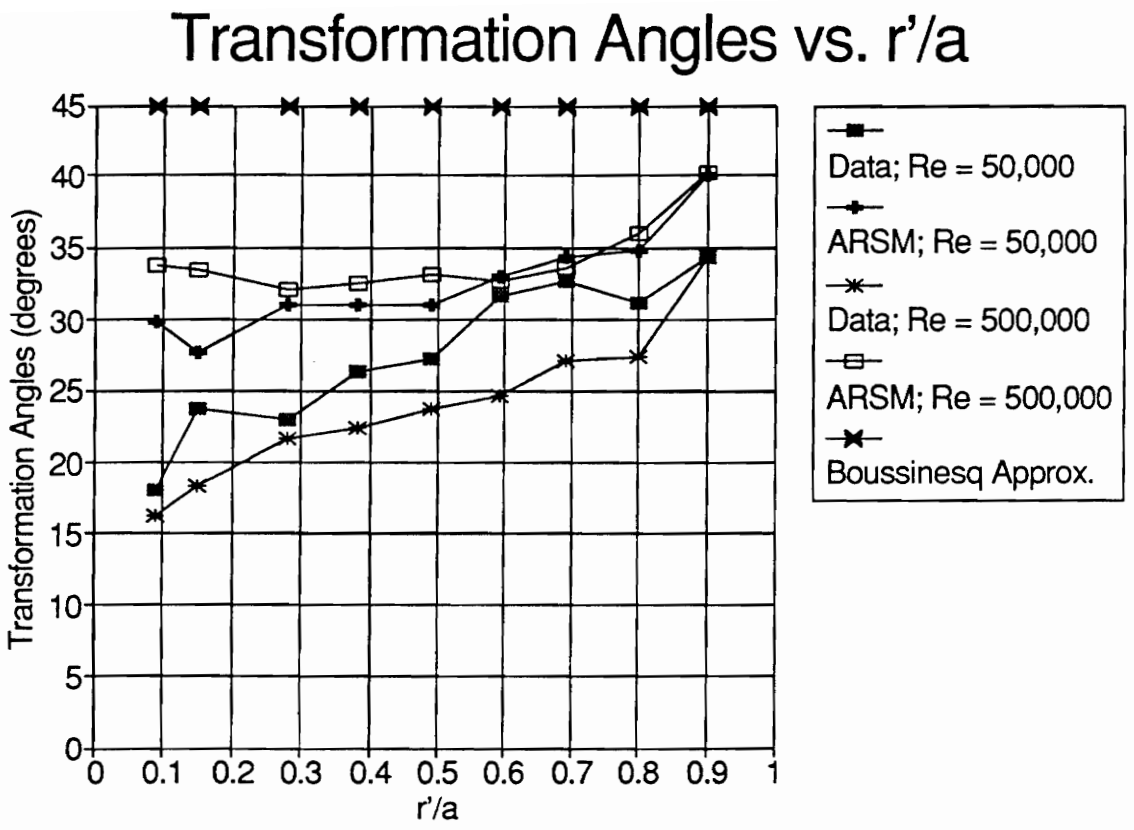

Fig. 33 Transformation Angles to Principal Directions for Fully Developed Pipe Flow

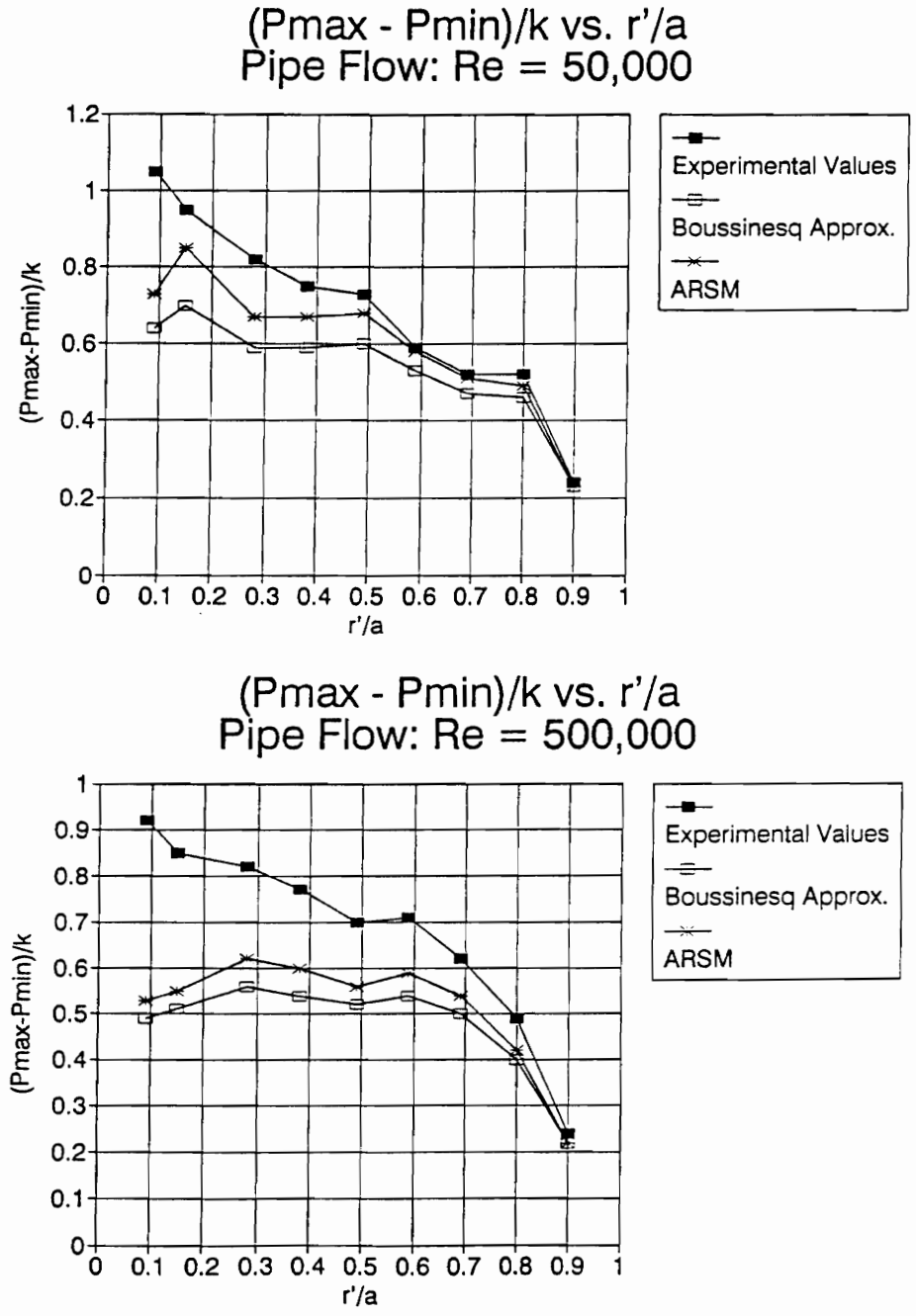

Fig. 34 Degree of Anisotropy Values for Fully Developed Pipe Flow

6.4.4 Dissipation Rates and Model Constant Evaluation

Turbulence dissipation rates for both Reynolds numbers were calculated according to the Kolmogorov-Prandtl expression and an equation derived from the ARSM. For the flow at a Reynolds number of 50,000, the dissipation calculations were compared with the experimental measurements of Laufer. These are shown in Figure 35. As with the Reynolds stress predictions, the dissipation rates were calculated with the turbulence production and kinetic energy determined from experimental measurements. The dissipation rates were non-dimensionalized by multiplying by the factor $a / U_o U_\tau^2$.

6.4.4.1 Laufer's Dissipation Measurements

Laufer estimated radial distributions of turbulence dissipation rates in fully developed pipe flow. Recall that the rate of turbulence dissipation is defined as

$$\varepsilon = \nu \overline{\frac{\partial u_i}{\partial x_j} \frac{\partial u_i}{\partial x_j}}. \tag{57}$$

Laufer directly measured five of the nine fluctuating velocity gradient components at radial stations in the pipe. He estimated the other four through the Kolmogorov assumption of local isotropy of turbulence at the microscales at which dissipation is known to occur. In cylindrical coordinates, this assumption results in:

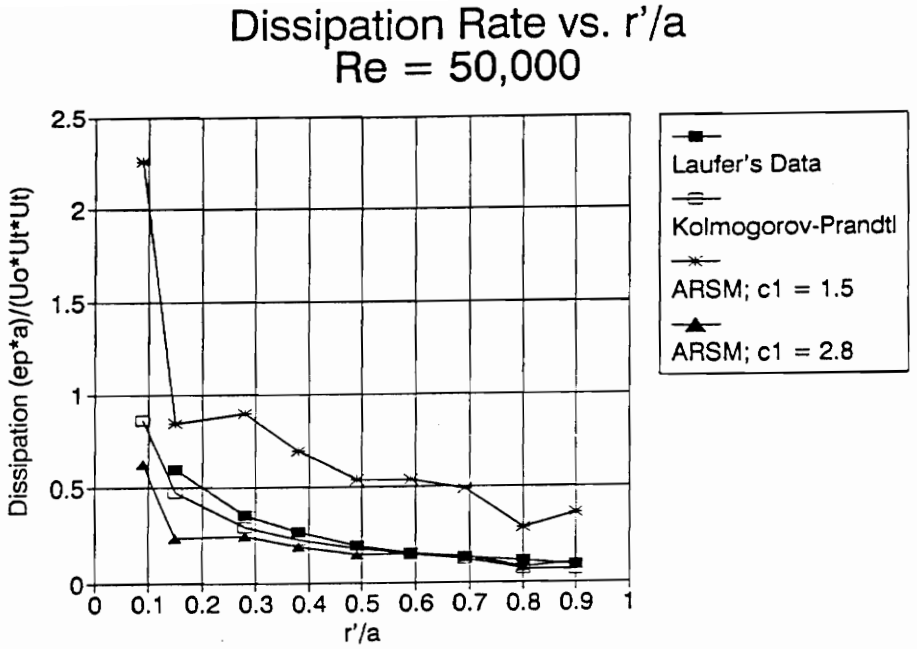

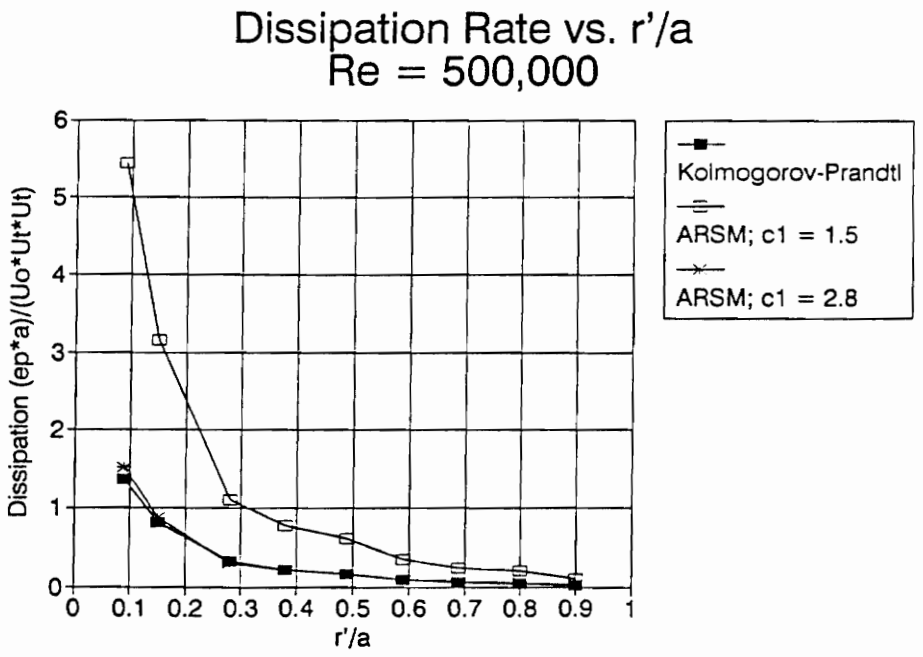

Fig. 35 Dissipation Measurements and Calculations for Fully Developed Pipe Flow

$$\overline{\left(\frac{\partial u}{\partial r}\right)^2} = 2\overline{\left(\frac{\partial v}{\partial r}\right)^2} = \overline{\left(\frac{\partial w}{\partial r}\right)^2} \tag{58}$$

$$\frac{1}{r^2}\overline{\left(\frac{\partial u}{\partial \phi}\right)^2} = \frac{1}{r^2}\overline{\left(\frac{\partial v}{\partial \phi}\right)^2} = \frac{2}{r^2}\overline{\left(\frac{\partial w}{\partial \phi}\right)^2} \tag{59}$$

Laufer measured all the velocity fluctuation gradients with respect to the axial direction and the gradients of u with respect to the radial and circumferential directions. He then estimated the remaining four with the relations shown in Equations (58) and (59).

Measurements were made at Reynolds numbers of 50,000 and 500,000. The measurements at Re = 500,000, however, were inaccurate due to the increased probe sensitivity to amplifier noise and wire effects at the higher frequencies at which dissipation occurs. For this reason, only the measurements at Re = 50,000 are considered here.

In general, Figure 35 shows Laufer's measurements remaining fairly constant throughout most of the cross sectional pipe area. The dissipation rate then rises as the wall is approached.

6.4.4.2 The Kolmogorov-Prandtl Expression

The Kolmogorov-Prandtl expression is

$$\nu_t = C_\mu' \sqrt{k} L, \tag{60}$$

where C_μ' is a constant and L is a length scale. Dimensional analysis can be used to relate the dissipation rate to the turbulence kinetic energy and the length scale. This gives:

$$\nu_t = C_\mu \frac{k^2}{\varepsilon}, \tag{61}$$

where ε is the rate of turbulence dissipation. For pipes, the constant C_μ is taken to be 0.09 [6]. Turbulence models based upon the Boussinesq approximation use this relation to link the turbulent viscosity to the dissipation rate.

A general expression for the turbulent viscosity based upon the experimentally measured rate of turbulence production is given in Equation (40). This expression can be used in Equation (61) to derive an equation for the turbulence dissipation rate. For pipe flow this is given as:

$$\varepsilon = -\frac{C_\mu k^2 \frac{\partial U}{\partial r}}{\overline{u_1 u_2}}. \tag{62}$$

Figure 35 shows close agreement between dissipation calculations based upon the Kolmogorov-Prandtl expression and Laufer's measurements. This was expected because the constant C_μ was determined specifically for pipe flows. The calculation of C_μ was based upon the assumption that a local equilibrium shear layer exists in which the rate of turbulence production equals the rate of turbulence dissipation. Experiment shows this to be true at most radial positions in a pipe [17]. For simple shear layers such as pipe flow, equating the expressions for production and dissipation results in:

$$P = -\overline{uv}\frac{\partial U}{\partial r} = -\frac{C_\mu k^2 \frac{\partial U}{\partial r}}{\overline{uv}} = \varepsilon\,, \tag{63}$$

which can be reduced to:

$$C_\mu = \left(\frac{\overline{uv}}{k}\right)^2. \tag{64}$$

For pipe flows, it has been found that $\overline{uv}/k = 0.3$ across most of the pipe radius [18]. As a result, $C_\mu = 0.09$.

6.4.4.3 ARSM Dissipation Calculations

An expression for the rate of turbulence dissipation was derived in Section (5.0) and is given in Equation (42). For pipe flow, this expression reduces to:

$$\varepsilon = -\frac{(1-\gamma)}{(C_1-1)}\frac{\overline{ku_2^2}\,\frac{\partial U}{\partial r}}{\overline{u_1u_2}} + \frac{\overline{u_1u_2}\,\frac{\partial U}{\partial r}}{C_1-1}, \qquad (65)$$

as derived in Appendix D and shown in Equation (D.20). Note that all Reynolds stresses in this expression are ARSM and not measured values. This equation is coupled with the ARSM, given in Equation (37) in Section (5.0).

Values for the constants C_1 and γ were originally taken from the full Reynolds stress modeling work of Launder et al. [7]. In their research, model predictions were compared to measurements of nearly homogeneous shear flow made by Champagne et al. [19], and it was determined that using C_1=1.5 and γ=0.6 resulted in reasonable predictions.

Using these values in the ARSM to calculate dissipation rates, however, results in predictions that are significantly higher than the experimental measurements. This is seen in Figure 35 for Re = 50,000. For the flow at Re = 500,000, the calculations based upon the Kolmogorov-Prandtl expression were assumed accurate since they compared well with the dissipation rate measurements for the flow at Re = 50,000. At the higher

Reynolds number, therefore, it can be seen that the ARSM calculations again predicted dissipation rates that were too high.

To correct the errors in the dissipation rate calculations, the value for C_1 was changed to match the measured data and the Kolmogorov-Prandtl calculations. It has been shown that the value for γ must remain close to 0.6 for most flows [7], so this value was not changed. By considering dissipation rate predictions for both Reynolds numbers, it was found that $C_1 = 2.8$ best fit the data. The results of the ARSM predictions using this value are shown in Figure 35.

Rodi [9] suggested that for simple shear layers such as pipe flow the ARSM equation for the shear stress, $\overline{uv}$, is in the form of the Kolmogorov-Prandtl formulation of the eddy viscosity concept

$$\overline{uv} = -\nu_t \frac{\partial U}{\partial r} = -C_\mu \sqrt{k} L \frac{\partial U}{\partial r} \tag{66}$$

where the constant C_μ is replaced by a function of P/ε in the form:

$$C_\mu = \frac{2}{3}\frac{1-\gamma}{C_1}\left[1-\frac{1}{C_1}(1-\gamma P/\varepsilon)\right] \Big/ \left[1+\frac{1}{C_1}(P/\varepsilon - 1)\right]^2 . \tag{67}$$

This relation can be used as another way of calculating the ARSM constants for fully developed pipe flow. It has been stated previously that for pipe flow $C_\mu = 0.09$ and $P/\varepsilon = 1.0$ across most of the pipe radius. If the value for γ is again taken to be 0.6, then the only unknown in Equation (67) is C_1. Solving Equation (67) results in $C_1 = 2.8$, just as the dissipation calculations suggested.

6.4.5 Gradients of $\overline{u_i u_j}/k$ in Pipe Flow

The primary assumption used in the derivation of the ARSM is that $\overline{u_i u_j}/k$ should be constant or vary slowly throughout the flowfield. With this assumption, terms containing gradients of $\overline{u_i u_j}/k$ can be neglected. The details of this assumption appear in Appendix A with Equations (A.6) and (A.7). With these two equations, it is assumed that:

$$(1)\quad \left|\frac{\overline{u_i u_j}}{k}\frac{Dk}{dt}\right| >> \left|k\frac{D\left(\overline{u_i u_j}/k\right)}{Dt}\right|$$

$$(2)\quad \left|\frac{\overline{u_i u_j}}{k}D_k\right| >> \left|C_s\frac{\partial}{\partial x_k}\left(\frac{k^2}{\varepsilon}\overline{u_k u_l}\frac{\partial \overline{u_i u_j}/k}{\partial x_l}\right)+\frac{k}{\varepsilon}C_s\overline{u_k u_l}\frac{\partial k}{\partial x_l}\frac{\partial \overline{u_i u_j}/k}{\partial x_k}\right|.$$

Put simply, these relations can be interpreted as saying that the magnitudes of the gradients of the turbulence kinetic energy far exceed the gradients of $\overline{u_i u_j}/k$. An easy

way to check the validity of this assumption in fully developed pipe flow is then to plot the gradients of turbulence kinetic energy and $\overline{u_i u_j}/k$, and see how they relate to one another.

For fully developed pipe flow, the Reynolds stress components vary only in the radial direction. Gradients in this direction were therefore estimated. Specifically, the gradients were taken with respect with r'/a. They were calculated as a ratio in the form of:

$$\left| \frac{\partial\left(\frac{\overline{u_i u_j}}{k}\right) \Big/ \partial\left(\frac{r'}{a}\right)}{\left(\frac{\overline{u_i u_j}}{k}\right)} \right| \quad \text{or} \quad \left| \frac{\partial k \Big/ \partial\left(\frac{r'}{a}\right)}{k} \right|.$$

The absolute values were taken because the relative magnitudes were being compared. These quantities for $\overline{uu}/k$, $\overline{vv}/k$, $\overline{ww}/k$, and k are shown in Figure 36 for both Reynolds numbers.

For both Reynolds numbers, the assumption that the turbulence kinetic energy gradients are much higher than the $\overline{u_i u_j}/k$ gradients seems weakest as the pipe wall is approached. At the point closest to the pipe wall, the $\overline{vv}/k$ gradients actually exceed gradients of k at both Reynolds numbers, and $\overline{ww}/k$ gradients are larger than the k gradients for the flow at Re = 50,000. At most other points, the k gradients have larger

magnitudes than the $\overline{u_i u_j}/k$ gradients, but the differences between the two do not seem to be as large as relations (1) and (2) suggest.

These results indicate that the underlying assumption of the ARSM may be a source of error for this model. It must be noted, however, that this analysis compares quantities that are only approximations to the quantities given in relations (1) and (2). A more complete evaluation of relations (1) and (2) may therefore be required to determine with more confidence the applicability of the ARSM.

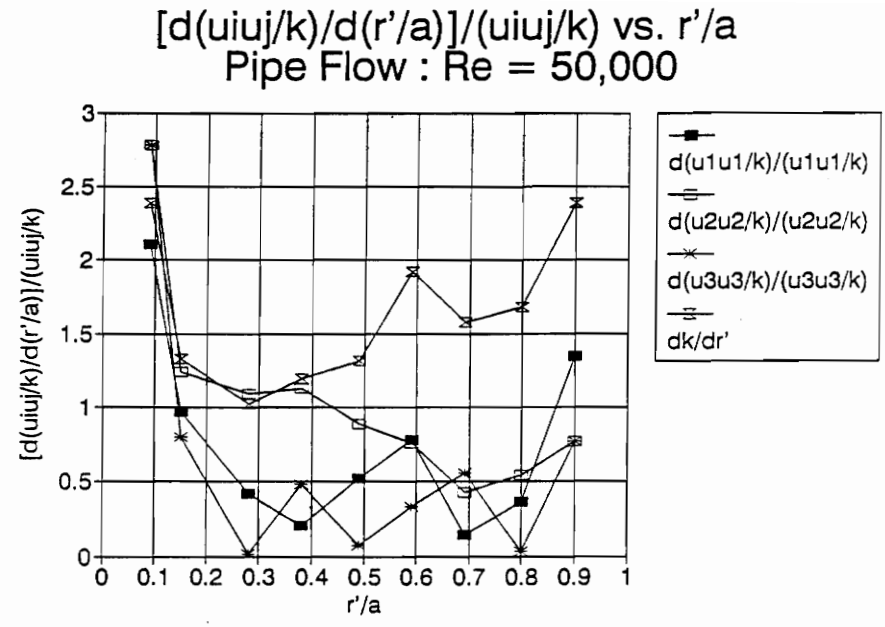

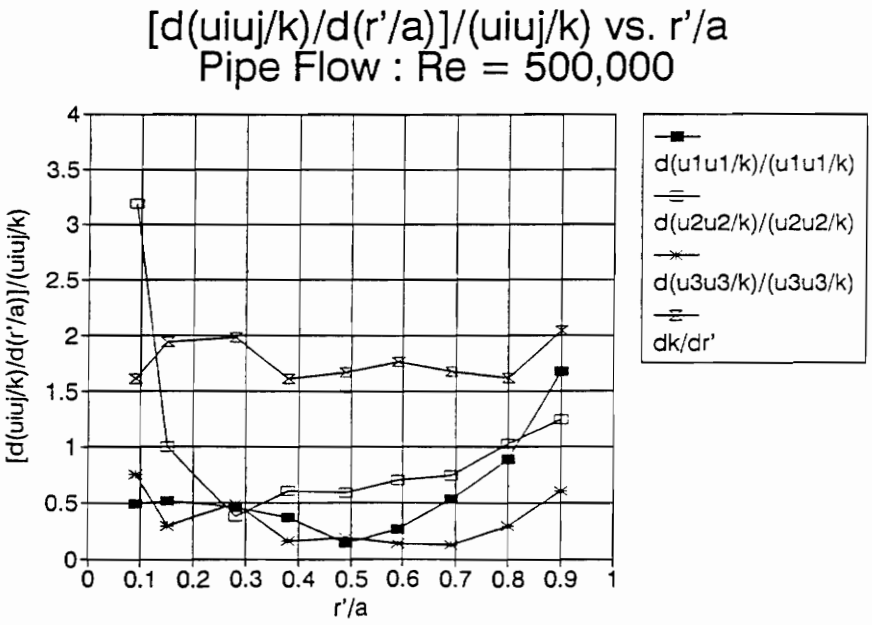

Fig. 36 Gradients of u_iu_j/k in Fully Developed Pipe Flow

7.0 Analysis of Flow in a Tip Leakage Turbine Cascade

7.1 Cascade Geometry and Previous Experimental Study

An analysis analogous to the one performed for fully developed pipe flow was performed on a flow through a linear turbine cascade with tip leakage. This analysis was based upon the measurements made by Moore et al. [1] in the VPI&SU tip leakage turbine cascade. The cascade geometry is shown in Figure 37 [1]. Here the inlet freestream velocity, U_o, is 20 m/s, and the freestream turbulence intensity, Tu, is 0.4%. The Reynolds number based on blade axial chord, c, and the flow exit velocity was 4.4 x 10^5.

Measurements of Reynolds stress and mean velocity components were made in a plane upstream of the trailing edge at X/c = 0.96. Measurements of mean flow velocity components were also made on an additional plane further upstream in order to evaluate velocity gradient components. The measurements were made using hot-wire anemometry and a rotatable two-wire endflow probe.

The coordinate system used for the measurements is shown in Figure 37. The primary flow coordinate, x, was taken to be parallel to the mean camber line of the turbine blade trailing edge. The secondary flow coordinates, y and z, are perpendicular to the trailing edge mean camber line and in the spanwise blade direction, respectively.

Figure 38 [20] shows contours of the primary flow velocity component, U, with the superposition of secondary flow velocity vectors at the measurement points in the

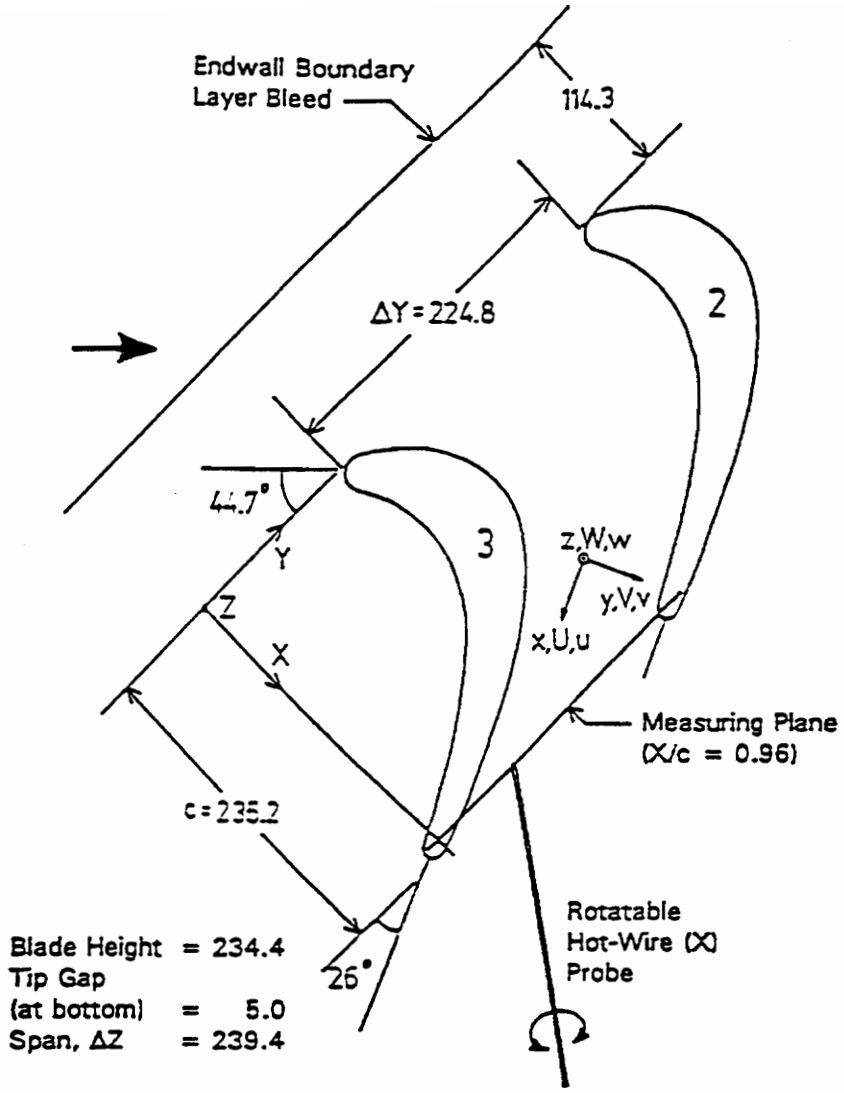

Fig. 37 Tip Leakage Turbine Cascade Geometry [20]

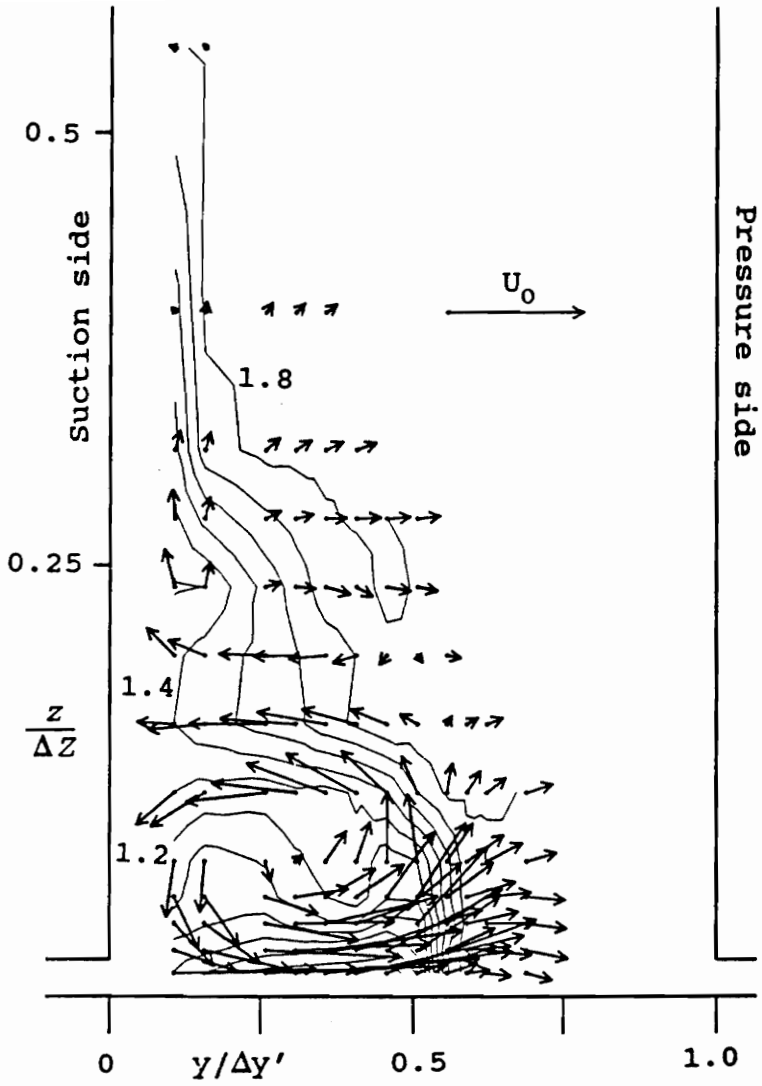

Fig. 38 Mean Velocity Components in a Tip Leakage Turbine Cascade [20]

plane. These vectors are the resultant of the velocity components V and W. All three velocity components are normalized by the freestream inlet velocity, U_o. Here, we see the tip leakage jet flow along the endwall, separate, and circulate, forming a tip leakage vortex. The flow at the top of the tip leakage vortex approaches the blade suction side and splits. Some of the flow continues to swirl in the tip leakage vortex and the rest forms another weaker passage vortex. For a more detailed discussion see Dishart and Moore [21].

The distribution of turbulence kinetic energy is shown in Figure 39 [20]. On this figure, the turbulence kinetic energy is normalized by the factor, $U_o^2/2$. Here, the highest level of turbulence kinetic energy is near the separation point. In this region, the level rises to nearly 0.3. By comparison, the tip leakage jet has a much lower level of turbulence kinetic energy, at about 0.1. The turbulence kinetic energy generated in the separation region is convected about the tip leakage vortex core. During this convection, the level of its intensity falls somewhat.

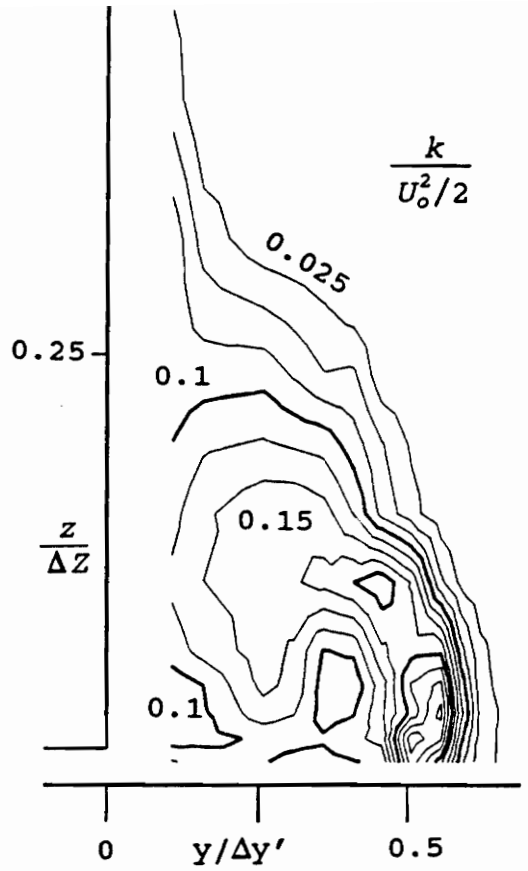

Fig. 39 Turbulence Kinetic Energy in a Tip Leakage Turbine Cascade [20]

7.2 Reynolds Stress Contour Plots

Figures 40-45 are contour plots of the Reynolds stress tensor components. On each figure, the measured stress component is shown along with the Boussinesq approximation and ARSM predictions. All stress values on these plots are non-dimensionalized by U_o^2.

On Figure 40, the $\overline{uu}$ stress is shown. On this figure, the stress predictions of the ARSM and Boussinesq approximation are more similar to one another than to the experimental data. Both models predict a $\overline{uu}$ stress that is generally higher that the experimental measurements. Throughout most of the flow region, however, the modeling errors are not more than 10. A peak in the $\overline{uu}$ stress is shown to occur near the point of endwall separation. Here, the contour plots indicate a peak ARSM $\overline{uu}$ value of 120, Boussinesq approximation values reaching 110, and a maximum measured $\overline{uu}$ stress of 90.

Figure 41 shows the $\overline{vv}$ stress values. Again, the ARSM and Boussinesq approximation are seen to be more closely related to one another than to the measured data. In general, the two models predict less variation of the $\overline{vv}$ stress than is indicated by the measurements. Throughout much of the flow, the modeled $\overline{vv}$ values are lower than the measured data. An exception occurs at the point of maximum $\overline{vv}$ intensity, again shown to occur in the endwall separation region. Here, the Boussinesq approximation

predicts $\overline{vv}$ stress values climbing to 130, while the data peaks at 120, and the ARSM only reaches 110.

On Figure 42, the $\overline{ww}$ stresses are presented. As with the $\overline{uu}$ and the $\overline{vv}$ stresses, the ARSM and Boussinesq approximation make similar predictions for this component, while differing somewhat from the data. This fact is illustrated by the highest $\overline{ww}$ stress values. The data indicates two regions where the $\overline{ww}$ stress peaks: one in the endwall separation region where the values exceed 70, and one in the convected flow region, at about $y / \Delta y' = 0.5$ and $z / \Delta z = 0.1$, where $\overline{ww}$ exceeds 80. The two models also have two regions of peak $\overline{ww}$ stress values, but only one corresponds to the data. In the convected flow region, both models predict values reaching 80, just like the measurements show. The second modeled peak $\overline{ww}$ value, however, occurs above the separation region, away from the endwall. Here, the models show $\overline{ww}$ values reaching 80 and 90, for the Boussinesq approximation and the ARSM, respectively. Besides this discrepancy, the two models yield values that are close to the experimental measurements.

On Figure 43, distributions for the $\overline{uv}$ stresses are shown. This figure shows the $\overline{uv}$ stress dropping to its lowest negative value in the region of endwall separation. Here the ARSM has values reaching -50, while the Boussinesq approximation and the measurements have values falling as low as -55. Besides this region, all three contour

plots indicate relatively low $\overline{uv}$ stress magnitudes, with values generally staying in the range of -5 to 5.

Figure 44 shows the $\overline{uw}$ stresses. Throughout most of the flow region, the $\overline{uw}$ stress was measured to have low negative values. Regions in the range of 0 to -10 fill most of the measurement plot. Both the ARSM and the Boussinesq approximation generally show the same values. In the endwall separation region, however, the measurements show the $\overline{uw}$ stress falling to -30 next to the endwall. In this region, the Boussinesq approximation predicts no significant gradient in the values. The ARSM, on the other hand, has a peak in the $\overline{uw}$ magnitudes, in a region removed from the endwall. Here, the ARSM $\overline{uw}$ values reach as low as -55.

Finally, Figure 45 shows the $\overline{vw}$ stresses. As with the normal stress components, the ARSM and the Boussinesq approximation yield similar results that are slightly different from the measurements. The $\overline{vw}$ values are predominantly positive with a region of negative values between the passage and tip leakage vortices. The measurements show the negative values extending nearer the blade suction surface than the two models. High measured values of $\overline{vw}$ occur in the endwall separation region in roughly the same places as the $\overline{uw}$ peaks, one next to the endwall and one slightly removed from it. Near the endwall, the measured $\overline{vw}$ stress reaches 35, and away from the endwall a peak value of 30 occurs. The two models, on the other hand only yield one

peak value for the $\overline{vw}$ stress, at the point removed from the endwall. Here, both models predict $\overline{vw}$ values reaching 40.

In summary, the contour plots of the Reynolds stress components suggest that the Boussinesq approximation and the ARSM are related to one another in some way. This is evidenced by the striking similarities between the two models for the $\overline{uu}$, $\overline{vv}$, $\overline{ww}$, and $\overline{vw}$ stress components. Particularly revealing are the similarities in the positions of the modeled $\overline{ww}$ and $\overline{vw}$ peak values, and their discrepancies with the measured stresses. The similarities between the ARSM and the Boussinesq approximation break down dramatically, however, for the $\overline{uw}$ stress component in the region of endwall separation. In this area, the ARSM predicts a significant gradient in the $\overline{uw}$ stress values, while the Boussinesq approximation values remain fairly constant. This anomaly does not indicate an improvement of one model over the other, since both are in considerable error when compared to the data.

These stress contour plots also suggest that the ARSM and Boussinesq approximation may yield more isotropic stress tensors than the measurements show over much of the flow domain. This is implied by the relative magnitudes of the normal stress components. Comparing Figures 40, 41, and 42, in the regions aside from the endwall separation region, the measurements generally show that $\overline{uu}$ is the smallest normal stress component while $\overline{vv}$ is the largest stress component. In these regions, the two models

give higher $\overline{uu}$ values and lower $\overline{vv}$ values, while the $\overline{ww}$ stresses have comparable magnitudes. This means that, in the models, the normal stresses are more evenly distributed, which suggests a more isotropic tensor. It must be noted, however, that the degree of isotropy can only be measured by considering the magnitudes of the principal stresses. Since these are not shown on Figures 40-45, conclusions regarding isotropy can only be made tentatively, pending further analysis.

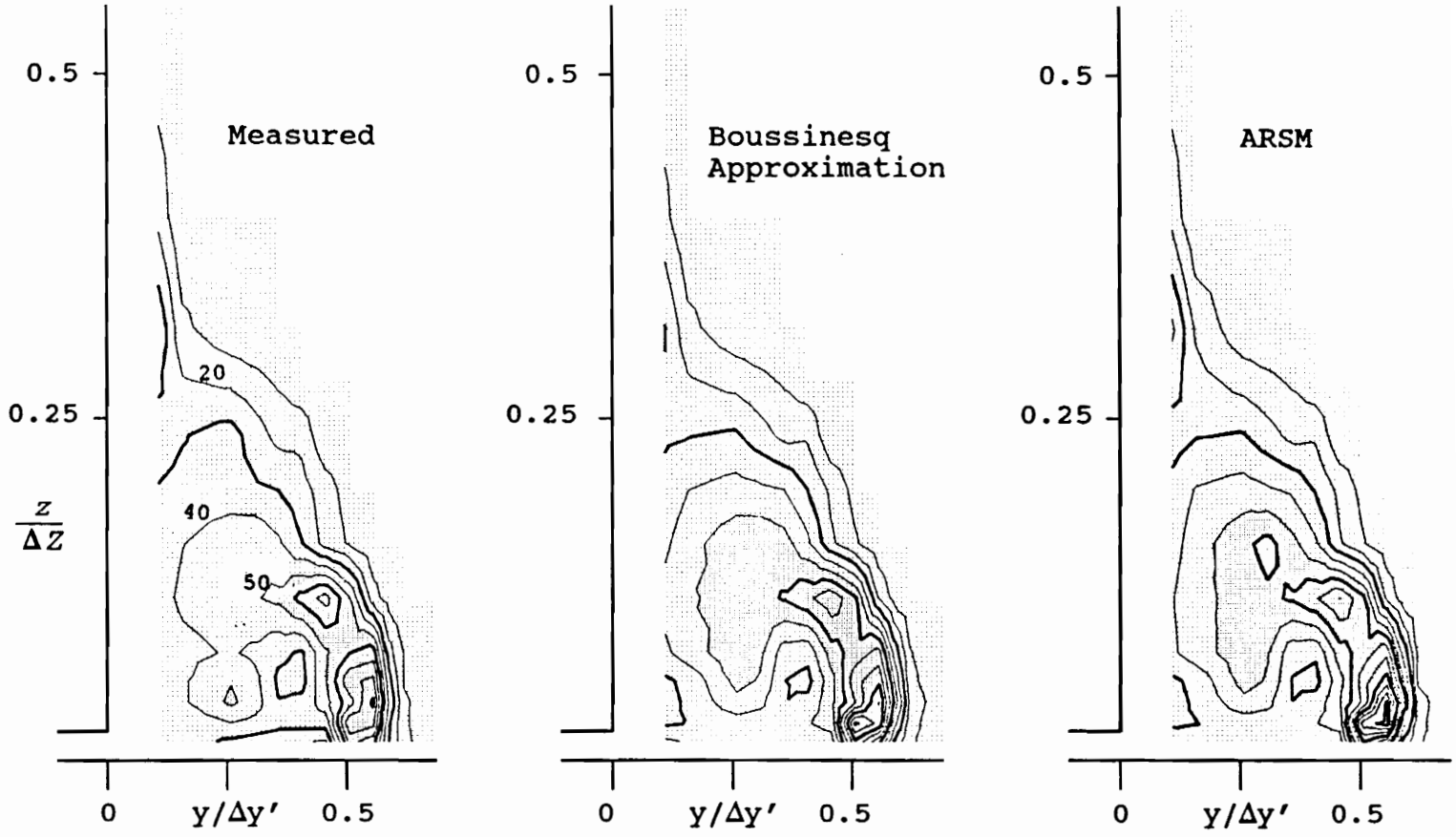

Fig. 40 Reynolds stress component plots: 1000 $\overline{uu}/U_o^2$, contour interval, 10, light shading < 50, dark shading > 50

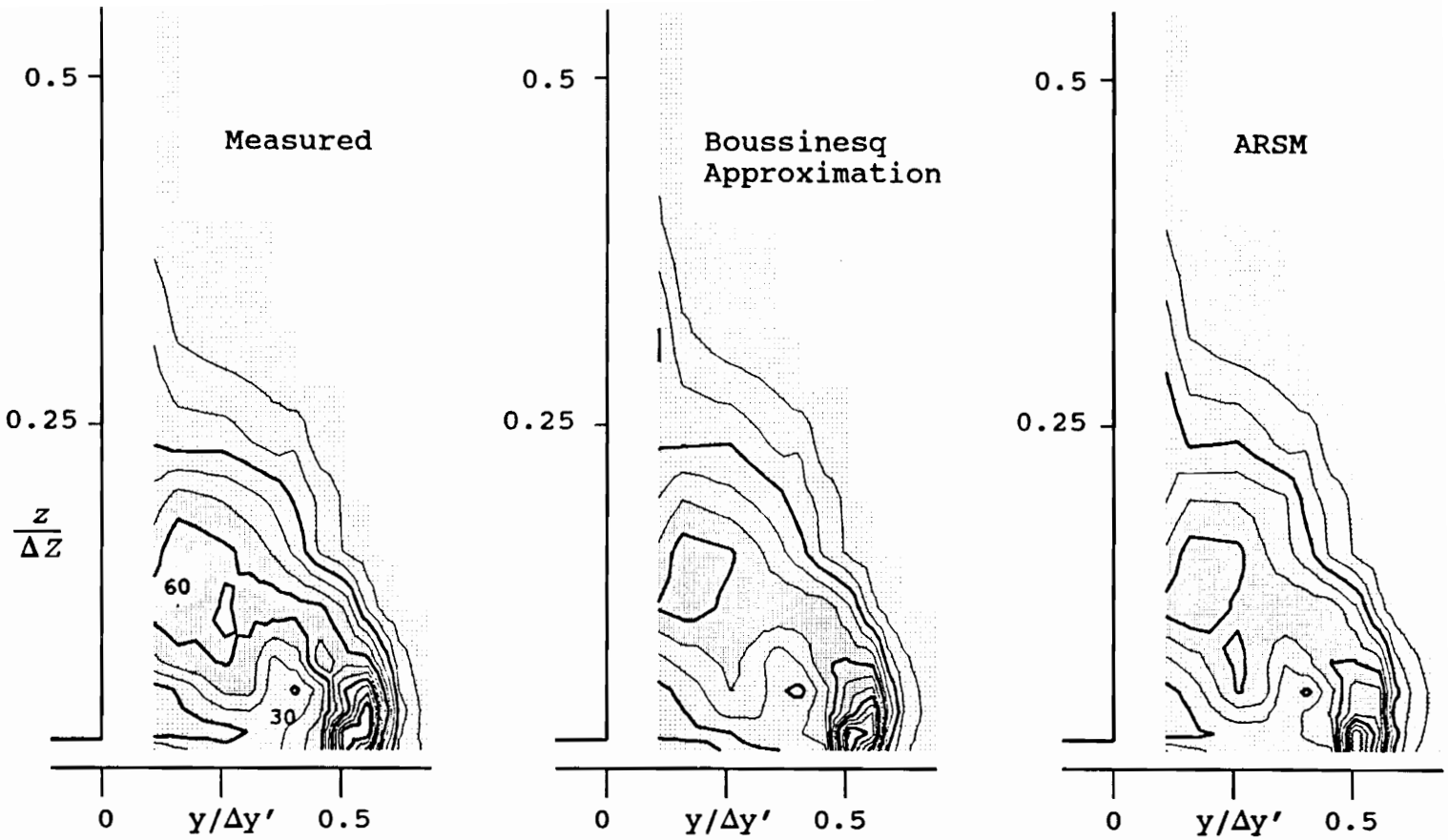

Fig. 41 Reynolds stress component plots: 1000 $\overline{vv}/U_o^2$, contour interval, 10, light shading < 50, dark shading > 50

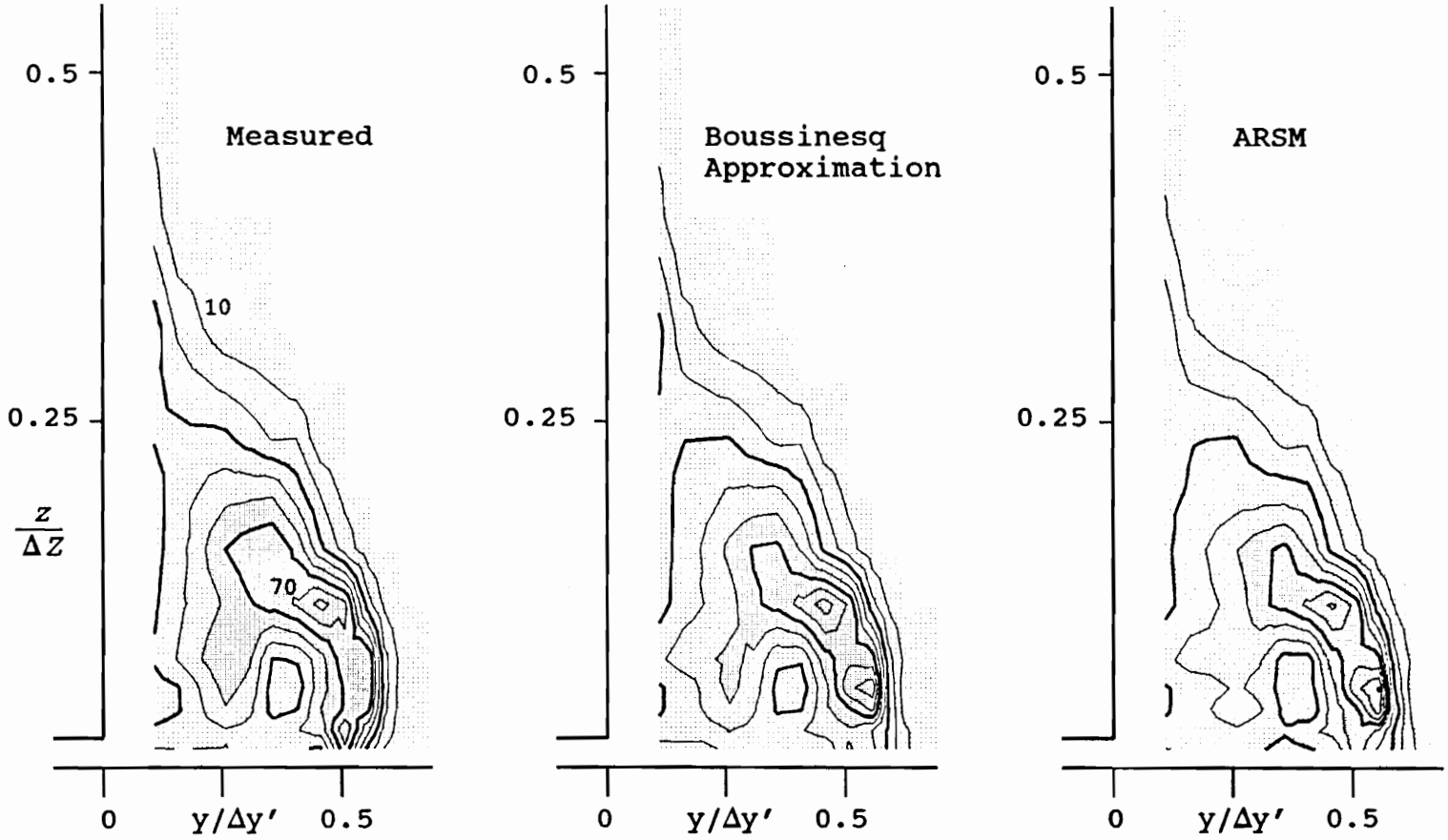

Fig. 42 Reynolds stress component plots: 1000 $\overline{ww}/U_o^2$, contour interval, 10, light shading < 50, dark shading > 50

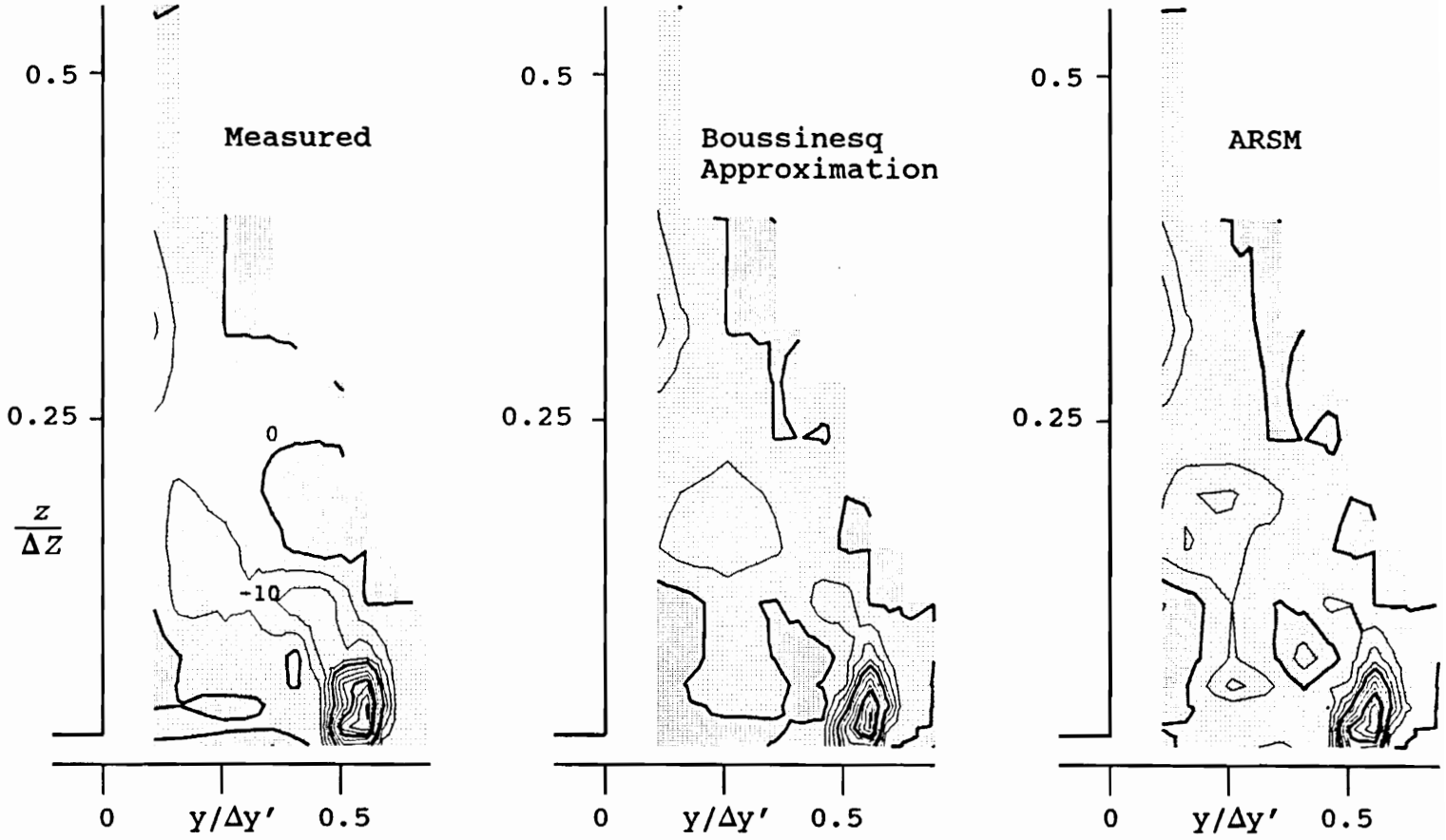

Fig. 43 Reynolds stress component plots: 1000 $\overline{uv}/U_o^2$, contour interval, 5, light shading < 0, dark shading > 0

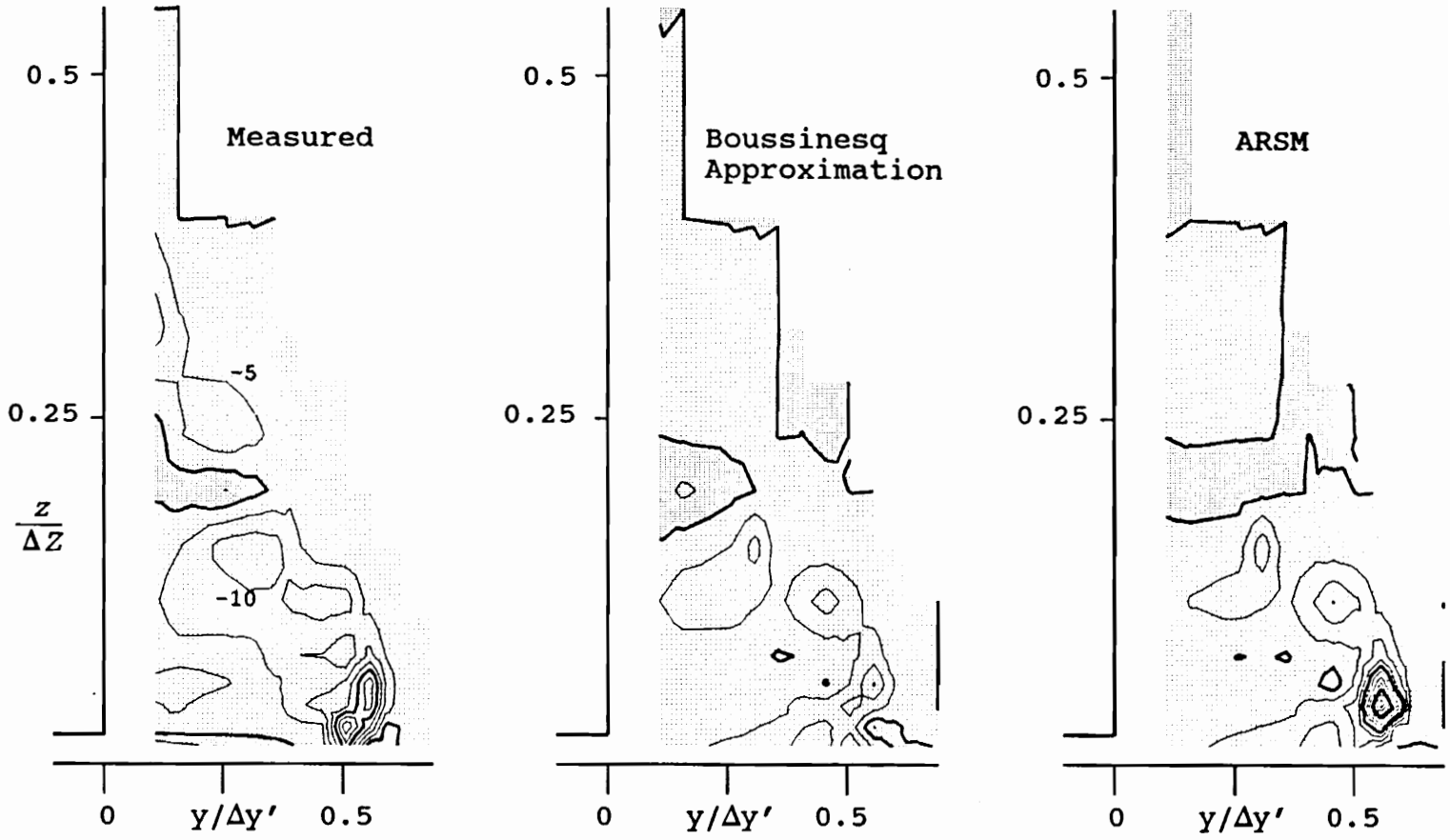

Fig. 44 Reynolds stress component plots: 1000 $\overline{uw}/U_o^2$, contour interval, 5, light shading < 0, dark shading > 0

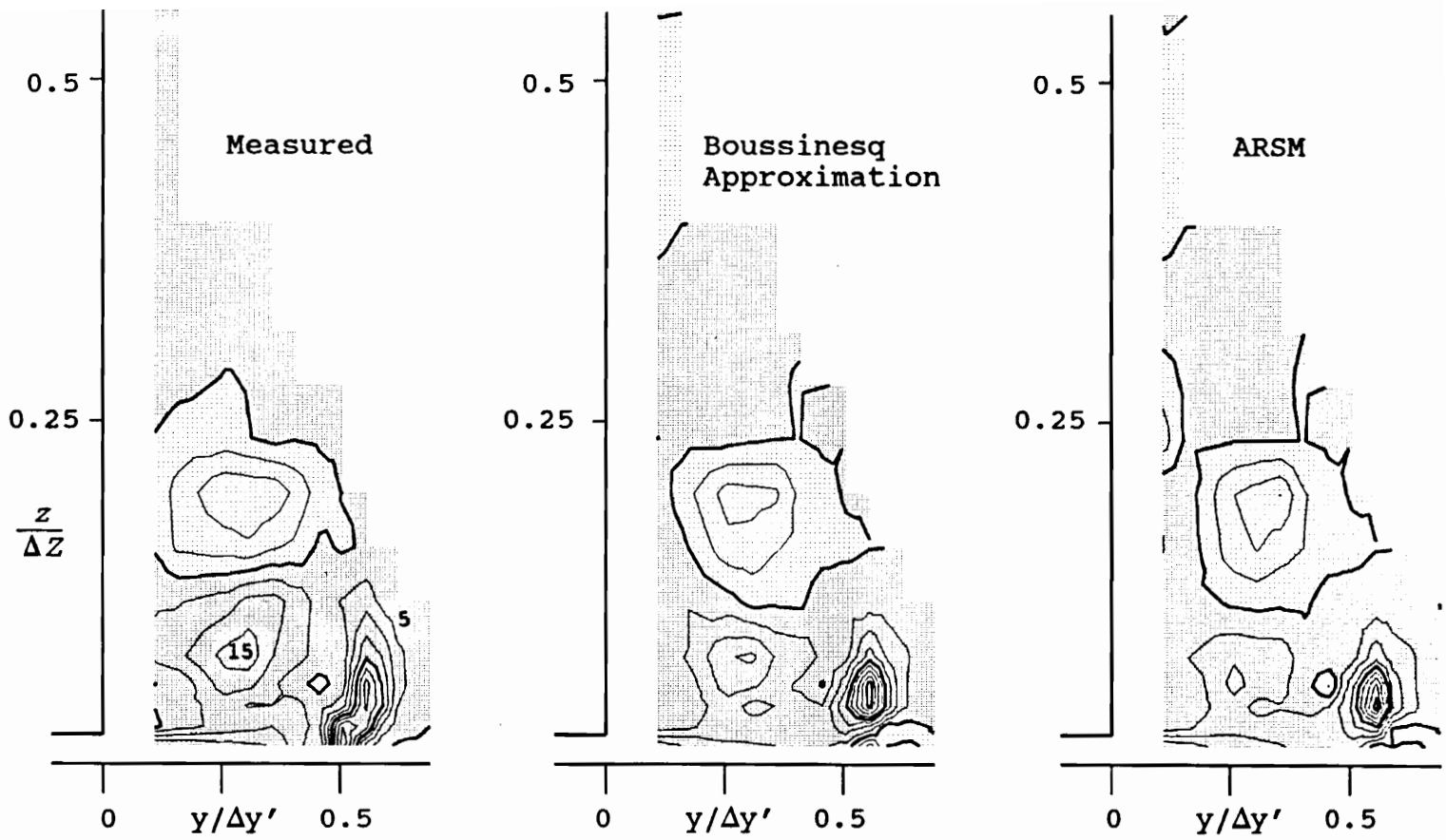

Fig. 45 Reynolds stress component plots: 1000 $\overline{vw}/U_o^2$, contour interval, 5, light shading < 0, dark shading > 0

7.3 Tensor Glyph Pictures and Associated Quantitative Measures

As with the fully developed pipe flow analysis, tensor glyphs were created for the data points in the tip leakage cascade to further study stress tensor characteristics such as the degree of anisotropy and the orientation of the principal directions. The glyphs are shown in Figures 46 to 48, with Figure 46 showing the measured Reynolds stress tensors, Figure 47 showing the Boussinesq approximation predictions, and Figure 48 giving the ARSM Reynolds stress predictions. Associated with the tensor glyph pictures are quantitative measurements of the orientation of the major principal directions and the degree of anisotropy. These are shown in Figures 49 and 50, respectively. On these five figures, ARSM and Boussinesq approximation predictions were omitted for any measurement points that did not sufficiently satisfy the continuity equation for an incompressible flow to within 0.1 U_0/c. The relative orientations of the three sets of glyphs are defined by the angles between the major principal axes. On Figure 49, the angles between corresponding major principal axes of the measured data glyphs and the Boussinesq approximation glyphs, the measured data glyphs and the ARSM glyphs, and the Boussinesq approximation glyphs and the ARSM glyphs are all presented. For this flow geometry, the degree of anisotropy is defined just as it was for the fully developed pipe flow, as $(P_{MAX} - P_{MIN})/k$. Contour plots associated with the measured Reynolds stress tensor, the Boussinesq approximation, and the ARSM are all shown on Figure 50.

Figures 46 to 48 present information concerning the Reynolds stress tensor at each measurement point in the flowfield. It is possible to consider each glyph individually,

and evaluate it in terms of the degree of anisotropy and the orientation of principal directions. This was essentially done for the fully developed pipe flow. The relatively large number of data points in the tip leakage turbine cascade, however, makes this kind of analysis extremely tedious. Instead, specific regions in the flow will be chosen, the glyphs for the measurements in these regions will be analyzed, and the corresponding modeled glyphs will be evaluated. In this way, the amount of analysis is reduced, but the usefulness of the glyphs in representing the different flow characteristics in different regions can still be demonstrated. Three regions in the tip leakage turbine cascade will be considered: the tip leakage jet region, the endwall separation region, and the flow convected above the tip leakage vortex core.

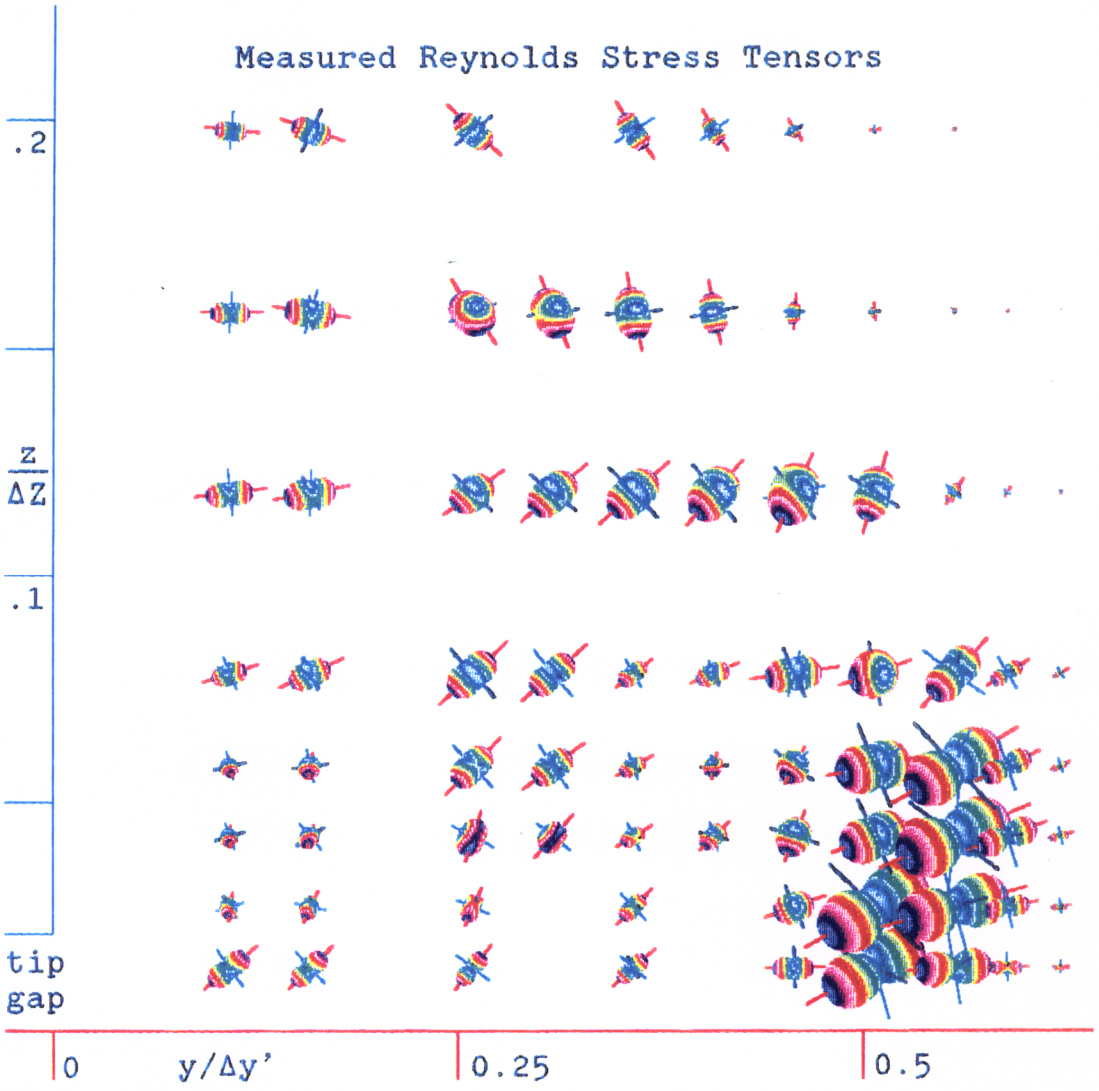

Fig. 46 Glyphs for the Measured Data in a Tip Leakage Turbine Cascade

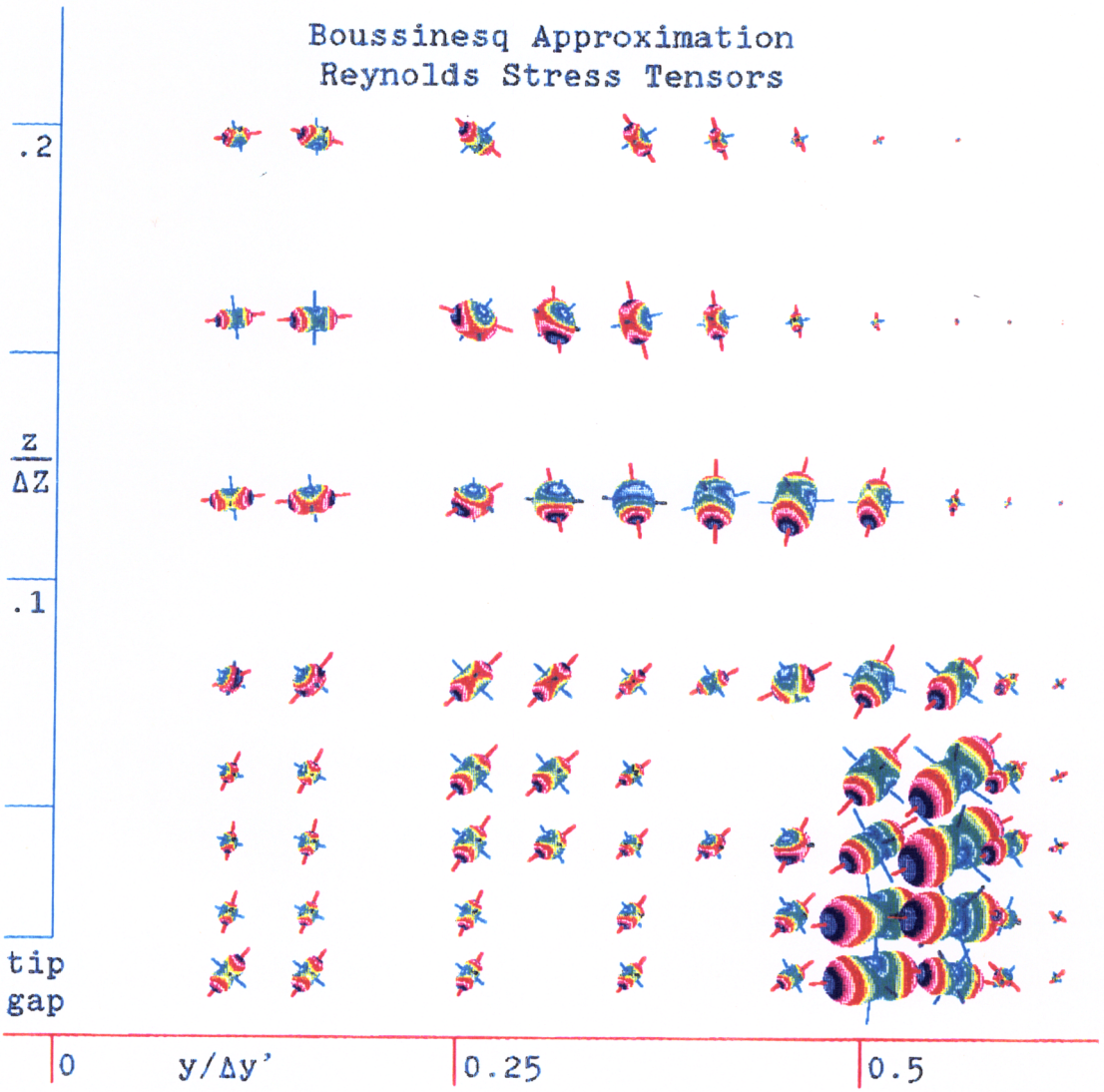

Fig. 47 Glyphs for the Boussinesq Approximation Predictions in a Tip Leakage Turbine Cascade

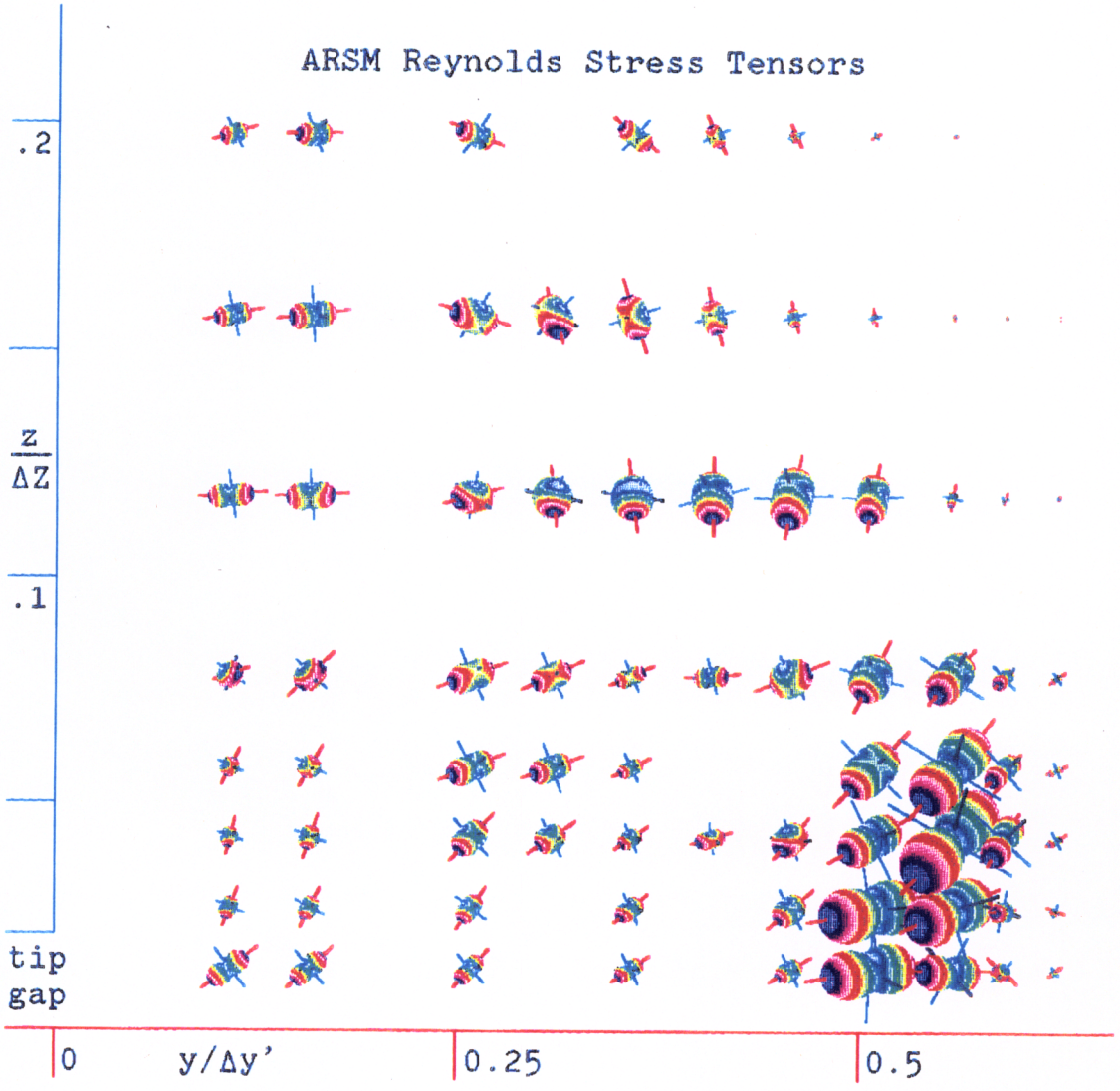

Fig. 48 Glyphs for the ARSM Predictions for a Tip Leakage Turbine Cascade

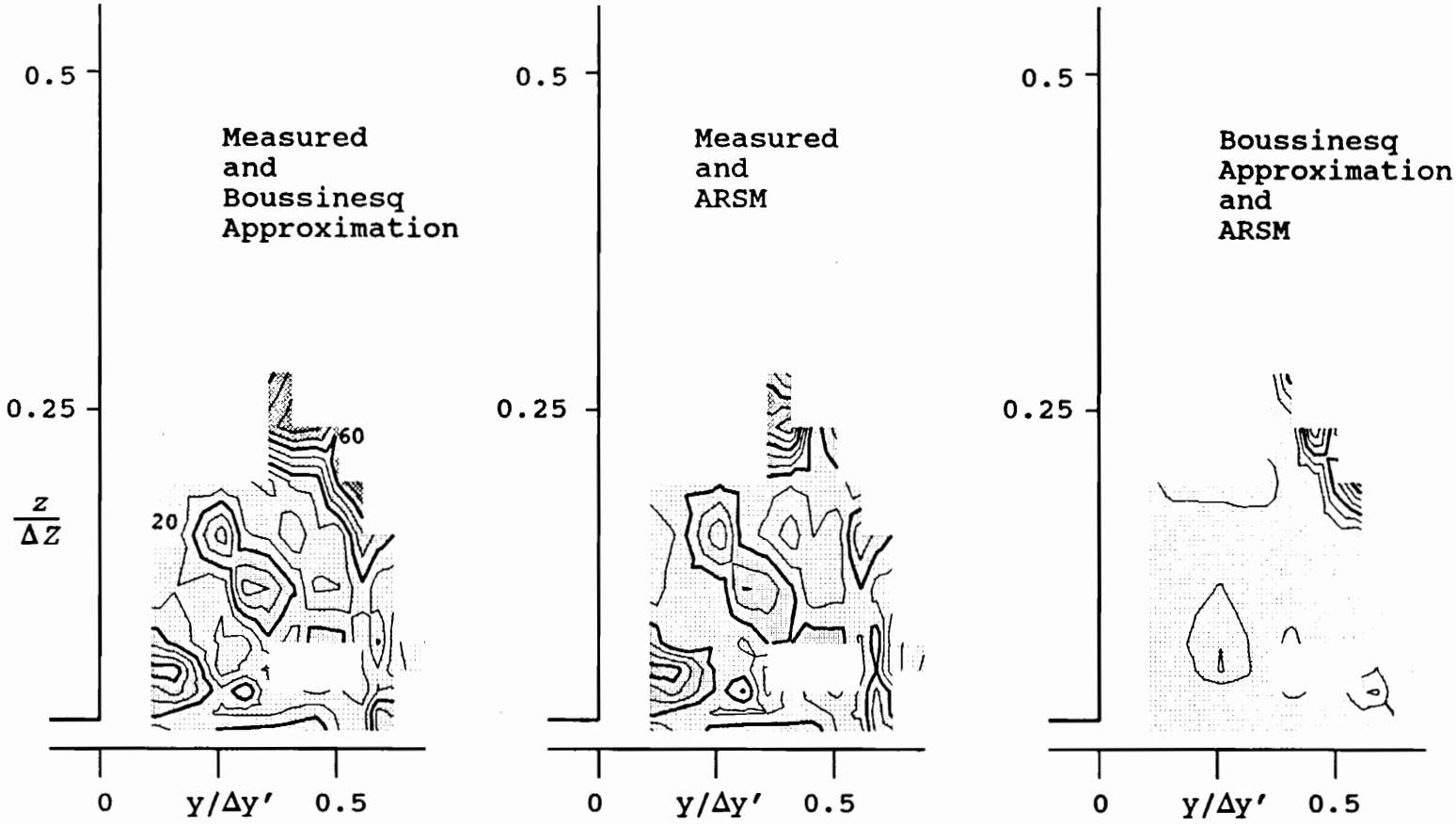

Fig. 49 Orientation Angles: contour interval, 10 degrees, light shading < 30 degrees, dark shading > 30 degrees

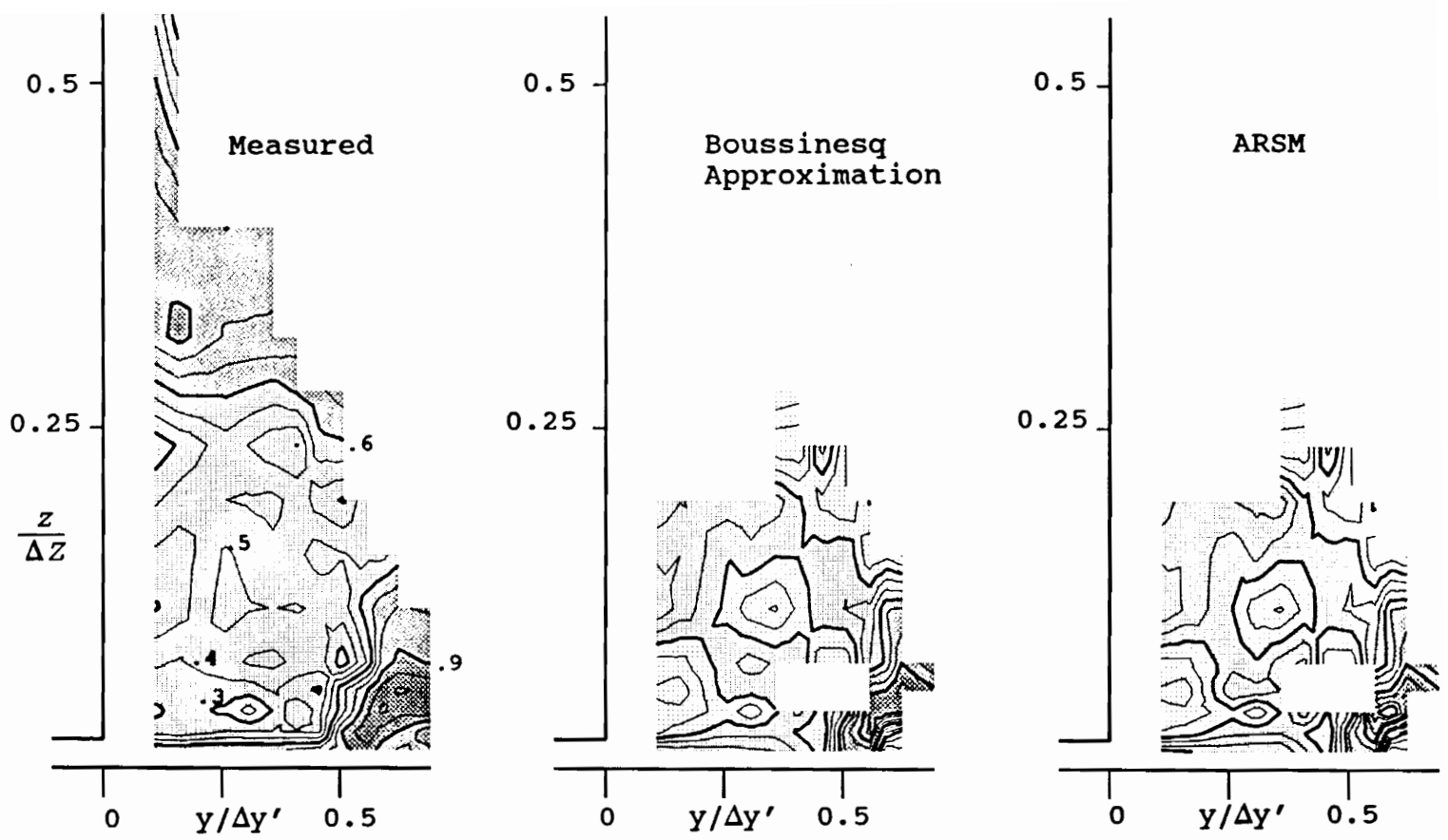

Fig. 50 Degree of anisotropy, contour interval, 0.1, light shading < 0.3, dark shading > 0.3

7.2.1 Tip Leakage Jet Region

The tip leakage jet flows through the tip gap along the endwall. On Figures 46 - 48, this region consists of the set of glyphs on the bottom two rows, each extending four across, beginning with the column closest to the tip gap. From these figures, it can be seen that the glyphs in this region are relatively small, indicating a relatively low level of turbulence kinetic energy. For clarity, therefore, the three sets of these eight glyphs were enlarged and are presented together on Figure 51. On this figure, the glyphs are shown in the same view as the glyphs given in Figures 46 - 48.

Consider first, the orientation of the glyphs for the measured Reynolds stress tensors. Along the bottom row, as the jet emerges from the tip gap and moves along the endwall, the glyphs are aligned so that the major principal axis is oriented in the y-z plane, and the middle principal axis is roughly parallel to the x-axis, pointing out of the page. The orientation of these glyphs resemble the orientation of the glyphs measured in fully developed pipe flow. This suggests that the jet flow close to the endwall acts essentially like a boundary layer, where the dominating shear stress has components in the direction of the flow and perpendicular to the wall.

In the top row of glyphs of the measured data, the major principal direction has a pronounced x-component. This indicates the influence of Reynolds stresses oriented in the direction of the free stream flow.

By comparison, the glyphs of the Boussinesq approximation are all generally oriented so that the major principal direction is primarily in the y-z plane, but does have a

small x -component. The rotation of the top row of glyphs to the freestream flow direction is not given by the Boussinesq approximation.

Likewise, the ARSM glyphs are also generally oriented with the major principal direction in the y-z plane. These glyphs are more closely aligned with the glyphs of the Boussinesq approximation than the measured data.

Quantitatively, the relative orientations of the glyphs are shown in Figure 49. On these plots, the tip leakage jet region extends from the endwall to the height of the tip gap, from $y / \Delta y' = 0$ to $y / \Delta y' = 0.35$. In this region, the orientation angles between the Boussinesq approximation and measured stress tensor glyphs are in the range of 20 to 30 degrees. Similar angles occur between the ARSM and the measured data glyphs. The orientation angles between the ARSM and the Boussinesq approximation, on the other hand, are under 10 degrees throughout the tip leakage jet region.

Now consider the shapes of the glyphs in the tip leakage jet region. From the measurements, the glyphs along the bottom row appear peanut-shaped, indicating three distinct principal stress values. In the top row, the glyphs are more rounded and egg-shaped. These tensors, therefore, are more isotropic and have closer middle and minor principal stress values.

The glyphs for the Boussinesq approximation are also more rounded and isotropic in the top row when compared to the bottom row. Compared to the measured data, however, the Boussinesq approximation produces glyphs that all appear more rounded. This means that while the Boussinesq approximation successively predicts the trends for

isotropy in the tip leakage jet region, it generally yields a more isotropic stress tensor than the experimental measurements show.

The glyphs for the ARSM again show the tensor becoming more isotropic moving away from the endwall. These glyphs are also generally more isotropic than the measured stress tensor glyphs, but slightly less isotropic than the Boussinesq approximation glyphs.

Figure 50 shows quantitatively, the anisotropy of the three sets of Reynolds stress tensors. On each plot, increasing degrees of anisotropy can be seen in the tip leakage jet region as the endwall is approached. Just as the tensor glyph pictures indicate, Figure 50 shows the measured Reynolds stress tensor having the highest degree of anisotropy. These tensors have anisotropy values of about 0.3 in the portion of jet region furthest away from the endwall, and values over 0.6 in the area close to the endwall. The ARSM tensors also have anisotropy values of about 0.3 in the area away from the endwall. Values close to the endwall, however, only reach the 0.5 to 0.6 range. The Boussinesq approximation tensors have anisotropy values similar to the ARSM.

Fig. 51 Glyphs for the Tip Leakage Jet

7.3.2 The Endwall Separation Region

In the endwall separation region, the flow moving from the tip gap along the endwall separates from the wall and begins to circulate in a vortex flow pattern. On the glyph pictures presented in Figures 46 - 48, the endwall separation region consists of the eight largest glyphs shown in columns eight and nine, extending four rows up, beginning at the bottom of the figure. Again, for a clearer presentation, these sets of glyphs from Figures 46 - 48 were enlarged and are shown together in Figure 52. On the orientation angles and anisotropy contour plots, the endwall separation region extends from $y / \Delta y' = 0.5$ to $y / \Delta y' = 0.55$, and from the bottom of the plot to $z / \Delta z = 0.05$.

As the tip leakage jet flows along the endwall and begins to mix with the passage flow that moves between the two turbine blades, the interaction produces endwall separation, starting at about $y / \Delta y' = 0.5$. This complex flow pattern results in a region of high turbulence intensity. This is shown on Figure 46 by the relatively large glyphs in this area.

From the glyphs for the measured data shown in Figure 52, it can be seen that the combination of Reynolds stresses in this region produces nearly uniform orientation of the major principal axes, each having a large y-component, and smaller, nearly equal, x and z components.

The glyphs for the Boussinesq approximation stress tensors are also oriented with the major principal axes having large y-components. These glyphs, however, are not as uniformly aligned with each other as the glyphs for the measured data. The bottom four

Boussinesq approximation glyphs have major principal axes with almost no z-component, while the top four are rotated more in the z direction. Also, the middle and minor principal axes of the bottom four Boussinesq approximation glyphs are positioned similarly to the measured stress tensor glyphs, while the top four glyphs have poor alignment of the middle and minor principal stress directions.

The ARSM glyphs are oriented in a similar fashion as the Boussinesq glyphs. This can be seen with visual comparisons of the glyphs on Figure 52, and by studying the orientation angle plots of Figure 49. On Figure 49, the orientation angles between the Boussinesq approximation and the measured data glyphs and between the ARSM and Boussinesq approximation glyphs are mostly between 10 and 30 degrees in the endwall separation region. The Boussinesq approximation and ARSM glyphs, on the other hand, are generally oriented to within 10 degrees in this region.

For the measured Reynolds stress tensors in the endwall separation region, Figure 52 shows that the larger glyphs are highly elongated in the major principal direction, and have a narrow neck in the plane formed by the middle and minor principal axes. This corresponds physically to a highly anisotropic stress tensor with a middle principal value close to the minor principal value. The smaller glyphs in the first column in the top two rows are more rounded, and, therefore, more isotropic.

The glyphs for the Boussinesq approximation, on the other hand, are generally shown to be more isotropic than their counterparts in the measured data. The major principal stress appears slightly smaller for these glyphs, and the middle principal stress

looks to have relatively higher values than the measured stress tensors. This latter fact is indicated by the coloring scheme of the glyphs. Where the measured data glyphs are generally shaded blue in the middle principal direction, the Boussinesq approximation glyphs are more often shaded green.

The ARSM glyphs, for the most part, seem to be shaped similarly to the measured data glyphs. Some glyphs, particularly the ones in the first column, do appear more isotropic that their measured data counterparts, but the differences are slight. A noteworthy ARSM glyph is given in the second column, third row. Here, the ARSM glyph is noticeably more anisotropic than its counterpart in the measurements. In fact, this glyph appears to have the highest degree of anisotropy of any considered thus far.

Figure 50 shows the quantified anisotropy measures of the three glyph sets in the endwall separation region. On this figure, the measured stress tensors have anisotropy values that are, for the most part, above 0.9. In the area where the top two glyphs in the first column appear in Figure 52, the anisotropy values are shown to be in the range of 0.6 to 0.9. The anisotropy values for the Boussinesq approximation tensors are lower than the measured stress tensors. Values between 0.6 and 0.9 appear over most of the endwall separation region. In the top right hand corner of the region, values climb over 0.9. The ARSM stress tensors also have slightly lower anisotropy values when compared to the measured data, particularly in the area of the first column of glyphs. Here, values in the range of 0.6 to 0.9 are found. Values in the area of the second column of glyphs, however, generally climb over 0.9, like the measured data. The highly anisotropic ARSM glyph

appears in this region on the contour plot with an anisotropy value of 1.3. This is the highest anisotropy value found on any of the three contour plots.

Fig. 52 Glyphs for the Endwall Separation Region

7.3.3 Flow Convected Above the Vortex Core

The last region to be considered is the flow convected above the tip leakage vortex core. On Figures 46 - 48, the region is represented by the first five glyphs in rows six and seven. Enlarged glyphs for this region are shown in Figure 53. On the contour plots given in Figures 49 and 50, this region extends from $y / \Delta y' = 0$ to $y / \Delta y' = 0.35$, and from $z / \Delta z = 0.08$ to $z / \Delta z = 0.12$.

Looking first to the mean flow velocity components in Figure 38, it can be seen that in this region, the flow is moving in a vortex towards the turbine blade suction side. Careful comparison of Figure 38, the glyph pictures of the entire cascade measurement plane, and the enlarged glyphs shown in Figure 53 show that the glyphs in the bottom row on Figure 53 are in a region moving around the tip leakage vortex, while the glyphs in the top row of Figure 53 are positioned in an area between the tip leakage vortex and the passage vortex.

The measured data glyphs in Figure 53 can easily be divided into three groups: the four glyphs in the two rows on the left side of the region, the remaining three glyphs in the bottom row, and the remaining three glyphs in the top row.

The four glyphs on the left side of the convected flow region are associated with flow in direct proximity of the turbine blade suction side. The presence of the blade apparently produces relatively large normal Reynolds stress components perpendicular to its surface, in the y direction. This is shown on the glyphs by the orientation of the major principal axis in the y direction. The middle and minor principal stresses, which are

oriented in the x and z directions, respectively, have smaller values. This is shown by the elongated shape of the glyph. A moderately anisotropic stress tensor is, therefore, indicated.

The remaining three glyphs in the bottom row correspond to flow circulating directly above the tip leakage vortex core. Here, the glyph orientations are almost identical, with the major principal axis having a small x-component and roughly forming a 45 degree angle in the y-z plane. These glyphs are egg-shaped, indicated a moderately anisotropic tensor with comparable middle and minor principal stress values.

The last three glyphs in the top row are associated with the flow moving between the tip leakage and passage vortices. These glyphs are also oriented in a fairly uniform fashion, with the major principal direction having a large z-component and smaller x and y components. The left-most glyph in this group is disk-shaped, while the glyphs to its right become more egg-shaped. This shows the growing dominance of the major principal stress, oriented in the z direction, moving left to right in this group of glyphs.

By comparison, in this region, the Boussinesq approximation and the ARSM produce glyphs that are remarkably similar to one another. Both models reproduce the group of the four left-most glyphs reasonably well, with these glyphs being egg-shaped and having the major principal stresses oriented in the y direction, just as the measurements indicate. The model glyphs in the remaining two groups, however, do not compare well with the measured stress tensor glyphs. In the third column, where the measurements produce glyphs that look similar to adjacent glyphs in their respective

rows, the two models produce glyphs that do not fit into any group. In addition, in this column neither model produces glyphs that resemble the measurement glyphs. In the bottom row, third column, both models produce glyphs that are disk-shaped, instead of egg-shaped like the measured stress tensor glyphs. In the top row, third column, the orientations of both modeled glyphs are in significant error. For the remaining two glyphs in the bottom row, both models have glyphs that are oriented the wrong way, and are much more isotropic that the measured stress tensors. In fact, in both models, the last glyph in the bottom row is nearly spherical, meaning that the two models predict a state of nearly isotropic stress in this area. Finally, the last two glyphs in the top row are also similar in both models. The two models both produce glyphs that show the normal stresses in the z direction having lesser relative importance than the measured stress tensor glyphs indicate. In both models, the major principal axes do not have as large a z-component as in the measurements. Also, the modeled glyphs are more disk-shaped then egg-shaped, indicating a larger relative middle principal stress.

The similarities between the Boussinesq approximation and ARSM predictions, and the differences the two models have with the actual measurements, is again shown on the orientation angle and the anisotropy contour plots. On the orientation angle plots, in convected flow region near the blade suction surface, both model glyphs are oriented at 10 to 30 degree angles relative to the measured stress tensor glyphs. In the region further from the blade, the orientation errors in the models reach as high as 50 degrees. On the other hand, the orientation differences between the two models never exceed 20 degrees.

Similarly, on the anisotropy measure plots, the anisotropy values of the two models are nearly the same in the convected flow region. Close to the blade surface, anisotropy values for both models range from 0.3 to 0.5. Away from the blade surface, values fall below 0.3. with the point of the spherical glyph having an anisotropy value of below 0.1. The measured data, on the other hand, shows more consistent values for the degree of anisotropy. From the measurements in this region, values in the range of 0.4 to 0.6 were found.

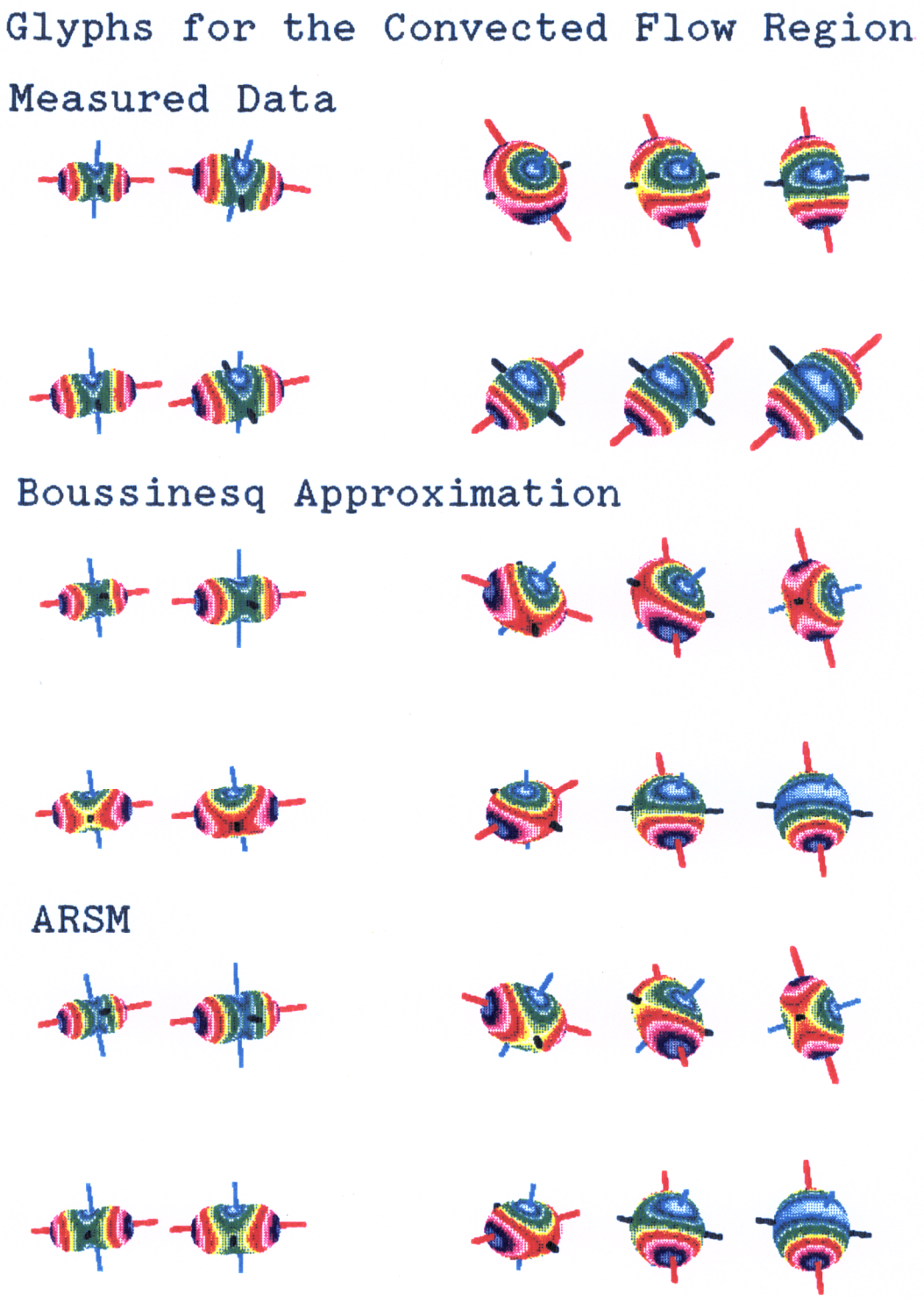

Fig. 53 Glyphs for the Flow Convected Above the Vortex Core

7.3.4 Overall Model Performance

Aside from the tensor glyph pictures, the contour plots of the orientation angles and the degrees of anisotropy can be used to help evaluate the ARSM and the Boussinesq approximation over the entire cascade measurement plane. Throughout most of the measurement plane, both models have orientation errors that are less than 30 degrees. For the most part, the two models are oriented quite well with each other, generally to within 20 degrees. The only area in which the two models show a discrepancy in their orientation is at the top of the plot, where the turbulence is relatively low. Here, the two models differ in orientation by as much as 60 degrees. This is also the area where the two models are in the greatest error when compared to the data, with both having orientation errors over 80 degrees.

Throughout the anisotropy plots, the two models both show more isotropic stress tensors than the measurements. For the experimental data, over nearly all the measurement plane, the degree of anisotropy was over 0.3, with a small area in the vicinity of the tip leakage vortex core having anisotropy values under 0.2. Higher anisotropy values were found along the endwall and in the separation area, where peak values over 1.1 are shown. Both models, on the other hand, have substantial regions where the anisotropy values are under 0.3. Peak values for the two models also occur in the endwall separation region. Here, the ARSM shows a peak value of 1.3, while the Boussinesq approximation has a maximum value slightly over 1.0.

8.0 Conclusions

The tensor glyph provides another way of presenting the Reynolds stress tensor throughout a turbulent flowfield. By representing the entire tensor, it yields information not given by plots of individual stress components. The glyph also has the advantage of being independent of any coordinate system, since it represents all the tensor components at once. This property is useful in complex flow geometries, where flow boundaries do not obviously define a proper coordinate system for presenting the Reynolds stresses. However, the Reynolds stress component plots do have the advantage of clearly indicating turbulence momentum transfer in a specified direction. Since this information is usually of interest to the engineer, the tensor glyph is most effectively used in conjunction with the stress component plots. In this way, a more complete understanding of the state of turbulence stress will be gained.

The glyph that was constructed and used throughout this thesis provided a clearer representation of more tensor information than any glyph type found in the literature. This was done by constructing the glyph to a) give normal stress components in every coordinate system orientation, b) directly correspond to tensor component values, and c) clearly indicate the principal directions. In addition, these glyphs are easily used in conjunction with Mohr's circles to supply information about shear stress components in planes formed by two principal directions. In one of these planes, the maximum possible shear stress value is found.

Tensor properties, such as the degree of anisotropy and the orientation of principal directions, are shown by the tensor glyph in a qualitative way. To complement this qualitative representation, these properties can be quantitatively defined and plotted. In this thesis, anisotropy is defined as the difference between the maximum and minimum principal stresses, divided by the turbulence kinetic energy. These quantitative plots reduce the amount of information given by the glyph to provide a more concise summary.

8.1 Fully Developed Pipe Flow

In fully developed pipe flow, both the tensor glyph pictures and the Reynolds stress component plots indicate that Rodi's Algebraic Reynolds Stress Model (ARSM) [9] provides an improvement over the Boussinesq approximation in modeling the Reynolds stress tensor. This conclusion, however, is reached differently with both presentation methods. From the Reynolds stress component plots, it can be seen that the ARSM clearly predicts the $\overline{uu}$ and $\overline{vv}$ stress components better that the Boussinesq approximation, while the Boussinesq approximation is slightly better in predicting the $\overline{ww}$ stress. The glyphs, on the other hand, show that the ARSM gives a clear improvement in predicting the orientation of the principal directions. In fact, the orientation of principal directions indicates a fundamental break-down of the Boussinesq approximation in modeling fully developed pipe flow. This is because the Boussinesq approximation predicts that the major principal direction must be 45 degrees to the flow. The measurements, on the other hand, indicate that the major principal direction varies

with the radial position, and is oriented between 15 and 35 degrees to the flow. In addition, the glyphs show that the ARSM provides a slight improvement in predicting the degree of anisotropy. Both models, however, yield more isotropic stress tensors that Laufer's measurements show.

Two methods used in calculating the rate of turbulence dissipation, one based upon the Kolmogorov-Prandtl expression and one based upon the ARSM, gave similar results in the fully developed pipe flow. At both Reynolds numbers considered, the calculated distributions of the dissipation values were similar, to within a constant factor. By comparing the ARSM calculations to the known distribution of the dissipation values, the ARSM constants could be evaluated for fully developed pipe flow. It was found that using $C_1 = 2.8$ and $\gamma = 0.6$ worked suitably well for this flow geometry.

8.2 Tip Leakage Vortex

In the tip leakage vortex flow of a turbine cascade, the ARSM and the Boussinesq approximation yielded remarkably similar results. This is seen in the Reynolds stress component plots, where the two models yielded very similar $\overline{uu}$, $\overline{vv}$, $\overline{ww}$, and $\overline{vw}$ results, and in the glyph pictures, where the corresponding model glyphs usually resembled one another in each region considered. These results suggest that any significant difference between the two models in calculating Reynolds stresses must come from externally supplied scalar quantities, such as ν_t, ε, or the model constants.

Reformulating the model equations so that these values could be replaced with the same experimental data results in a similar representation of the Reynolds stress tensor.

Calculating the orientation of the principal directions and the degree of anisotropy provided two additional ways of describing the Reynolds stress tensor and evaluating turbulence models. Over almost all of the measurement region in the tip leakage turbine cascade, the major principal directions of the two models were oriented within 20 degrees of each other. Over roughly 60% of the measurement region, the major principal directions of the two models were oriented within 30 degrees of the data. Also, both models generally predicted a lower degree of anisotropy than the measurements indicate. Where the data showed anisotropy values of between 0.3 and 0.6 over most of the measurement region, both models had substantial areas of values under 0.3. The highest degree of anisotropy was found in the endwall separation region. Here, the data showed a peak value over 1.1, the ARSM peaked at over 1.3, and the Boussinesq approximation had a maximum value just over 1.0.

Appendix A: Derivation of the Algebraic Reynolds Stress Model

The derivation of the Algebraic Reynolds Stress Model (ARSM) as presented by Rodi [9] is given here. Recall that the modeled Reynolds stress transport equations, Equation (12), given by Hanjalic and Launder [8] are in the form:

$$\frac{D\overline{u_i u_j}}{Dt} = P_{ij} - \frac{2}{3}\delta_{ij}\varepsilon + \left(\phi_{ij} + \phi_{ji}\right)_1 + \left(\phi_{ij} + \phi_{ji}\right)_2 + D_{ij} \qquad (A.1)$$

where D_{ij} is the modeled Reynolds stress diffusion term:

$$D_{ij} = C_s \frac{\partial}{\partial x_k}\frac{k}{\varepsilon}\left[\overline{u_i u_l}\frac{\partial\overline{u_j u_k}}{\partial x_l} + \overline{u_j u_l}\frac{\partial\overline{u_k u_i}}{\partial x_l} + \overline{u_k u_l}\frac{\partial\overline{u_i u_j}}{\partial x_l}\right] \qquad (A.2)$$

Rodi used a simplified expression for this term. It appears as:

$$D_{ij} = C_s \frac{\partial}{\partial x_k}\left(\frac{k}{\varepsilon}\overline{u_k u_l}\frac{\partial\overline{u_i u_j}}{\partial x_l}\right) \qquad (A.3)$$

The transport equation for the turbulence kinetic energy can be given in a similar form:

$$\frac{Dk}{Dt} = D_k - P - \varepsilon . \tag{A.4}$$

Here, D_k is the diffusion of turbulence kinetic energy. If the turbulence kinetic energy equation is derived by taking half the sum of the three normal Reynolds stress transport equations, D_k takes the form:

$$D_k = C_s \frac{\partial}{\partial x_k}\left(\frac{k}{\varepsilon}\overline{u_k u_l}\frac{\partial k}{\partial x_l}\right). \tag{A.5}$$

To simplify the set of differential Reynolds stress equations, it is desirable to approximate them with a set of algebraic expressions. To do this, the differential convective and diffusion terms in the Reynolds stress equations must be replaced with algebraic approximations. Rodi proposed the approximation

$$\frac{D\overline{u_i u_j}}{Dt} - D_{ij} \cong \frac{\overline{u_i u_j}}{k}\left(\frac{Dk}{Dt} - D_k\right) = \frac{\overline{u_i u_j}}{k}(P - \varepsilon). \tag{A.6}$$

This approximation can be more fully understood by expanding the convective and diffusion Reynolds stress terms in the following way:

$$\frac{D\overline{u_i u_j}}{Dt} = \frac{\overline{u_i u_j}}{k}\frac{Dk}{Dt} + k\frac{D\,\overline{u_i u_j}/k}{Dt}, \qquad (A.7)$$

$$D_{ij} = \frac{\overline{u_i u_j}}{k}D_k + C_s\frac{\partial}{\partial x_k}\left(\frac{k^2}{\varepsilon}\overline{u_k u_l}\frac{\partial\,\overline{u_i u_j}/k}{\partial x_l}\right) + \frac{k}{\varepsilon}C_s\overline{u_k u_l}\frac{\partial k}{\partial x_l}\frac{\partial\,\overline{u_i u_i}/k}{\partial x_k}. \qquad (A.8)$$

From Equations (A.7) and (A.8) it is clear that the approximation in Equation (A.6) is exactly true if the terms containing gradients of $\overline{u_i u_j}/k$ are equal to zero and approximately true if the gradients of $\overline{u_i u_j}/k$ are small.

If the approximation given in Equation (A.6) is used in the Reynolds stress transport equations, Equation (A.1), along with the pressure strain models given in Equations (12.a) and (12.c), there results:

$$\frac{D\overline{u_i u_j}}{Dt} - D_{ij} = \frac{\overline{u_i u_j}}{k}(P-\varepsilon) = P_{ij} - C_1\frac{\varepsilon}{k}\left(\overline{u_i u_j} - \delta_{ij}\frac{2}{3}k\right) - \gamma\left(P_{ij} - \frac{2}{3}P\delta_{ij}\right) - \frac{2}{3}\delta_{ij}\varepsilon \qquad (A.9)$$

Solving for $\overline{u_i u_j}$ gives the algebraic expression for the Reynolds stresses as:

$$\overline{u_i u_j} = k\left[\frac{2}{3}\delta_{ij} + \frac{(1-\gamma)\left(P_{ij} - \frac{2}{3}P\delta_{ij}\right)}{\varepsilon(C_1 - 1) + P}\right]. \qquad (A.10)$$

Appendix B: Computation Method for Calculating Principal Values and Directions

A subroutine based upon Jacobian transformations of a symmetric matrix was presented in Numerical Recipes in FORTRAN [15] and was used to determine principal values and directions of the Reynolds stress tensor. The subroutine is an efficient numerical approach to solving a more generalized eigenvalue/eigenvector problem in which the Reynolds stress tensor qualifies as a subclass. The method presented here works for a real, symmetric matrix of any size.

Essentially, the subroutine utilizes a proven relation in linear algebra:

$$X_R^{-1} \bullet A \bullet X_R = \mathrm{diag}(\lambda_1, \lambda_2, ..., \lambda_N), \qquad \text{(B.1)}$$

in which A is the matrix being considered, N is the size of the matrix, X_R is a matrix whose columns store the components of each eigenvector, and X_R^{-1} is the inverse of X_R. The eigenvalues are stored in a diagonal matrix shown on the right hand side of Equation (B.1). When this subroutine is applied in this thesis, the A matrix is the Reynolds stress tensor and eigenvectors and eigenvalues are its principal directions and values, respectively. The subroutine utilizes the above relation by multiplying the A matrix by a series of plane transformation matrices, P, shown as:

$$P = \begin{bmatrix} 1 & 0 & 0 & 0 & 0 \\ 0 & c & 0 & s & 0 \\ 0 & 0 & 1 & 0 & 0 \\ 0 & -s & 0 & c & 0 \\ 0 & 0 & 0 & 0 & 1 \end{bmatrix}. \qquad \text{(B.2)}$$

Here, the c and s represent the cosine and sine of the angle of the plane rotation. Each plane rotation is designed to create a zero in one of the off-diagonal elements. Successive transformations are applied so that:

$$A \rightarrow P_1^{-1} \bullet A \bullet P_1 \rightarrow P_2^{-1} \bullet P_1^{-1} \bullet A \bullet P_1 \bullet P_2 \rightarrow .... \qquad \text{(B.3)}$$

The matrix containing the eigenvalues then becomes:

$$X_R = P_1 \bullet P_2 \bullet P_3 \bullet .... \; . \qquad \text{(B.3)}$$

In this way, the plane transformation matrices build to form the eigenvector matrix X_R. Successive transformations undo previously set zeroes, but the off-diagonal elements nevertheless continue to get smaller, until the matrix is diagonal to within machine precision. Once the plane transformation matrices successfully create zeros for all the off-diagonal elements in A, the resulting diagonal matrix stores the eigenvalues and X_R stores the eigenvectors.

Appendix C: A New Glyph Construction Method

To construct the glyph utilized in this thesis from a Reynolds stress tensor, the equation governing the transformation of normal stress components, Equation (19), was used. Using this expression, a set of normal stress values in three spatial dimensions were calculated. This was done in a FORTRAN subroutine given below, but the process can be explained with the consideration of Figure C.1. Here a cubic shell, whose faces are discretely broken up into n by n grid points, is shown surrounding a point P in space. In the FORTRAN subroutine, directions of unit vectors are defined from P to every point on the cubic shell. This vector is used in Equation (19) in conjunction with a Reynolds stress tensor defined in the x,y,z coordinate system to calculate a normal stress magnitude. These normal stresses, shown as $\overline{u_n^2}$ on Figure C.1, are multiplied by the unit vector components to create new vectors used in the construction of the glyph. Constructing these vectors for all the points on the cubic shell completely defines the glyph geometry. After all the glyph vector magnitudes and directions are determined, a data file is created in which the coordinates of four adjacent vector tips and a color are stored. These four coordinate points form a polygon in space which is colored according to a scheme described below. Another program named ZDRAW is then used to image all the polygons in the data file. The result is the glyph used described in Section 4.3.

As the magnitudes and directions of the glyph vectors are calculated, the largest and smallest stress values are noted. These correspond to the major and minor principal

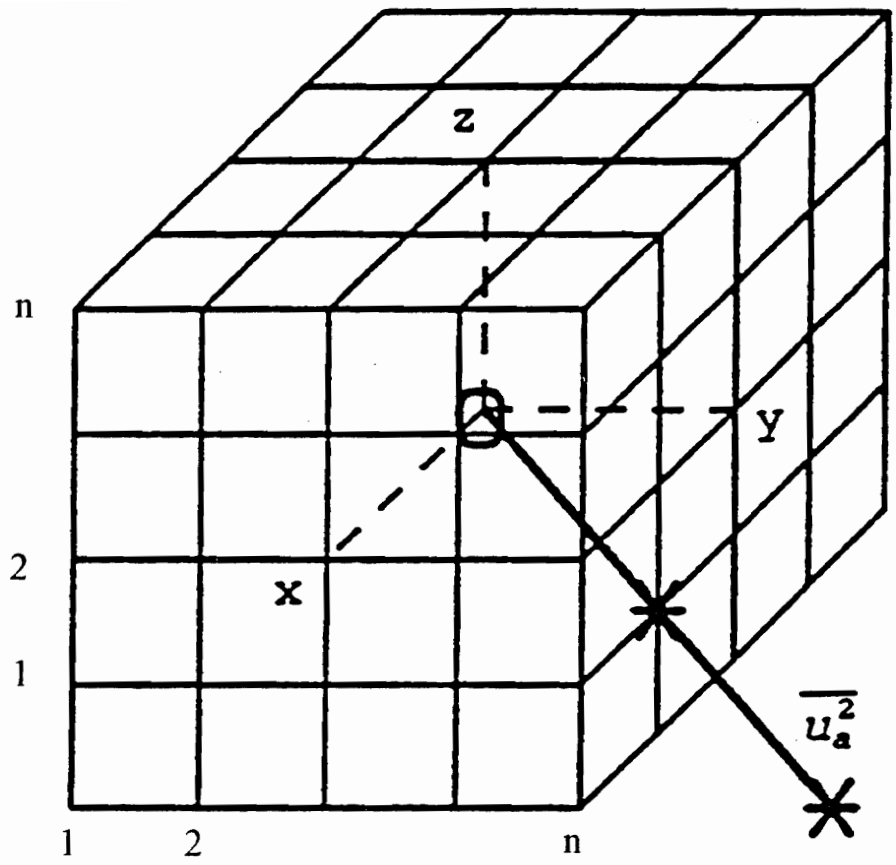

Fig. C.1 A Cubic Shell Used in the Normal Stress Component Calculations for the Glyph Construction

stresses and directions. Protruding glyph axes are constructed in these directions and in the direction normal to both. In this way, the principal directions are indicated on the glyph.

The coloring scheme for the glyph was developed according to the values of the major and minor principal stresses. Forty colors were used for the glyph, each one assigned to a range of normal stress values equal to $1/40*(\mathrm{P\,max} - \mathrm{P\,min})$. This scheme helps to emphasize the variation of normal stress values in differing directions.

The following is a FORTRAN subroutine used in creating the glyph.

```
      program tform
c*****************************************************************
c This program determines the normal Reynolds stress
c in any direction through the transformation of the
c 3-D Reynolds stress tensor. It also produces a file, poly.data,
c  that can be used to image one or more stress tensors.
c The imaging is used through the program ZDRAW.
c*****************************************************************

      real t,nstress,a,b,c,at,bt,ct,mt,scle,scl2,tk,lnmed,magmed
      common t(3,3),nstress(100,100,100),x(100,100,100),y(100,100,100),
     *       z(100,100,100)

      open(1,file='poly.data')

c input the Reynolds stress tensor

      t(1,1) = 121
      t(2,2) = 89
      t(3,3) = 104
      t(1,2) = -8
      t(1,3) = -13
      t(2,3) = 26
      t(2,1) = t(1,2)
      t(3,1) = t(1,3)
      t(3,2) = t(2,3)

c calculate the normal stress in all directions

      a = -1.
      b = -1.
      c = -1.
      stmax=0.
      stmin=10000000
      do 10, i=1,11
         b = -1
         do 20, j=1,11
            c = -1
            do 30, k=1,11

c stretch position vector to insure that its length = 1

               mt = sqrt(1/(a*a+b*b+c*c))
               at = a*mt
               bt = b*mt
               ct = c*mt

c nstress is the value of the normal stress in the direction of
c the vector at,bt,ct

               nstress(i,j,k)=t(1,1)*at*at+t(2,2)*bt*bt+t(3,3)*
     *          ct*ct+2*at*bt*t(1,2)+2*at*ct*t(1,3)+2*bt*ct*t(2,3)

c x,y,z are the components of the normal stress vector
```

```
                x(i,j,k)=nstress(i,j,k)*at
                y(i,j,k)=nstress(i,j,k)*bt
                z(i,j,k)=nstress(i,j,k)*ct

c determine the max/min stresses and the stress directions

                stmax1=amax1(stmax,nstress(i,j,k))
                stmin1=amin1(stmin,nstress(i,j,k))
                if (stmax1.ne.stmax) then
                   xmax = at*nstress(i,j,k)
                   ymax = bt*nstress(i,j,k)
                   zmax = ct*nstress(i,j,k)
                endif
                if (stmin1.ne.stmin) then
                   xmin = at*nstress(i,j,k)
                   ymin = bt*nstress(i,j,k)
                   zmin = ct*nstress(i,j,k)
                endif
                stmax = stmax1
                stmin = stmin1
                c = c + .2
 30           continue
                b = b + .2
 20        continue
                a = a + .2
 10    continue

c assign a color according to the average length of 4 adjacent
c normal stress vectors, repeat for all six sides of a cube to
c obtain a 3-d object to be plotted

       do 40 i=1,11,10
       do 40 j=1,10
       do 40 k=1,10
       stb=.25*(nstress(i,j,k)+nstress(i,j+1,k)+nstress(i,j,k+1)
      *        +nstress(i,j+1,k+1))
       ic=11+39*(stb-stmin)/(stmax-stmin)
       write (1,*) 'c',ic
       write (1,*) 'p',x(i,j,k),y(i,j,k),z(i,j,k),
      *                x(i,j+1,k),y(i,j+1,k),z(i,j+1,k),
      *                x(i,j+1,k+1),y(i,j+1,k+1),z(i,j+1,k+1),
      *                x(i,j,k+1),y(i,j,k+1),z(i,j,k+1)
 40    continue
       do 41 j=1,11,10
       do 41 i=1,10
       do 41 k=1,10
       stb=.25*(nstress(i,j,k)+nstress(i+1,j,k)+nstress(i,j,k+1)
      *        +nstress(i+1,j,k+1))
       ic=11+39*(stb-stmin)/(stmax-stmin)
       write (1,*) 'c',ic
       write (1,*) 'p',x(i,j,k),y(i,j,k),z(i,j,k),
      *                x(i+1,j,k),y(i+1,j,k),z(i+1,j,k),
      *                x(i+1,j,k+1),y(i+1,j,k+1),z(i+1,j,k+1),
      *                x(i,j,k+1),y(i,j,k+1),z(i,j,k+1)
 41    continue
       do 42 k=1,11,10
       do 42 i=1,10
       do 42 j=1,10
       stb=.25*(nstress(i,j,k)+nstress(i+1,j,k)+nstress(i,j+1,k)
      *        +nstress(i+1,j+1,k))
       ic=11+39*(stb-stmin)/(stmax-stmin)
```

```
      write (1,*) 'c',ic
      write (1,*) 'p',x(i,j,k),y(i,j,k),z(i,j,k),
     *                x(i+1,j,k),y(i+1,j,k),z(i+1,j,k),
     *                x(i+1,j+1,k),y(i+1,j+1,k),z(i+1,j+1,k),
     *                x(i,j+1,k),y(i,j+1,k),z(i,j+1,k)
 42   continue

c plot axes for the glyph, the axes will be in the directions of the
c max and min normal stresses and the direction orthogonal to the
c max/min stresses
c find the orthogonal direction, take the cross product

      xmed = ymax*zmin - ymin*zmax
      ymed = zmax*xmin - zmin*xmax
      zmed = xmax*ymin - xmin*ymax

c make the medium axis a unit vector then adjust its length as the
c average of the minimum and maximum lengths

      magmed = sqrt(xmed*xmed+ymed*ymed+zmed*zmed)
      lnmed = .5*(stmax+stmin)
      xmed = (xmed/magmed)*lnmed
      ymed = (ymed/magmed)*lnmed
      zmed = (zmed/magmed)*lnmed

c construct axes for each glyph. scale the length of the axis
c by scle. the axis thickness is given as tk.

      scle = 1.5
      scl2 = 2.5
      tk = 3

      write (1,*) 'c',2
      write (1,*) 'p',-scle*xmax,dy-scle*ymax,dz-scle*zmax,
     *                scle*xmax,dy+scle*ymax,dz+scle*zmax,
     *                scle*xmax,tk+dy+scle*ymax,dz+scle*zmax,
     *                -scle*xmax,tk+dy-scle*ymax,dz-scle*zmax
      write (1,*) 'c',2
      write (1,*) 'p',-scle*xmax,dy-scle*ymax,dz-scle*zmax,
     *                scle*xmax,dy+scle*ymax,dz+scle*zmax,
     *                scle*xmax,dy+scle*ymax,tk+dz+scle*zmax,
     *                -scle*xmax,dy-scle*ymax,tk+dz-scle*zmax
      write (1,*) 'c',2
      write (1,*) 'p',-scle*xmax,dy-scle*ymax,tk+dz-scle*zmax,
     *                scle*xmax,dy+scle*ymax,tk+dz+scle*zmax,
     *                scle*xmax,tk+dy+scle*ymax,tk+dz+scle*zmax,
     *                -scle*xmax,tk+dy-scle*ymax,tk+dz-scle*zmax
      write (1,*) 'c',2
      write (1,*) 'p',-scle*xmax,tk+dy-scle*ymax,dz-scle*zmax,
     *                scle*xmax,tk+dy+scle*ymax,dz+scle*zmax,
     *                scle*xmax,tk+dy+scle*ymax,tk+dz+scle*zmax,
     *                -scle*xmax,tk+dy-scle*ymax,tk+dz-scle*zmax
      write (1,*) 'c',5
      write (1,*) 'p',-scl2*xmin,dy-scl2*ymin,dz-scl2*zmin,
     *                scl2*xmin,dy+scl2*ymin,dz+scl2*zmin,
     *                scl2*xmin,tk+dy+scl2*ymin,dz+scl2*zmin,
     *                -scl2*xmin,tk+dy-scl2*ymin,dz-scl2*zmin
      write (1,*) 'c',5
      write (1,*) 'p',-scl2*xmin,dy-scl2*ymin,dz-scl2*zmin,
     *                scl2*xmin,dy+scl2*ymin,dz+scl2*zmin,
     *                scl2*xmin,dy+scl2*ymin,tk+dz+scl2*zmin,
```

```
*                  -scl2*xmin,dy-scl2*ymin,tk+dz-scl2*zmin
 write (1,*) 'c',5
 write (1,*) 'p',-scl2*xmin,dy-scl2*ymin,tk+dz-scl2*zmin,
*                  scl2*xmin,dy+scl2*ymin,tk+dz+scl2*zmin,
*                  scl2*xmin,tk+dy+scl2*ymin,tk+dz+scl2*zmin,
*                  -scl2*xmin,tk+dy-scl2*ymin,tk+dz-scl2*zmin
 write (1,*) 'c',5
 write (1,*) 'p',-scl2*xmin,tk+dy-scl2*ymin,dz-scl2*zmin,
*                  scl2*xmin,tk+dy+scl2*ymin,dz+scl2*zmin,
*                  scl2*xmin,tk+dy+scl2*ymin,tk+dz+scl2*zmin,
*                  -scl2*xmin,tk+dy-scl2*ymin,tk+dz-scl2*zmin
 write (1,*) 'c',1
 write (1,*) 'p',-scle*xmed,dy-scle*ymed,dz-scle*zmed,
*                  scle*xmed,dy+scle*ymed,dz+scle*zmed,
*                  scle*xmed,tk+dy+scle*ymed,dz+scle*zmed,
*                  -scle*xmed,tk+dy-scle*ymed,dz-scle*zmed
 write (1,*) 'c',1
 write (1,*) 'p',-scle*xmed,dy-scle*ymed,dz-scle*zmed,
*                  scle*xmed,dy+scle*ymed,dz+scle*zmed,
*                  scle*xmed,dy+scle*ymed,tk+dz+scle*zmed,
*                  -scle*xmed,dy-scle*ymed,tk+dz-scle*zmed
 write (1,*) 'c',1
 write (1,*) 'p',-scle*xmed,tk+dy-scle*ymed,dz-scle*zmed,
*                  scle*xmed,tk+dy+scle*ymed,dz+scle*zmed,
*                  scle*xmed,tk+dy+scle*ymed,tk+dz+scle*zmed,
*                  -scle*xmed,tk+dy-scle*ymed,tk+dz-scle*zmed
 write (1,*) 'c',1
 write (1,*) 'p',-scle*xmed,dy-scle*ymed,tk+dz-scle*zmed,
*                  scle*xmed,dy+scle*ymed,tk+dz+scle*zmed,
*                  scle*xmed,tk+dy+scle*ymed,tk+dz+scle*zmed,
*                  -scle*xmed,tk+dy-scle*ymed,tk+dz-scle*zmed


 stop
 end
```

Appendix D: Boussinesq Approximation and ARSM Equations for Reynolds Stresses in Fully Developed Pipe Flow

In tensor notation, where x_1 refers to the axial direction, x_2 is the radial direction, and x_3 is the circumferential direction, the simplifications of fully developed turbulent pipe flow are:

(1) $U_2 = 0$ and $U_3 = 0$

(2) $\dfrac{\partial}{\partial x_3} = 0$

(3) the velocity field is independent of x_1.

Because of these restrictions, the only non-zero velocity gradient is $\partial U_1/\partial x_2$. This fact greatly simplifies the Boussinesq approximation and the ARSM.

Recall that the Boussinesq approximation is given by

$$-\overline{u_i u_j} = \nu_t\left(\frac{\partial U_i}{\partial x_j} + \frac{\partial U_j}{\partial x_i}\right) - \frac{2}{3}k\delta_{ij}. \qquad \text{(D.1)}$$

When i = j, the strain rates found in the Boussinesq approximation are zero. As a result,

$$\overline{u_1^2} = \overline{u_2^2} = \overline{u_3^2} = \frac{2}{3}k. \qquad \text{(D.2)}$$

When $i \neq j$, $\delta_{ij} = 0$, so the Boussinesq approximation predicts the shear stresses to be:

$$-\overline{u_1 u_2} = \nu_t \frac{\partial U_1}{\partial x_2}$$

$$\overline{u_1 u_3} = \overline{u_2 u_3} = 0 \qquad \text{(D.3)}$$

An expression for the turbulence viscosity can be derived using the definition of the rate of turbulence production. Repeating Equation (39) given in Section 5.0:

$$P = -\overline{u_i u_j} \frac{\partial U_i}{\partial U_j} = \nu_t \left(\frac{\partial U_i}{\partial xj} + \frac{\partial U_j}{\partial x_i} \right) \frac{\partial U_i}{\partial x_j}. \qquad \text{(D.4)}$$

For pipe flow, this reduces to

$$P = -\overline{u_1 u_2} \frac{\partial U_1}{\partial x_2} = \nu_t \left(\frac{\partial U_1}{\partial x_2} \right)^2, \qquad \text{(D.5)}$$

so that

$$\nu_t = -\frac{\overline{u_1 u_2}}{\partial U_1 / \partial x_2}. \qquad \text{(D.6)}$$

Similar simplifications can be made in the evaluation of the ARSM. The ARSM equations are:

$$\overline{u_i u_j} = k\left[\frac{2}{3}\delta_{ij} + \frac{(1-\gamma)\left(P_{ij} - \frac{2}{3}P\delta_{ij}\right)}{\varepsilon(C_1 - 1) + P}\right], \tag{D.7}$$

Under the assumptions of fully developed pipe flow, the Reynolds stress production terms, P_{ij}, reduce to:

$$P_{11} = -2\overline{u_1 u_2}\frac{\partial U_1}{\partial x_2}, \tag{D.9}$$

$$P_{12} = -\overline{u_2^2}\frac{\partial U_1}{\partial x_2}, \tag{D.10}$$

$$P_{22} = P_{33} = P_{13} = P_{23} = 0. \tag{D.11}$$

If these expressions are substituted into the ARSM model, the Reynolds stress equations become:

$$\overline{u_1^2} = \frac{2}{3}k - \frac{4}{3}\frac{k(1-\gamma)\overline{u_1 u_2}\frac{\partial U_1}{\partial x_2}}{(C_1 - 1)\varepsilon + P} \tag{D.12}$$

$$\overline{u_2^2} = \frac{2}{3}k + \frac{2}{3}\frac{k(1-\gamma)\overline{u_1 u_2}\frac{\partial U_1}{\partial x_2}}{(C_1 - 1)\varepsilon + P} \tag{D.13}$$

$$\overline{u_3^2} = \frac{2}{3}k + \frac{2}{3}\frac{k(1-\gamma)\overline{u_1 u_2}\frac{\partial U_1}{\partial x_2}}{(C_1 - 1)\varepsilon + P} \tag{D.14}$$

$$\overline{u_1 u_2} = -\frac{k(1-\gamma)\overline{u_2^2}\frac{\partial U_1}{\partial x_2}}{(C_1 - 1)\varepsilon + P} \tag{D.15}$$

$$\overline{u_1 u_3} = 0 \tag{D.16}$$

$$\overline{u_2 u_3} = 0. \tag{D.17}$$

An expression for the rate of turbulence dissipation can be derived using the rate of turbulence production. As discussed in Section 5.0, the dissipation rate can be given as:

$$\varepsilon = \frac{-k(1-\gamma)P_{ij}\frac{\partial U_i}{\partial x_j}}{P(C_1 - 1)} - \frac{P}{C_1 - 1} \tag{D.18}$$

In fully developed pipe flow,

$$P_{ij}\frac{\partial U_i}{\partial x_j} = -\overline{u_2^2}\left(\frac{\partial U_1}{\partial x_2}\right)^2, \tag{D.19}$$

and the turbulence production is given in Equation (D.5). With these simplifications, the expression for the dissipation becomes:

$$\varepsilon = \frac{-k(1-\gamma)\overline{u_2^2}\dfrac{\partial U_1}{\partial x_2}}{\overline{u_1 u_2}(C_1 - 1)} + \frac{\overline{u_1 u_2}\dfrac{\partial U_1}{\partial x_2}}{C_1 - 1}. \qquad \text{(D.20)}$$

In this expression, the Reynolds stresses are ARSM values. This expression can be re-written in the form:

$$\frac{k(1-\gamma)\partial U_1/\partial x_2}{(C_1 - 1)\varepsilon + P} = -\frac{\overline{u_1 u_2}}{\overline{u_2^2}} \qquad \text{(D.21)}$$

The expression on the LHS of Equation (D.21) appears in each of the ARSM stress equations given in Equations (D.12) to (D.15). Substitution then results in:

$$\overline{u_1^2} = \frac{2}{3}k + \frac{4}{3}\frac{\left(\overline{u_1 u_2}\right)^2}{\overline{u_2^2}} \qquad \text{(D.22)}$$

$$\overline{u_2^2} = \frac{2}{3}k - \frac{2}{3}\frac{\left(\overline{u_1 u_2}\right)^2}{\overline{u_2^2}} \qquad \text{(D.23)}$$

$$\overline{u_3^2} = \frac{2}{3}k - \frac{2}{3}\frac{\left(\overline{u_1 u_2}\right)^2}{\overline{u_2^2}} \qquad \text{(D.24)}$$

$$\overline{u_1 u_2} = \overline{u_1 u_2} \qquad \text{(D.25)}$$

The $\overline{u_1 u_2}$ stress component is returned in Equation (D.25) because, under the conditions of fully developed pipe flow, using the turbulence production to derive an equation for turbulence dissipation is equivalent to using the $\overline{u_1 u_2}$ shear stress. No unique expression for this component will therefore exist.

References

1. Moore, J., J.G. Moore, S.P. Heckel, and R. Ballesteros, "Reynolds Stresses and Dissipation Mechanisms in a Turbine Tip Leakage Vortex," ASME Paper No. 94-GT-267, 1994.
2. Kriz, R.A., "Three Visual Methods: Gradients, Function Extraction, and Tensor Glyphs," Class Notes for ESM 5174, Virginia Polytechnic Institute and State University, 1994.
3. Reynolds, O., "On the Dynamical Theory of Incompressible Viscous Fluids and the Determination of the Criterion," Phil. Trans. Roy. Soc., A, Vol. 186, pp. 123-164.
4. Boussinesq, J., "Theorie de l'ecoulement tourbouillant," Memoires presentes par diverse savants a l'academie des sciences de l'institut de France, Vol. 23, 1877.
5. Prandtl, L., "The Mechanics of Viscous Fluids," in W.F. Durand, Aerodynamic Theory, III, 1934.
6. Rodi, W., "Turbulence Models and Their Applications in Hydraulics - A State of the Art Review," International Association for Hydraulic Research, 1980.
7. Launder, B.E., G.J. Reece, and W. Rodi, "Progress in the development of a Reynolds-stress turbulence closure," Journal of Fluid Mechanics, Vol. 48, part 3, 1975, pp. 537-566.

8. Hanjalic, K., and B.E. Launder, "A Reynolds stress model of turbulence and its application to thin shear flows," Journal of Fluid Mechanics, Vol. 52, part 4, 1972, pp. 609-638.

9. Rodi, W., "A New Algebraic Relation for Calculating the Reynolds Stresses," ZAMM 56, 1976, pp. 219-221.

10. Frederick, D., and T.S. Chang, Continuum Mechanics, Scientific Pub. Inc., Boston, 1972, pp. 35-62.

11. Beer, F.P., and E.R. Johnston, Jr., Mechanics of Materials, McGraw-Hill, New York, 1993, p. 23.

12. Hinze, J.O., Turbulence, 2nd ed., McGraw-Hill, New York, 1975, p. 20.

13. Currie, I.G., Fundamental Mechanics of Fluids, 2nd ed., McGraw-Hill, New York, 1993, p. 23.

14. Hill, R., The Mathematical Theory of Plasticity, Oxford University Press, 1950.

15. Press, W.H., S.A. Tuekolsky, W.T. Vetterling, and B.P. Flannery, Numerical Recipes in FORTRAN, 2nd ed., Cambridge Univ. Press.

16 Haber, R.B., "Visualization Techniques For Engineering Mechanics," Computing Systems in Engineering, Vol. 1, No. 1, 1990, pp. 37-50.

17. Laufer, J., "The Structure of Turbulence in Fully Developed Pipe Flow," NACA Report No. 1174, 1954.

18. Hinze, J.O., Turbulence, 2nd ed., McGraw-Hill, New York, 1975, p. 524.

19. Champagne, F.H., V.G. Harris, and S. Corrsin, "Experiments on nearly homogeneous turbulent shear flow," Journal of Fluid Mechanics, Vol. 41, part 1, 1970, pp. 81-139.

20. Moore, J.G., S. Schorn, and J. Moore, "Methods of Classical Mechanisms Applied to Turbulence Stresses in a Tip Leakage Vortex," ASME Paper No. 95-GT-220, 1995.

21. Dishart, P.T. and J. Moore, "Tip Leakage Losses in a Linear Turbine Cascade," Trans. ASME, Journal of Turbomachinery, Vol. 112, No. 4, October 1990, pp. 556-608.

VITA

Scott Schorn was born on August 24, 1970 in Bethesda, Maryland. His family moved to Philadelphia, Pennsylvania in 1977. There, Scott completed his elementary, junior high school, and high school education. He graduated from Downingtown Senior High School in 1988.

In September of 1988, he began his undergraduate studies in Aerospace Engineering at Boston University. In the spring of 1990, Scott tranfered to the Virginia Polytechnic Insititute and State University, and completed his undergraduate education. He graduated with a Bachelor of Science degree in May of 1993.

In August of 1993, Scott began his graduate studies, also at the Virginia Polytechnic Institute and State University. There he investigated the use of tensor visualization techniques in representing the Reynolds stress tensor. This thesis is the culmination of his efforts.